

AD-A265 867



2

ARMY RESEARCH LABORATORY



The Development of a Tungsten Heavy Alloy That Fails by an Adiabatic Shear Mechanism Phase I - SBIR

Sumit Guha, Christos Kyriacou, James C. Withers,
and Raouf O. Loutfy

ARL-CR-56

April 1993

prepared by

Materials and Electrochemical Research (MER) Corporation
7960 S. Kolb Road
Tucson, AZ 85706

under contract

DAAL04-92-C-0009

DTIC
ELECTE
JUN 16 1993
S A D

93-13479



Approved for public release; distribution unlimited.

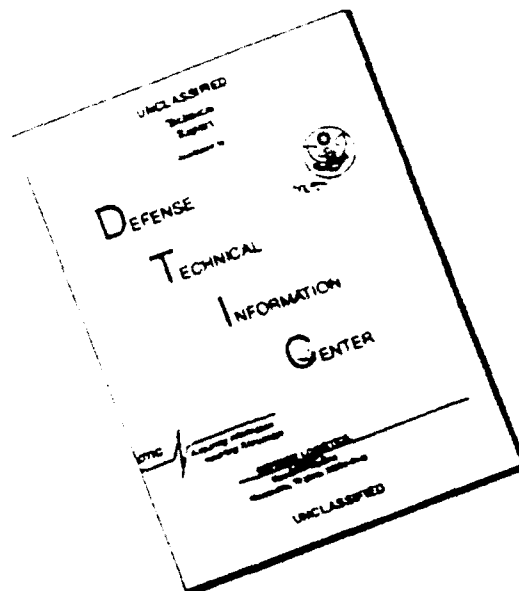
93 6 15 170

The findings in this report are not to be construed as an official Department of the Army position unless so designated by other authorized documents.

Citation of manufacturer's or trade names does not constitute an official endorsement or approval of the use thereof.

Destroy this report when it is no longer needed. Do not return it to the originator.

DISCLAIMER NOTICE



THIS DOCUMENT IS BEST QUALITY AVAILABLE. THE COPY FURNISHED TO DTIC CONTAINED A SIGNIFICANT NUMBER OF PAGES WHICH DO NOT REPRODUCE LEGIBLY.

REPORT DOCUMENTATION PAGE			Form Approved OMB No. 0704-0188	
Public reporting burden for this collection of information is estimated to average 1 hour per response, including the time for reviewing instructions, searching existing data sources, gathering and maintaining the data needed, and completing and reviewing the collection of information. Send comments regarding this burden estimate or any other aspect of this collection of information, including suggestions for reducing this burden, to Washington Headquarters Services, Directorate for Information Operations and Reports, 1215 Jefferson Davis Highway, Suite 1204, Arlington, VA 22202-4302, and to the Office of Management and Budget, Paperwork Reduction Project (0704-0188), Washington, DC 20503.				
1. AGENCY USE ONLY (Leave blank)		2. REPORT DATE April 1993		3. REPORT TYPE AND DATES COVERED Final Report - 1/1/92 - 9/30/92
4. TITLE AND SUBTITLE The Development of a Tungsten Heavy Alloy That Fails by an Adiabatic Shear Mechanism Phase I - SBIR			5. FUNDING NUMBERS Contract No. DAAL04-92-C-0009	
6. AUTHOR(S) Sumit Guha, Christos Kyriacou, James C. Withers, and Raouf O. Loutfy				
7. PERFORMING ORGANIZATION NAME(S) AND ADDRESS(ES) Materials and Electrochemical Research (MER) Corp. 7960 S. Kolb Road Tucson, AZ 85706			8. PERFORMING ORGANIZATION REPORT NUMBER	
9. SPONSORING/MONITORING AGENCY NAME(S) AND ADDRESS(ES) U.S. Army Research Laboratory Watertown, MA 02172-0001 ATTN: AMSRL-OP-PR-WT			10. SPONSORING/MONITORING AGENCY REPORT NUMBER ARL-CR-56	
11. SUPPLEMENTARY NOTES Robert Dowding, COR				
12a. DISTRIBUTION/AVAILABILITY STATEMENT Approved for public release; distribution unlimited.			12b. DISTRIBUTION CODE	
13. ABSTRACT (Maximum 200 words) (See Reverse of SF 298 for Block 13. ABSTRACT.)				
14. SUBJECT TERMS Tungsten alloys, Adiabatic shear, High strain rate, Testing, Processing			15. NUMBER OF PAGES 117	
			16. PRICE CODE	
17. SECURITY CLASSIFICATION OF REPORT Unclassified	18. SECURITY CLASSIFICATION OF THIS PAGE Unclassified	19. SECURITY CLASSIFICATION OF ABSTRACT Unclassified	20. LIMITATION OF ABSTRACT UL	

ABSTRACT

A novel approach to making WHA more susceptible to failure along shear bands would be the use of materials whose ductility decreases with increasing temperature. $L1_2$ -structured intermetallic materials such as B-microalloyed Ni_3Al and two-phase intermetallic, $Ni-12at.\%Al-40at.\%Fe$, with a microstructure consisting of a dispersion of $\approx 10nm$ sized $L1_2$ $(Ni,Fe)_3(Al,Fe)$ within a fcc (Ni,Fe,Al) matrix, exhibit an 'anomalous' material behavior of decreasing ductility with increasing temperature (over the temperature range RT-800°C). $L1_2$ -intermetallic based WHA with various matrix weight fractions (3%, 5%, 7% and 10%) were synthesized by Liquid Phase Sintering. Microstructurally, these WHA were similar to conventional WHA with essentially pure W grains ($\approx 25-30\mu m$ in diameter) in an intermetallic matrix. The quasistatic yield strength of these composites was similar to those measured for conventional WHA although the ductility was considerably reduced; only W+7% Ni-12Al-40Fe exhibited an acceptable combination of strength and ductility ($\approx 4-5\%$ tensile elongation). When tested in compression at very high strain rates ($5000s^{-1}$), these novel WHA exhibited about $\approx 33\%$ increase in peak flow stress compared to conventional WHA. Also, while the heavy alloys based on Ni_3Al matrix exhibited shear localization roughly at 45° to the stress axis, those based on $Ni_{58}Fe_{40}Al_{12}$ matrix failed at $\approx 45^\circ$ to stress axis indicating failure along shear band. Further, while the shear localization initiated at roughly similar strain levels as conventional WHA, failure along shear bands occurred shortly after instability (only after an additional 3-4% strain). The significant improvement in flow stress at high strain rates combined with failure along adiabatic shear bands indicates that the composition W+7%Ni-12Al-40Fe is a possible replacement for DU penetrators. This research, thus, indicates that a WHA design philosophy based on thermally assisted failure along shear bands is a viable approach to designing heavy alloys with self-sharpening behavior.

TABLE OF CONTENTS

I.	ABSTRACT	6
II.	INTRODUCTION	8
	A. General Background	8
	B. Background on WHA and DU Alloys	10
	C. Proposed Concept	16
	D. Proposed Matrix Materials for WHA	20
	E. Alternative Approaches	22
III.	PHASE I RESEARCH OBJECTIVES	24
IV.	EXPERIMENTAL TECHNIQUES	25
V.	PHASE I ACCOMPLISHMENTS	30
	A. Processing	30
	1. Powder Dispersion	30
	B. Powder Processing	42
	1. Mixing	42
	i. Compaction of Powder Mixtures	45
	C. Consolidation	48
	1. Pressureless Sintering	49
	i. Atmosphere	48
	ii. Temperature and Time	50
	2. Hot Pressing	56
	D. Microstructural Analysis	56
	E. Quasi-Static Testing	78
	F. Dynamic Testing	87
	G. Electroless Coating of W powders by Ni	92
	H. Novel Processing Approaches for WHA	97
	I. W-Mn Alloys	102
VI.	DISCUSSION	104

NOT QUANTITATIVELY EVALUATED

Accession For	
NTIS GRA&I	<input checked="" type="checkbox"/>
DTIC TAB	<input type="checkbox"/>
Unannounced	<input type="checkbox"/>
Justification	
By	
Distribution/	
Availability Codes	
Dist	Avail and/or Special
A-1	

LIST OF FIGURES

Figure 1.	Performance gap between DU and WHA penetrators (after [2]). . . .	13
Figure 2.	Variation of (a) ductility and (b) yield strength with temperature for boron-doped Ni_3Al based alloys.	21
Figure 3.	(a) Room Temperature Microstructure and (b) Temperature Dependence of Mechanical properties in L_{12}/fcc intermetallic $\text{Ni-12at.\%Al40 at.\%Fe}$	23
Figure 4.	Process Flow Sheet for Tungsten Heavy Alloy Specimen Fabrication.	27
Figure 5.	Typical Sintering Profile for Tungsten Heavy Alloys.	28
Figure 6.	Tensile Specimen Machining Specifications	31
Figure 7.	SEM micrograph of as-received raw tungsten powders	33
Figure 8a.	Settling behavior of Tungsten powder suspended in different organic solvents.	35
Figure 8b.	Rate of change of sediment height (packing density) for W powders suspended in various organic solvents. Both methanol and isopropanol yield	36
Figure 9a.	Rate of change of 'clear zone' height with settling time for tungsten powders dispersed in toluene with and without dispersants.	37
Figure 9b.	Rate of change of 'sediment' height with settling time for tungsten powders dispersed in toluene with and without dispersants	38
Figure 10.	SEM micrographs of as-received intermetallic powders of (a) $\text{Ni}_3\text{Al-0.02B}$ (b) $\text{Ni-12Al-40Fe(at.\%)}$	41
Figure 11.	Plot of Compaction Pressure vs. Green and Sintered Density of Tungsten Alloys Sintering Conditions	47
Figure 12a-b.	SEM micrograph of WHA specimens sintered at $1500^\circ\text{C}/5\text{mins}$ with 5wt.% intermetallic powder starting with (a) as-received NiFeAl powder (b) ball-milled Ni_3Al powders.	54

Figure 12c-d.	SEM micrograph of WHA specimens sintered at 1600°C/30mins with 5wt.% intermetallic powder starting with (a) as-received NiFeAl powder (b) ball-milled Ni ₃ Al powders.	55
Figure 13.	SEM micrograph for W-5%NiFeAl consolidated by hot-pressing.	57
Figure 14a.	X-ray diffraction pattern of as-received Ni ₃ Al intermetallic powder.	58
Figure 14b.	X-ray diffraction pattern of as-received Ni-12Al-40Fe intermetallic powder.	59
Figure 15.	SEM micrographs of liquid-phase sintered (a) W + 3%Ni ₃ Al & (b) W + 3%NiFeAl.	63
Figure 16a-b.	Low magnification SEM micrographs for liquid-phase sintered (a) W + 5%Ni ₃ Al & (b) W + 5%NiFeAl.	64
Figure 16c-d.	High magnification SEM micrographs for liquid-phase sintered (c) W + 5%Ni ₃ Al & (d) W + 5%NiFeAl.	65
Figure 16e.	X-ray diffraction pattern for sintered heavy alloy W + 5%Ni ₃ Al.	66
Figure 16f.	X-ray diffraction pattern for sintered heavy alloy W + 5%NiFeAl.	67
Figure 17.	High magnification SEM micrographs for liquid-phase sintered (a) W + 7wt.%Ni ₃ Al & (b) W + 7wt.%NiFeAl.	68
Figure 18.	X-ray diffraction pattern for the sintered heavy alloy W + 7%Ni ₃ Al. .	69
Figure 19a-b.	Low magnification SEM micrographs for liquid-phase sintered (15 minutes at 1475 or 1550°C) (a) W + 10%Ni ₃ Al & (b) W + 10%NiFeAl.	72
Figure 19c-d.	High magnification SEM micrographs for liquid-phase sintered (c) W + 10%Ni ₃ Al & (d) W + 10%NiFeAl.	73
Figure 19e-f.	High magnification SEM micrographs for (e) W + 10%Ni ₃ Al and (f) W + 10%NiFeAl sintered at 1475-1575°C/20-30mins.	74
Figure 20.	X-ray diffraction pattern corresponding to specimen in Figure 19f (W + 10%NiFeAl) showing the presence of W, NiFeAl (pattern being similar to Ni ₃ Al) and Ni ₂ W ₄ C phases.	75

Figure 21.	SEM micrographs for conventional WHA (8:2 Ni-Fe ratio) with (a) 7% and (b) 10% matrix.	77
Figure 22.	Fractographs of tensile-tested W+Ni ₃ Al heavy alloys with (a) 5% matrix (b) 7% matrix and (c) 10% matrix.	82
Figure 23.	Fractographs of tensile-tested W+NiFeAl heavy alloys with (a) 5% matrix (b) 7% matrix and (c) 10% matrix.	83
Figure 24.	Fractographs of conventional WHA (W+NiFe) with (a) 7% matrix and (b) 10% matrix.	84
Figure 25.	Polished longitudinal section (near fracture surface) of (a) W+7%Ni ₃ Al, (b) W+7%Ni ₁₂ Al-40Fe & (c) W+7%NiFe	85
Figure 26.	High strain rate (5x10 ³ /sec) stress-strain relationships in intermetallic matrices utilized for WHA.	89
Figure 27.	High strain rate (5x10 ³ /sec) stress-strain relationships in intermetallic-based W heavy alloy composites with 7% and 10% Ni ₃ Al and NiFeAl matrices.	90
Figure 28.	Shear localization in WHA with Ni ₃ Al and NiFeAl matrices.	93
Figure 29.	SEM micrographs of Ni-coated W powders coated by electroless deposition of Ni onto (a) 12μm size (b) 0.5μm size W particles.	96
Figure 30.	SEM micrographs of Ni-Fe coated W powders (≈12μm nominal size) obtained from Ultramet Corp.	100
Figure 31.	SEM micrograph illustrating the minimization of W-W particle contacts by a combination of applied pressure and transient heating (in-situ generation of the intermetallic matrix by a SHS reaction).	101
Figure 32.	SEM micrograph illustrating the refinement of W particle size by induction sintering techniques.	101
Figure 33.	Liquid-phase sintered W+5wt.%Mn alloy showing extensive matrix segregation and porosity.	103

LIST OF TABLES

Table I.	Statistical Experimental Design Applied to Optimize Mixing Process Experimental Approach and Resultant Sintered Densities	43
Table II.	Results of Statistical Analysis of Mixing Process Optimization	45
Table III.	Summary of Results of Effect of Compaction Pressure on Green and Sintered Densities of Tungsten Alloys	46
Table IV.	Cumulative Results of Pressureless Sintering of the Tungsten Heavy Alloys at Three Different Atmospheres	51
Table V.	Results of Densities for Experiments of Sintering Temperatures and Time for the Tungsten Alloy	52,53
Table VI.	Elemental analysis for 95W-5Ni ₃ Al corresponding to Figure 16c.	62
Table VII.	Chemical analysis for 95W-5NiFeAl corresponding to Figure 16d.	62
Table VIII.	Chemical analysis for 95W-10Ni ₃ Al corresponding to Figure 19c.	71
Table IX.	Chemical analysis for 95W-10NiFeAl corresponding to Figure 19d.	71
Table X:	Bend Tensile Results of Pressureless Sintered Tungsten Heavy Alloys	79
Table XI:	Summary of Tensile Test Results of W-Heavy Alloys	79
Table XII:	List of Specimens Shipped to Los Alamos National Labs for Hopkinson Bar Testing	87

I. ABSTRACT

Kinetic Energy penetrators made from Depleted Uranium (DU) alloys have consistently performed better than equi-density and geometrically similar penetrators made from conventional tungsten heavy alloys (WHA) during ballistic penetration tests into semi-infinite Rolled Homogeneous Armor (RHA) steel targets. The superior penetration behavior of DU penetrators is presently attributed to these penetrators maintaining a 'chisel' nose by failure along adiabatic shear bands which is in contrast to the 'mushroom' head observed in WHA penetrators; the 'mushroom' head decreases the energy density at the target thereby leading to reduced penetration. The radiological hazard of DU combined with chemical corrosion during storage provides an impetus to improving the state-of-the-art in WHA with respect to ballistic penetration behavior. Interestingly, WHA penetrators with DU matrix (instead of the conventional Ni-Fe, Ni-Co or Ni-Fe-Co matrices) also fail by adiabatic shear indicating that shear localization is probably influenced greatly by matrix material properties. Hence, an investigation into alternative matrix materials for WHA that will support shear localization is warranted.

Adiabatic shear is an instability between the competing processes of thermal softening and work-hardening. Under high strain rate conditions ($> 10^2 \text{ s}^{-1}$), deformation is often localized into narrow bands termed shear bands. The strain energy in these bands is converted into thermal energy leading to increased temperature along these bands. Evidence of increased temperature is deduced from microstructural transformations, recrystallization or melting observed in these bands in materials subjected to high strain rate tests. The increasing flow stress of the material with increasing deformation (work-hardening) combined with the material softening at high temperatures (the strength and ductility of conventional materials decrease and increase respectively with increasing

temperature) provides the instability condition; failure occurs when the thermal softening processes are dominant and the plastic strain in these bands is sufficient to induce fracture.

One approach to making WHA more susceptible to failure along shear bands would be the use of materials whose ductility decreases with increasing temperature. A class of intermetallic materials namely those with $L1_2$ (ordered fcc) crystal structure exhibit an 'anomalous' material behavior of increasing yield strength and decreasing ductility with increasing temperature (over the temperature range RT-800°C). Ni_3Al is such an intermetallic which has recently been ductilized extensively by microalloying additions of boron. Unfortunately, the work-hardening rate of Ni_3Al is very high. The relationship predicting the critical strain to induce shear instability yields a direct proportionality between the critical strain and the work-hardening rate of the material. Thus, materials with lower work-hardening rates would be conducive to shear localization. A two-phase intermetallic, Ni-12at.%Al-40at.%Fe, with a microstructure consisting of a dispersion of $\approx 10\text{nm}$ sized $L1_2$ $(Ni,Fe)_3(Al,Fe)$ within a fcc (Ni,Fe,Al) matrix, was previously shown by the PI of this program to be extensively ductile at low temperature, yet the work-hardening (albeit at low strain rates) was lower than that for single phase Ni_3Al . Thus, WHA with a matrix that exhibits low work-hardening rate and reduced ductility at elevated temperature should be susceptible to failure along the adiabatic shear bands. In this investigation, it was decided to investigate both Ni_3Al (boron microalloyed) and Ni-12Al-40Fe (at.%) as matrices for WHA.

$L1_2$ -intermetallic based WHA with various matrix weight fractions (3%, 5%, 7% and 10%) were synthesized by Liquid Phase Sintering. Microstructurally, these WHA were similar to conventional WHA with essentially pure W grains ($\approx 25\text{-}30\mu\text{m}$ in diameter) in an intermetallic matrix. The quasistatic yield strength of these composites was similar to those

measured for conventional WHA although the ductility was considerably reduced; only W+7% Ni-12Al-40Fe exhibited an acceptable combination of strength and ductility ($\approx 4\text{-}5\%$ tensile elongation). When tested in compression at very high strain rates (5000s^{-1}), these novel WHA exhibited about $\approx 33\%$ increase in peak flow stress compared to conventional WHA. Also, while the heavy alloys based on Ni_3Al matrix exhibited shear localization roughly at 45° to the stress axis, those based on NiFeAl matrix failed at $\approx 45^\circ$ to stress axis indicating failure along shear band. Further, while the shear localization initiated at roughly similar strain levels as conventional WHA, failure along shear bands occurred shortly after instability (only after an additional 3-4% strain). The significant improvement in flow stress at high strain rates combined with failure along adiabatic shear bands indicates that the composition W+7%Ni-12Al-40Fe is a possible replacement for DU penetrators. This research, thus, indicates that a WHA design philosophy based on thermally assisted failure along shear bands is a viable approach to designing heavy alloys with self-sharpening behavior.

II. INTRODUCTION

A. General Background

In recent years, tungsten heavy alloys (WHA) have found application in many armament systems. Liquid phase sintered W-Ni-Fe or W-Ni-Cu alloys are commonly used as the armor piercing core of medium to large ($> 20\text{mm}$) calibre kinetic energy ammunition [1]. Recently such WHA have also been used in various anti-aircraft and anti-missile warheads. The use of thicker modern armors have prompted the designers of anti-armor ammunition to increase the energy density at the target. The new designs are based on the long-rod principle and are referred to as the Armor Piercing Fin Stabilized Discarding Sabot

type of ammunition. The requirement for a high energy density at the target dictates the use of a high density material. The mechanical property requirements associated with the ballistic performance at the target are unclear, primarily due to the high strain rate and shock loading effects, although there appears to be the need for a balance between strength and ductility. Among materials with densities greater than 15g/cc, only two namely tungsten and uranium are sufficiently cheap and readily available. The uranium (actually depleted uranium, DU) alloys currently in use are U-0.75wt.%Ti while a variety of tungsten based alloys are under consideration. Such heavy tungsten alloys are manufactured by liquid phase sintering a tungsten + Ni-based matrix powder. The tungsten content typically varies between 90-97.5wt.%, the balance being nickel, iron, copper, cobalt, etc. These heavy alloys consist of spherical tungsten particles embedded in a metallic binder and have greater than 99.5% theoretical density. Since the process of sintering may leave behind porosity which may be detrimental to the low strain rate properties of these alloys, elimination of such processing defects are important. Mechanical working, usually swaging, has widely been used as the principal method of hardening these materials. Swaging increases both hardness and strength of the material although at the expense of ductility. Again, a balance between strength and ductility is necessary.

Although both WHA and DU alloys are candidates for such long rod piercing ammunition, in an one-to-one comparison against a spectrum of targets, the DU alloys have consistently demonstrated superior terminal ballistic performance. The superior penetration performance of DU alloys is ascribed to its failure by adiabatic shear mechanisms which allows it to retain a sharp point thereby penetrating further. By contrast, WHA are known to 'mushroom' upon impact thereby decreasing the energy density and hence the effectiveness of such penetrators. The details of failure mechanisms in both systems are

discussed later. In spite of the generally superior performance of DU alloys over WHA, the radiological hazards associated with DU alloys dictate the improvement of performance of WHA penetrators. In the following section, the performance and limitations of existing WHA alloys are discussed and compared with DU alloy penetrators and methods of improving the susceptibility of WHA to adiabatic shear are proposed.

B. Background on WHA and DU Alloys

In this section, we compare the quasi-static and dynamic properties of DU and WHA and their ballistic penetration behavior into RHA steel. Next we discuss the self-sharpening behavior of DU penetrators and why WHA with $L1_2$ intermetallic matrix should perform equally well (if not better). Finally, the selection of specific intermetallics to be investigated is discussed.

Mechanical Properties Of DU And WHA Alloys

Pure uranium is orthorhombic structured (α phase) at room temperature and exhibits two phase transformations before melting at 1132°C. The standard DU alloy for large caliber ammunition is U-0.75wt.%Ti, with the Ti being put into solid solution at high temperature in the b.c.c state (γ phase) followed by rapid quenching. The resulting microstructure is a lenticular martensitic microstructure. An aging treatment which precipitates the intermetallic phase U_2Ti , strengthens the alloy while reducing its ductility. The standard heat treatment for large caliber kinetic energy penetrator (M833 spec.) is 16 hours at 360°C or 4 hours at 385°C [2]. The density of U-0.75Ti is 18.6 g/cc and the 0.2% yield strength, ultimate tensile strength and ductility following the standard heat treatment are, respectively, 850 MPa, 1490 MPa and 24% elongation. Aging to induce precipitation of U_2Ti phase increases the yield strength to 1100 MPa, the UTS to \approx 1600 MPa while the ductility decreases to only 12%. Further aging decreases the ductility further (to 6%)

without significantly affecting the strength properties. Other DU based alloys include those with additions of Hf, Zr, Be or Mo in addition to Ti. Addition of Hf is quite beneficial since the alloy exhibits good strength and ductility (for example, an alloy U-0.9Hf-0.5Ti exhibits 900 MPa yield strength, 1620 MPa UTS and 20% elongation). By contrast, Mo which is an effective strengthener, greatly reduces ductility (again, for example, U-1Mo-0.5Ti exhibits a YS of 1400 MPa, UTS of 1820 MPa but only 6% elongation). Most DU based alloys exhibit high work hardening rates during quasistatic testing.

In contrast to DU alloys, WHA are not homogeneous and cannot be processed simply through casting (as is the case with DU alloys). The b.c.c structured tungsten exhibits no phase transformations between room temperature and its melting point of 3400°C. Unlike DU alloys, the poor ductility and toughness of pure W precludes a direct route to penetrator fabrication; rather, a metal matrix composite consisting of a high volume fraction of tungsten particles embedded in a Ni-Fe (and/or Cu, Co) matrix is preferred. Thus, a porous compact of fine powders of tungsten and matrix elements are placed in the furnace and held at a temperature sufficient for dissolution of tungsten into a liquid matrix. Subsequent precipitation during cooling results in a microstructure consisting of essentially pure W particles, 30-60 μ m in diameter, in a matrix of nickel, iron and dissolved W. Since the use of Ni-Fe based matrix reduces the density of the composite, there exists a minimum limit to the volume fraction of W, usually in excess of 90 wt.%, and frequently up to 97wt.%. For example, a typical WHA would be 93wt.%W-balance Ni-Fe-Co with density of 17.77g/cc. In the unworked condition the mechanical properties are a UTS of 975 MPa and a 33% elongation. In the 20% swaged condition, they exhibit a UTS of 1185 MPa and an elongation of 15% [Teledyne X21C alloy]. While WHA generally lack precipitation hardening mechanisms like DU alloys, strain aging is used to develop various combinations

of strength and ductility. In recent years, several investigators [3-6] have examined the quasistatic and dynamic properties of tungsten alloys in as-sintered and swaged condition. Rabin and German [3] showed that increasing the W content in composites resulted in increased strength but drastically decreased ductility. Bose, Sims and German [4] showed that for the alloy W-7%Ni-3%Fe, the strain rate sensitivity decreases with increasing temperature. Meyer and coworkers [5] evaluated the dynamic (strain rates up to $5 \times 10^3 \text{ sec}^{-1}$) strength and ductility of WHA composites in as-sintered and swaged conditions and showed that for each alloy a characteristic increase in strength (sometimes twice the quasistatic value) and decrease in ductility with increasing strain rates was observed. Lankford et al.[6] proposed a relationship between strength and fracture mode of explosively fractured WHA which indicated a change from cleavage fracture in W particles for low strength WHA to interfacial W-W and W-matrix fracture for high strength WHA. The quasistatic strength and ductility are generally inferior to the DU alloys. While the elastic moduli of WHA are higher than DU alloys, their (quasistatic) work-hardening rates are lower. Higher volume fractions of W generally result in degraded ductility primarily due to the increased frequency of W-W contiguity.

Penetration Performance of DU And WHA

The process of penetration of a target by a projectile at typical ordinance velocities is not well understood. While it is clear that the inertial forces generated by acceleration and displacement of target material and the deceleration and erosion of target material greatly exceed the strength of both projectile and armor materials, many aspects of the physical and materials processes under the conditions of high hydrostatic pressures (5-50GPa) and high deformation rates ($10^4 - 10^6 \text{ sec}^{-1}$) are not well understood, hence, the penetration process is difficult to model. Qualitatively, the process of penetration consists

of the penetrator being consumed as it burrows into the armor, 'back-extruding' from the penetrator- target interface while the interface moves forward into the target.

The influence of materials parameters on ballistic performance has been studied experimentally at the Army Ballistic Research Laboratory (presently known as the Weapons Technology Directorate of the U.S. Army Research Laboratory); trends observed in the model-scale tests have also been observed in the full scale tests [6-9]. In one such study examining the penetration depths into a rolled homogeneous armor (RHA) steel of equivalent geometry (rod of length-to-diameter of 20) and equal mass (65 gms) M833 specification DU (density 18.6 g/cc) and WHA (93wt.% W, density of 17.6g/cc) penetrators, DU penetrators were observed to perform consistently better over the range of impact velocities (800-2000m/sec), see Figure 1. Use of higher density (97 wt.% W) WHA penetrators result in slightly reduced difference in their penetration capabilities.

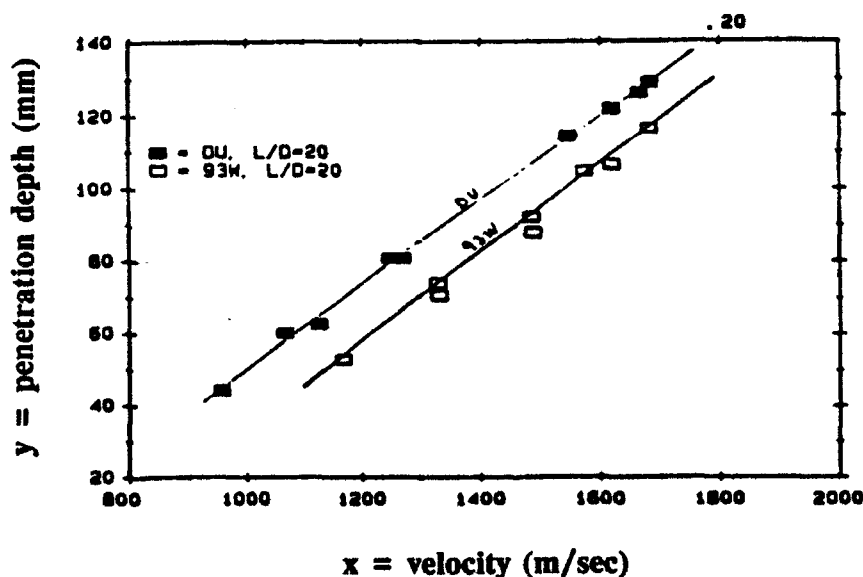


Figure 1. Performance gap between DU and WHA penetrators (after [2]).

An alternate method of judging the penetration capabilities is the determination of limit velocities. The velocity at which a 65 gms projectile of DU and WHA (long rod geometry, $L/D = 15$) just perforates a 3" RHA thick plate was observed to be lower by ≈ 100 m/sec for DU alloys than WHA penetrators. While increasing strength and hardness of DU alloys significantly increased its penetration capabilities, similar changes in mechanical properties of WHA appear to exert no influence on penetration performance. Only an increased density was observed to be beneficial to improved penetration capabilities.

While the poorer penetration performance of WHA (despite almost similar densities to DU alloys) have been attributed to the generally poorer mechanical properties of WHA (than DU alloys), x-ray radiographic images of the target-penetrator interface taken during the penetration process shows less flare for DU projectiles [10]. It was suggested that neither density nor mechanical properties are the root cause, rather, the low work-hardening rates of DU alloys (during dynamic loading) were principally responsible for the improved performance. Interestingly, the low work-hardening rates of DU alloys during dynamic loading are in contrast to the high work-hardening rates observed during quasistatic loading of the same [11]. This indicates the difficulty in predicting projectile performance behavior based on quasistatic mechanical properties. Alternate suggestions to the improved performance of DU penetrators include the formation of low melting point U-Fe intermetallics which, acting as a lubricant at the penetrator-target interface, allows the projectile to defeat the target more easily [12].

While the performance gap between DU and WHA penetrators cannot be satisfactorily explained by changes in mechanical properties, they do exhibit differences in their penetration behavior. For example, while the U-0.75wt.%Ti alloys retain a chiseled-

nose after penetration, the WHA usually retain a mushroomed head on the back side of the armor. The chiseled nose appearance in the former is related to the deformation being localized in adiabatic shear bands between the chips while the large mushroom head which develops during erosion and back extrusion of the penetrator rod is related to the great deal of plastic deformation in the WHA before localization of deformation and discarding of the back extruded material. Interestingly, the observed shear localization behavior in WHA is intermediate between those of refractory metals with low thermal-softening characteristics (e.g. W, Ta) where no shear localization is observed and α -U which deforms predominantly by adiabatic shear. While ballistic performance of WHA improves with increasing density, for equidensity WHA (97%W in Ni-Fe matrix) and U-0.75Ti penetrators, a performance gap of 100m/sec was observed in the limiting velocity. Again, the strength of WHA appears to exert almost no influence on the penetration performance. The penetration tunnels were roughened due to irregular discard of the eroded material. Interestingly, replacing the Ni-Fe matrix with Ta resulted in degraded performance (25 to 30m/sec higher limit velocity) and no localization of plastic flow was observed [13]. Further, such ductile flow has also been reported for pure tungsten penetrators [14]. Similarly, a U-6%Nb penetrator which exhibited bulk plastic deformation but no localized deformation (no adiabatic shear bands) was observed to perform poorly compared to the standard U-0.75Ti alloys. The limit velocity of the U-6%Nb penetrators was similar to those of equidensity WHA. These results are strongly indicative of the superior ballistic performance of DU penetrators being related to their failure by localized deformation (adiabatic shear bands) [2].

Interestingly, WHA composites synthesized using a DU alloy as a matrix perform very well as a penetrator which is strongly indicative of the role of the matrix (rather than

the W particles themselves) being the key to improved penetration performance. Clearly, WHA composites based on matrices prone to adiabatic shearing need to be emphasized.

C. Proposed Concept

Adiabatic shear bands have been known to occur in materials due to instabilities in plastic deformation resulting from the opposing effects of work-hardening and thermal softening behavior of materials. Since a large fraction of the energy of deformation is converted into heat, the temperature within a narrow deformation zone (shear band) is increased with increasing deformation. Under the action of high strain rates (typical of ballistic impact), there is little time for diffusion of the heat into the surrounding material, hence the temperature within the deformation zone increases rapidly and may approach the melting point of the material. Further, increased deformation also results in increased flow stress within the shear band. However, for materials whose increase in flow stress due to strain hardening or strain rate hardening is weaker than the load bearing capacity due to thermal softening, an instability develops and deformation is further concentrated within the shear band. Materials commonly known to be susceptible to adiabatic shear band failure are titanium based alloys (e.g. solution treated and aged Ti-6Al-4V), AISI 4340 and some other grades of steels, 2014 T6 aluminum alloys, etc. Interestingly, Shockey et al. [15] has demonstrated that microstructural features like defects and heterogeneities are not important to shear bands, rather, the propensity of shear band formation is proportional to the material properties like the hardness (i.e. higher the hardness, the higher the tendency for shear band formation). Furthermore, a strong effect of texture on shear band failure was observed, with the failure occurring preferentially along the weakest planes.

The flow stress of a material is a function of temperature, strain, and strain rate. Mathematically,

$$\tau = f (T, \gamma, \gamma').$$

The criteria for development of shear instability is given by:

$$0 = d\tau/d\gamma = \delta\tau/\delta\gamma|_{\gamma,T} + \delta\tau/\delta\gamma'|_{\gamma,T} d\gamma'/d\gamma + \delta\tau/\delta T|_{\gamma,\gamma'} dT/d\gamma \quad (1)$$

where τ is the shear strength, γ is the plastic shear strain and γ' the shear strain rate. The first (total differential) term represents the change in shear strength of material with strain while the three partial differentials represent, respectively, the work hardening, the strain-rate hardening and the thermal softening. For catastrophic shear, $d\tau/d\gamma = 0$. Due to the high strain rate, all the energy of deformation can be assumed to contribute to heating, thus,

$$dT/d\gamma = \tau/C \quad (2)$$

where C is the volume specific heat of the material [16]. For parabolic strain hardening behavior, the critical shear strain at instability is given by

$$\gamma_c = n / (-1/C \delta\tau/\delta T|_{\gamma,\gamma'} - m/\gamma' d\gamma'/d\gamma) \quad (3)$$

where n and m are, respectively, the strain hardening and strain rate hardening exponents. Since $0 \leq m \leq 1$ and as long as the strain rate is at least 10^2sec^{-1} , the second term in the denominator is negligibly small. Thus, the simplified expression for critical strain to adiabatic shear (under ballistic impact) is given by:

$$\gamma_c = -Cn / (\delta\tau/\delta T|_{\gamma,\gamma'}) \quad (4)$$

For explosively loaded AISI 4340 steel cylinders, Staker [16] has demonstrated good correlation between the observed and predicted critical shear strain values. Since steel exhibits decreased strength and increased ductility with increasing temperatures, thus, $\delta\tau/\delta T < 0$, hence γ_c is a positive number. The equation predicts that a weak work-hardening rate and strong (negative) temperature dependence of shear stress will favor adiabatic shear.

Equation (2) deserves a closer look. Assuming that $\tau = k\gamma^n$ and integrating the equation with respect to γ we get:

$$T = k \gamma^{n+1} / (C (n+1)) + K1 \quad (5)$$

where K1 is an integration constant and the remaining symbols have their usual meaning (defined earlier). Substituting $k/(n+1)$ as K2, and rearranging terms we get:

$$\gamma = C/K2 (T - K1)^{1/(n+1)} \quad (6)$$

From equation (6), for $T > K1$, a positive dependence of γ on T is clear, that is, the ductility increases with increasing temperature. While this is the usual behavior exhibited by most materials, it would be interesting to examine the effects on shear instability if one were to use a material that exhibited decreasing ductility with increasing temperatures. Certain intermetallic compounds (referred to as $L1_2$ structured alloys) do exhibit such a phenomenon and are discussed in more detail later.

Referring back to equation (1) and retaining the term $dT/d\gamma$ (i.e. not using the substitution in equation (2)), the form of equation at instability ($d\tau/d\gamma = 0$) for a material strained at high strain rates will be:

$$-\delta\tau/\delta\gamma|_{\gamma,T} = \delta\tau/\delta T|_{\gamma,\dot{\gamma}} dT/d\gamma \quad (7)$$

For parabolic strain hardening, the equation (7) becomes:

$$-k n \gamma^{n-1} = \delta\tau/\delta T|_{\gamma,\dot{\gamma}} dT/d\gamma \quad (8)$$

Rearranging, we get:

$$-n d\gamma/dT / (\delta\tau/\delta T|_{\gamma,\dot{\gamma}}) = \gamma/\tau \quad (9)$$

$$\text{Or } \gamma_c = \{-k n d\gamma/dT / (\delta\tau/\delta T|_{\gamma,\dot{\gamma}})\}^{1/(1-n)} \quad (10)$$

Equation (10) predicts that a weak work-hardening rate, strong temperature dependence of strength and weak temperature dependence of ductility will favor adiabatic shear. For conventional materials, since both yield and tensile strength decreases while ductility increases with increasing temperature, $\delta\tau/\delta T < 0$ and $d\gamma/dT > 0$, hence γ_c is a positive number, similar to the condition derived from equation (4). $L1_2$ structured alloys generally

exhibit decreased ductility with increasing temperatures; some $L1_2$ alloys exhibit increased yield strength with increasing temperatures (referred to as 'anomalous strengthening') while others exhibit a gradual thermal softening behavior. Almost all $L1_2$ alloys, however, exhibit decreasing ultimate tensile strength with decreasing temperatures. For alloys which exhibit anomalous strengthening, $\delta\tau/\delta T > 0$, $d\gamma/dT < 0$ and $n < 1$, γ_c is a positive number similar to that derived earlier for conventional materials. For alloys which exhibit both thermal softening and temperature assisted embrittlement, γ_c is a finite negative value which may be interpreted as a smaller value of γ_c necessary (than that predicted by equation 4) for adiabatic shear. In the absence of numerical values, it is not clear which set of criteria would be more amenable to adiabatic shear. A qualitative explanation of the possible failure mode for heavy tungsten alloys with $L1_2$ matrix would be as follows: as the localized deformation is initiated within a shear band, the energy of deformation would be converted into heat which would raise the temperature of the material within the shear band. Since $L1_2$ structured alloys become increasingly brittle with increasing temperature up to a temperature of 700°C, the shear band should become increasingly susceptible to cracking [17]. Further, many $L1_2$ alloys exhibit lower melting temperatures than the conventionally used Ni-Fe matrix. Hence the desired effect of self-sharpening penetrator may be possible. Since the exact deformation characteristics are not clear (whether $\delta\tau/\delta T$ greater than or less than zero is more desirable), it is proposed to examine two different matrix materials representing either characteristics. The problem, thus, is to find materials that would exhibit either a positive or negative dependence of strength on temperature and negative dependence of ductility with temperature (besides a low work-hardening rate).

D. Proposed Matrix Materials for WHA

The last decade has seen an extended interest in a novel class of materials called intermetallics which possesses mechanical properties intermediate between those of ceramics and metals. For example, while intermetallics exhibit good resistance to environmental degradation, low volume diffusion and relatively better strength at high temperatures, they also exhibit better toughness than most ceramics and, in some cases, are actually very ductile. Among these intermetallics, $L1_2$ (ordered f.c.c) structured alloys have attracted special attention due to their unusual property of increasing strength with increasing temperatures. Examples of $L1_2$ intermetallics abound in literature, a few well known ones being Ni_3Al , Ni_3Si , Co_3Ti , Cu_3Au etc. Among these, we proposed to concentrate on $L1_2$ intermetallics such as Ni_3Al .

The $L1_2$ -structured intermetallic Ni_3Al exhibits tensile ductility in single crystal form. Polycrystals of stoichiometric (25at.%Al), Ni-rich and Al-rich Ni_3Al are, however, brittle and fail by intergranular fracture [18]. The slip systems of Ni_3Al under quasistatic loading have been determined to be $\{111\} \langle 110 \rangle$, which provides five independent deformation modes. Thus, the brittleness of Ni_3Al is unrelated to the lack of any sufficient number of slip systems. Rather, Ni_3Al suffers from an intrinsic grain boundary weakness. The beneficial effect of boron addition on the mechanical behavior of Ni_3Al was first reported by Aoki and Izumi [19]. The tensile ductility of the stoichiometric alloy was improved from zero to $\approx 35\%$ by the addition of a few hundred ppm of boron. Thus, while intermetallics normally exhibit limited room temperature ductility, boron-doped Ni_3Al exhibits extensive ductility.

While dramatic improvement in ductility resulted from microalloying with boron, the ductility is sensitive to test temperature and atmosphere. Figure 2 shows the variation of yield strength and ductility of boron-doped Ni_3Al with temperature. It is clear that there

exists a minimum in ductility around the temperature range 700-800°C. Fracture behavior changed from dimple type at room temperature to increasingly intergranular fracture at higher temperatures [18]. Ductility minimum is reduced in severity when tests are carried out in vacuum. For example, for an alloy containing 0.5%Hf and 0.07%B, the ductility at 760°C increased steadily as the air pressure was decreased from 1 to 10^{-8} torr [18]. The embrittlement in oxygen bearing atmospheres at elevated temperatures appears due to adsorption of oxygen at grain boundaries, thereby lowering cohesion. However, even cube oriented single crystals of $\text{Ni}_3(\text{Al,Ti})$ when tested over a range of temperatures, exhibited sharply decreased ductility from about 15% at room temperature to $\approx 1\%$ at 827°C [18] (the peak flow stress temperature, see below), indicating that the high temperature embrittlement may be an intrinsic behavior of Ni_3Al and unrelated to grain boundary embrittlement.

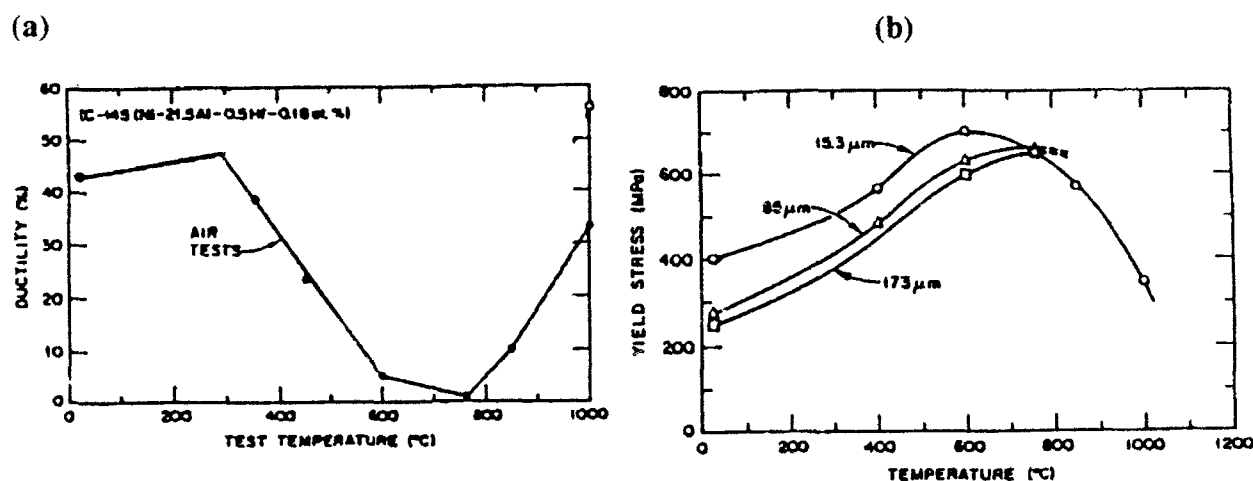


Figure 2. Variation of (a) ductility and (b) yield strength with temperature for boron-doped Ni_3Al based alloys.

Ni_3Al also exhibits an anomalous yield strength behavior (Figure 2b) where the yield strength increases with increasing temperatures up to 700°C, a behavior which has been the

primary source of such extended interest in Ni_3Al . The anomalous yield strength behavior is postulated to arise from the immobilization of the dislocation pair arising from the cross-slip of the leading super-partial on to the $\{100\}$ plane driven by the reduction of APB energy. The mechanism was originally proposed by Kear and Wilsdorf [18]. For the stoichiometric and Ni-rich composition, the peak flow stress has been reported to be influenced by the grain size. Interestingly, for similar grain sizes, boron doping resulted in increased flow stresses over the undoped alloy.

Ductility improvements have also been reported in Ni_3Al with macroalloying additions of Fe [17]. One such alloy is Ni-12at.%Al-40at.%Fe which exhibits an order-disorder type of microstructure, that is, L_{12} precipitates in a disordered fcc matrix. The alloy exhibits a room temperature yield strength of 500 MPa, a tensile strength of 800 MPa and about 27% elongation. Unlike boron-doped Ni_3Al , this alloy exhibits a lower work hardening rate. When tested in tension at high temperatures, the yield strength decreased gradually with increasing temperatures while the ductility decreased sharply, see Figure 3. The liquidus temperature of this alloy is about 1350°C (similar to DU alloys) [20].

Thus, it is clear that using boron-doped Ni_3Al (or even Ni-12at.%Al-40at.%Fe alloys) as a matrix for W particles, the WHA composite will be capable of significant (quasi-static) ductility so as to undergo the mechanical cold working processes such as swaging etc. Thus, a cold worked L_{12} -based matrix, by virtue of its low work hardening rate and increasing embrittlement with increasing temperatures, may be more susceptible to adiabatic shear.

E. Alternative Approach

Recent attempts to substitute the Ni-Fe matrix in WHA with non-conventional materials such as Hf (known to be susceptible to adiabatic shear) have not yielded the

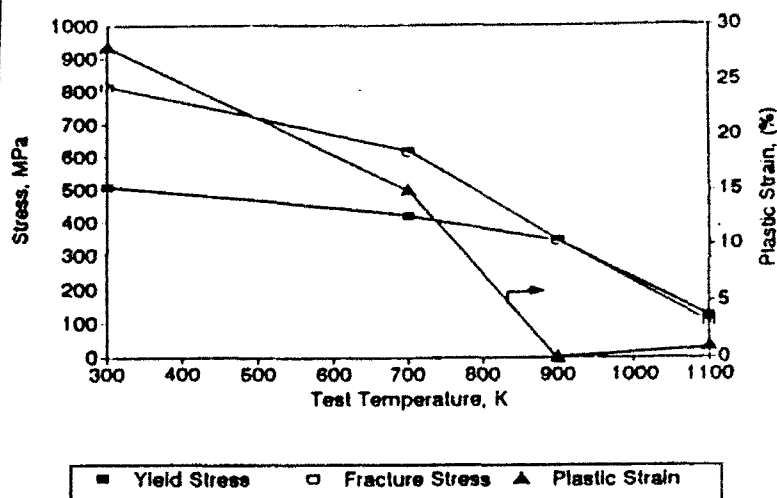
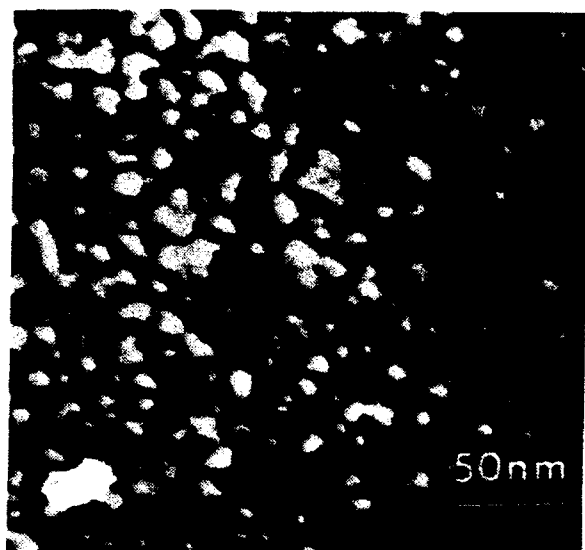


Figure 3. (a) Room Temperature Microstructure and (b) Temperature Dependence of Mechanical properties in L1₂/fcc intermetallic Ni-12at.%Al-40at.%Fe.

expected results. A radically different yet promising approach would be the use of single crystals of tungsten. Bruchey et al.[22] have examined the ballistic characteristics of [100], [110] and [111] single crystals of tungsten and reported promising results for [100] oriented crystals; such [100] crystals exhibited similar performance to the geometrically similar U-0.75Ti alloys which was attributed to the favorable slip/cleavage during compressive loading without large scale plastic deformation and the occurrence of shear localization at a favorable angle for easy material flow away from the penetrator interface. Synthesis of composites containing [100]-oriented whiskers of tungsten in a ductile matrix, while a technically feasible approach, would not be economically feasible without developing a low cost technology for growing [100] W whiskers. One possible approach, however, is imparting a suitable texture to the matrix for a b.c.c matrix-based WHA, for example, W-Mn composites (Mn being more preferable due to its lower melting point of 1260°C). Use of a b.c.c matrix may also limit the coarsening of W particles by limiting transport of b.c.c W

through b.c.c Mn. Such a concept was recently demonstrated by Kipphut et al.[23] where use of b.c.c Mo in Ni-Fe matrix limited the growth of W particles. Since the matrix rather than the tungsten particles themselves will govern the propensity to adiabatic shearing, orienting the b.c.c Mn matrix for favorable slip/cleavage along its weakest plane during impact, that is, imparting a [100] texture to the matrix (just like W single crystals), may be a viable alternative. Since b.c.c structured materials are known to generate a $\langle 110 \rangle$ wire texture during extrusion [24], 45° sections to the extrusions are likely to exhibit a $\langle 100 \rangle$ texture. (It remains to be demonstrated, however, that extruded W-Mn WHA will indeed exhibit a $\langle 110 \rangle$ texture). Alternate processing schemes include rolling which is known to generally impart a $\{100\} \langle 110 \rangle$ rolling texture to b.c.c metals. The possibility of using Mn as an alternate matrix was considered worth exploring as a secondary approach (intermetallic-based WHA being the primary emphasis of this investigation).

III. PHASE I RESEARCH OBJECTIVES

The overall technical objective was to develop tungsten-based penetrators that perform at least as well as the existing DU penetrators. The Phase I technical objective was to identify alloy systems that are compatible with the tungsten heavy alloy concept and, when used as a matrix, either exhibit shear localization or fail by adiabatic shear mechanisms. The specific objective of this program was to investigate whether self-sharpening mechanisms of failure along shear bands during high strain rate impact are achievable using matrices based on L1₂ alloys (Ni₃Al, Ni-12at.%Al-40at.%Fe). To establish these technical objectives, the Phase I program pursued the following questions:

1. Will tungsten heavy alloys based on Ni_3Al or $\text{Ni-12at.\%Al-40at.\%Fe}$ matrices exhibit adiabatic shear failure when subjected to high strain rates of deformation?
2. Which of the following is a better route for synthesis of these composites: liquid phase sintering or hot pressing?
3. Can the coarsening of W particles be prevented using such matrices?
4. Will $\text{W-Ni}_3\text{Al}$ or $\text{W-(Ni-12at.\%Al-40at.\%Fe)}$ systems exhibit the formation of intermetallics during their synthesis?
5. How will the room temperature quasistatic properties of W-based heavy alloys with Ni_3Al , $\text{Ni-12at.\%Al-40at.\%Fe}$ or Mn matrices compare against conventional WHA?
6. What would be the resulting texture from extrusion or rolling of W-Mn alloys and will they exhibit adiabatic shear when subjected to high strain rates?

At the end of the Phase I investigation, judging by the results from quasistatic and dynamic testing, a more detailed optimization of matrix compositions and novel processing approaches to minimize W-W contiguity was to be carried out in a Phase II follow-up investigation.

IV. EXPERIMENTAL TECHNIQUES

The preliminary results of experiments performed for the development of a process to consolidate the W-intermetallic heavy alloys provided the fundamental processing parameters for the preparation of specimens for tensile, bend and Hopkinson Bar testing; details pertaining to the selection of these processing parameters is described in Section V.A. Some variations in the final sintering temperature and time were made to adjust for variation in the amount of liquid phase present. A process flow sheet for the preparation

of specimens is shown in Figure 4. A plot showing the typical sintering profile followed for each composition of the intermetallic and conventional alloys is shown in Figure 5.

The as-received intermetallic powders were ground in a steel ball mill using stainless steel and tungsten carbide grinding media for a period of 24 hours to reduce the particle size to $<5\mu\text{m}$. The powders were ground in a solvent - Isopropanol. The ground powder was diluted and dispersed in isopropanol and the finer fractions were separated by sedimentation in 2 foot tall (3 inch diameter) columns. Powder retained in suspension after 30 minutes was collected and separated from the liquid using a centrifuge. The powder was rinsed with fresh alcohol 3 times to remove the dispersant added during ball milling and sedimentation. The fine powder was then dried and characterized using SEM.

The tungsten powder was used in the as-received condition and was mixed with the intermetallic powder in isopropanol. Mixing was done in plastic containers using stainless steel and tungsten carbide media and SOLSPERSE 20000 was added to aid dispersion and maintain a stable mixture. Mixing was done for two hours, after which the mixture was dried in a vacuum oven at 50°C . The powder mixture was then dry pressed in stainless steel dies at a pressure of 30ksi. For general microstructural analysis and process development, specimens of $\frac{1}{2}$ " diameter were used. For mechanical testing (4-pt bend and tensile) specimens, a die cavity of 2" X 1" was used, and for Hopkinson Bar specimens a die cavity of $\frac{1}{4}$ " diameter was used. The specimens were then labeled and prepared for pressureless sintering. The specimens were loaded inside an aluminum oxide crucible and surrounded by tabular aluminum oxide (+20 mesh). A total of 5-7 samples were loaded inside a crucible per sintering run. For the case of the 2" X 1" specimens, plates of aluminum oxide were used to support them for the purpose of avoiding warpage. The

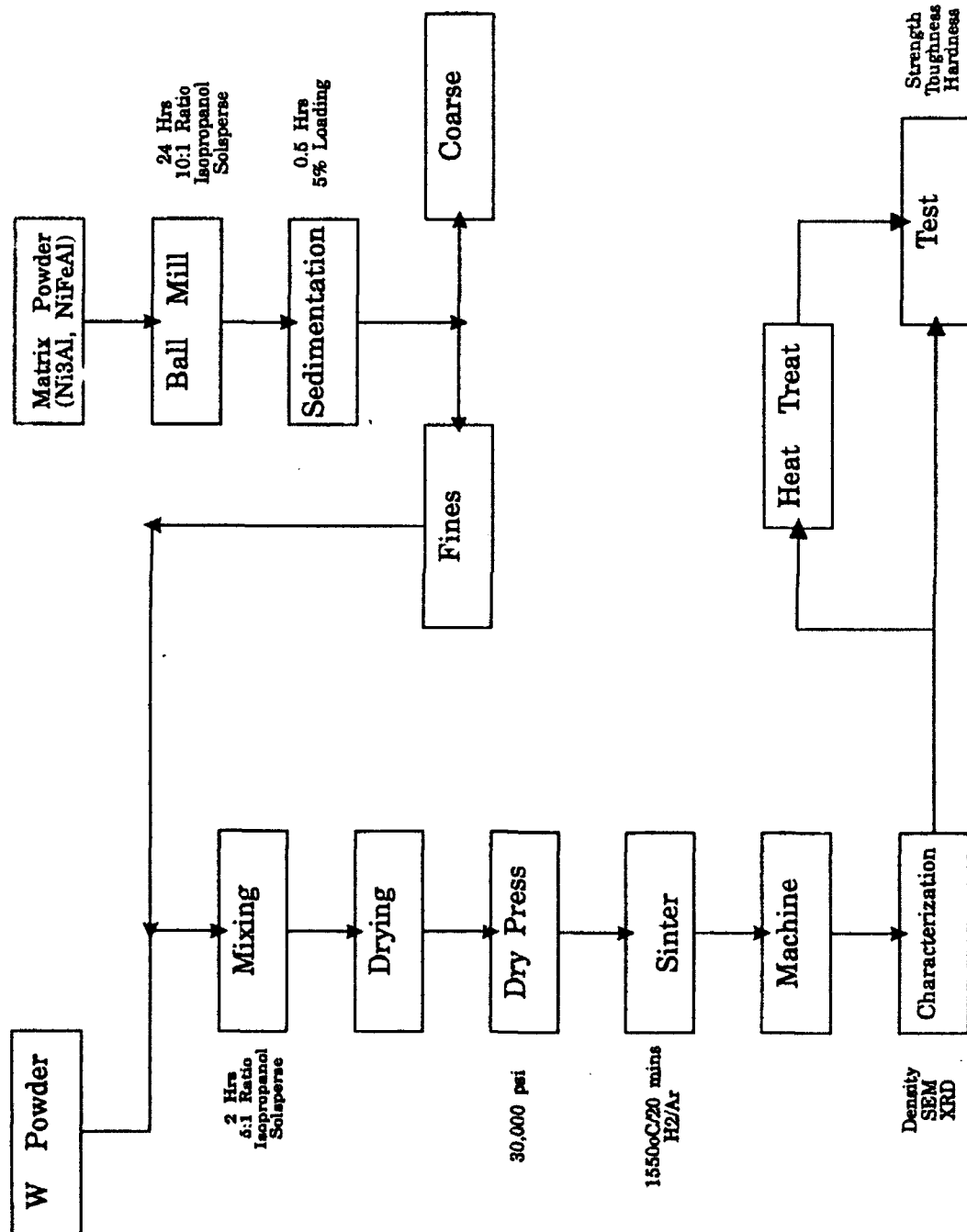


Figure 4. Process Flow Sheet for Tungsten Heavy Alloy Specimen Fabrication

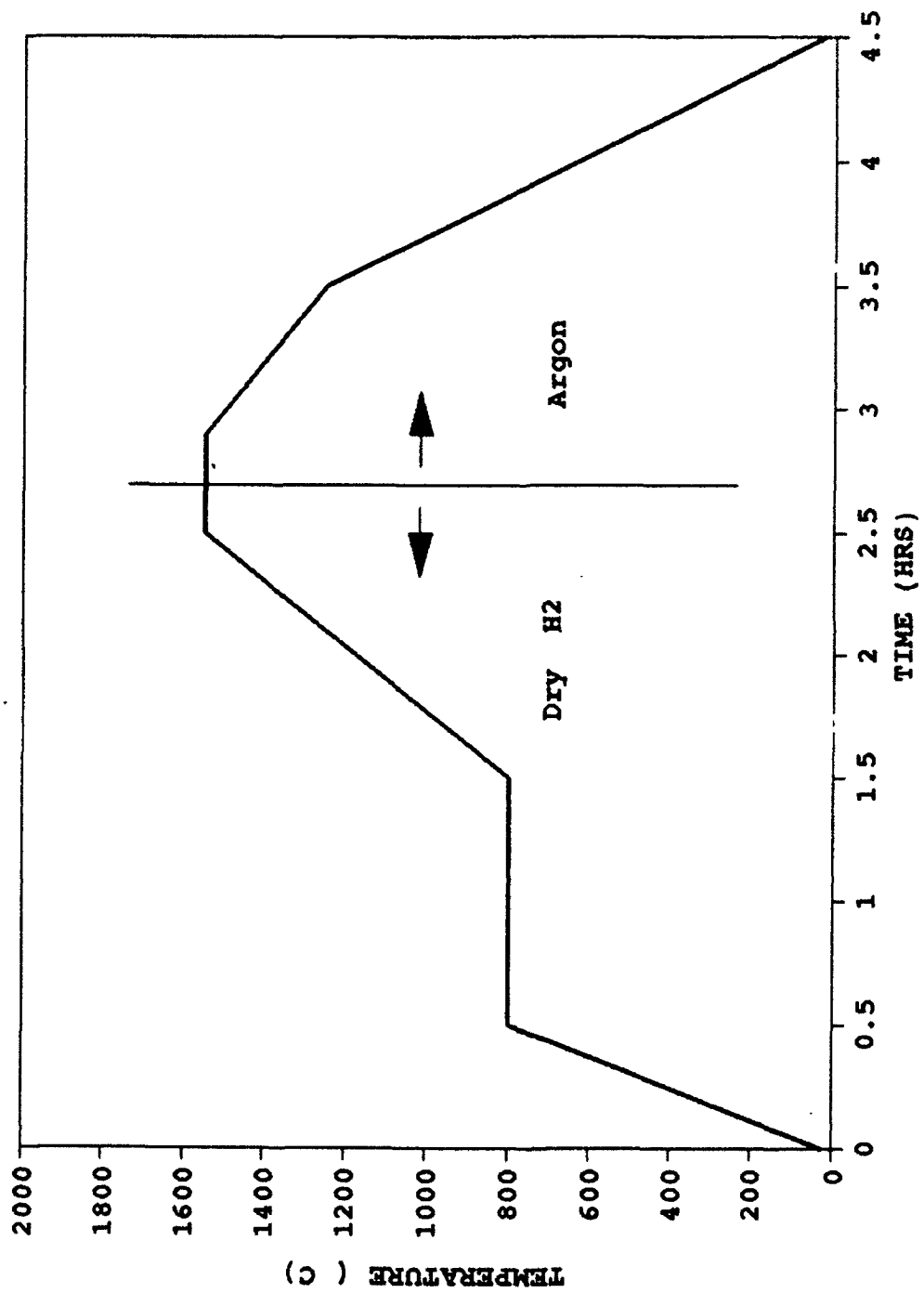


Figure 5. Typical Sintering Profile for Tungsten Heavy Alloys

specimens were sintered inside a 6" diameter furnace heated with graphite heating elements. The hydrogen/argon gas was delivered to the samples using an aluminum oxide tube which was reaching directly into the crucible. The furnace was evacuated and backfilled with hydrogen twice before heating had commenced. The samples were heated at 25°C/min to 800°C and held for 1 hour, re-heated at a new rate of 12.5°C/min to the desired sintering temperature (1475°C or 1550°C) and maintained there for a period of 15-30 minutes (the sintering temperature and time varied depending on alloy type and composition; exact conditions can be found in a later section on processing). At the middle of the sintering soak, the gas was switched to argon for the rest of the sintering cycle. The samples were cooled from the high temperature to 1250°C at a rate of 10°C/min. After that, the furnace power was shut-off and the furnace left to self-cool down to room temperature.

The samples were removed from the aluminum oxide bed and weighed. The densities were measured using the water displacement method. Microstructural analysis was performed by mounting samples in epoxy and polishing them down to 0.5 μ m finish. Polishing of the samples involved a total of 5-6 polishing steps before clear separation of the tungsten grains from the matrix was possible. The samples were then mounted on SEM specimen mounts and coated with a thin coating of Au-Pd. The general sample microstructure was examined and recorded with micrographs. The general and local sample chemistry was analyzed using x-ray analysis (EDAX) for elements with atomic number 11 or higher. The relative amount of the elements present in the tungsten grains and the matrix were estimated using standardless techniques.

Bend and tensile specimens were prepared from dry pressed flat specimens with green dimensions of 2" x 1.1"; after sintering, the samples had dimensions of ~ 1.5" x 0.95" x 0.10" thickness. The specimens were machined on a surface grinder to remove the surface

skin and produce flat and parallel surfaces. The surface was finished with a 320 mesh diamond dressed wheel. Bending specimens 0.16" wide were cut using diamond blades. The specimens were further polished using abrasive diamond paste to a finish of 1 micron. Four point bend tests were performed in-house using a 1000 lb_f load cell. A testing fixture with an inner span of 9mm and an outer span of 18mm was utilized.

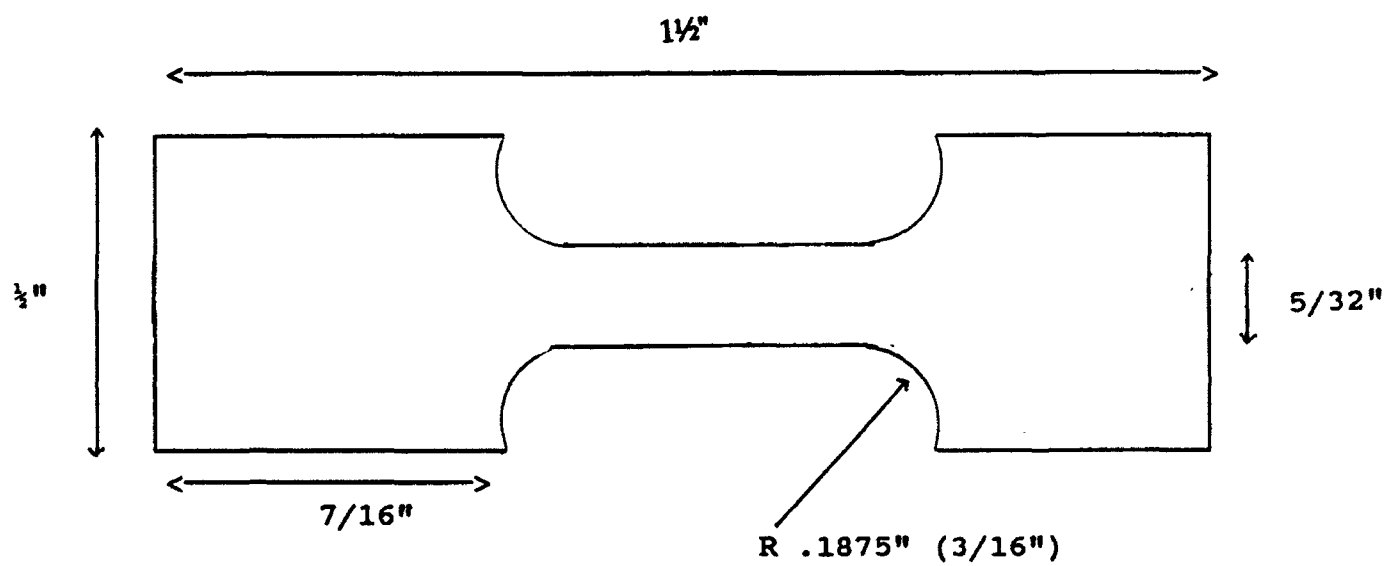
Size and shape specifications of tensile specimens cut to dogbone shape by electrodischarge machining (EDM) are shown in Figure 6. After machining, the specimens were stress-relief annealed at 750°C for 2 hours in vacuum. The samples show no apparent shape change or discoloration during heat treatment. Tensile testing was done at the University of Arizona, Materials Science Department, using an Instron tester (10,000 lb_f). A crosshead speed of 0.002 in/min was used which corresponds to an initial strain rate of 1×10^{-4} /sec. Samples were held using 500 lb jaws.

V. PHASE I ACCOMPLISHMENTS

A. Processing

1. Powder Dispersion

The dispersion of micron sized particles of different types of metals is of extreme importance in the synthesis of heavy alloys with uniform composition. The attractive forces between small particles strongly affect the mixing and settling behavior of powders suspended in an organic liquid. The high specific gravity of the powders and the differences in specific gravity make their suspension in the liquid very difficult. The dispersion of the tungsten powder was investigated in liquid organic solvents for the purpose of optimum mixing. The goal was to identify a suitable solvent and a dispersant for the tungsten and intermetallic powders.



Material: Tungsten
Tolerances: $\pm 0.010"$

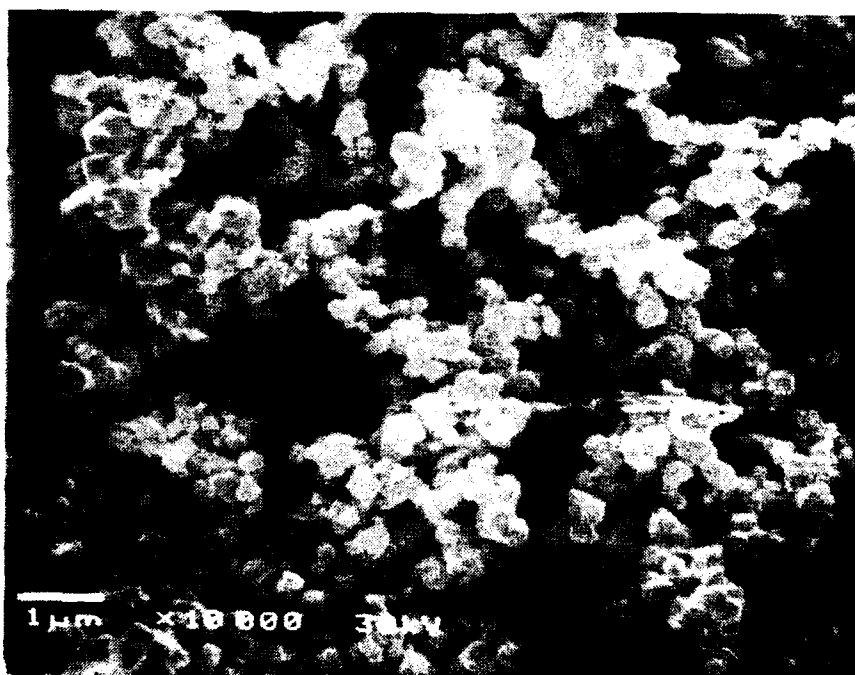
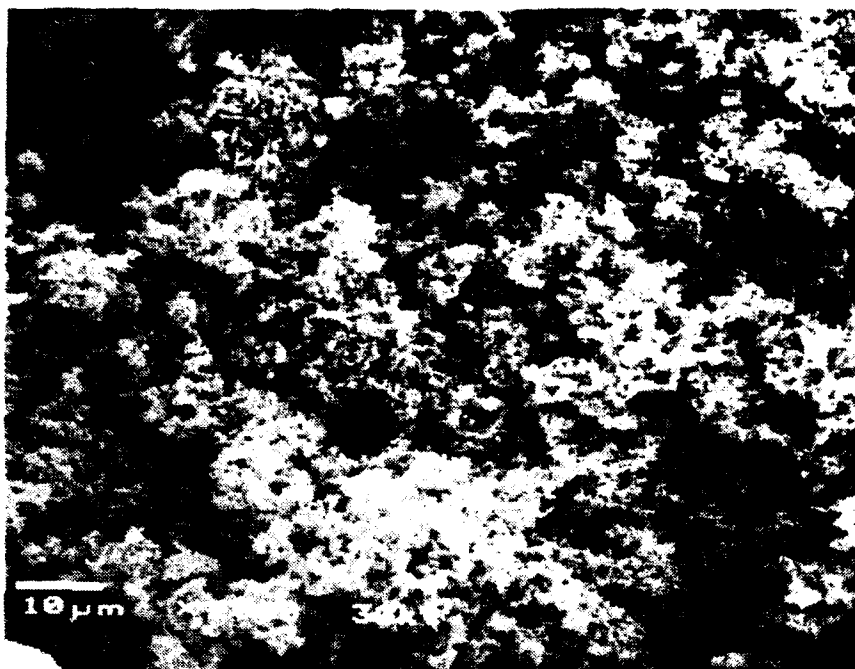
Figure 6: Tensile Specimen Machining Specifications

Steric repulsive forces between solid particles can be produced in the liquid medium by the use of strong surfactants or dispersing agents. These surfactants adhere to the surface of the metallic powders and generate repulsive forces that prevent agglomeration and maintain the powder suspended in the liquid medium for long periods of time. This adsorption lowers the attractive influence of the Van der Waals-London forces to a great extent. The ability to produce a uniform mixture which remains stable over a long period of time depends also strongly on the particle size and size distribution of the particles. Small particle size, in the range of <1-2 microns, are preferable for the purpose of suspension and mixing purposes of multicomponent composites. Such particle sizes however may suffer from low purity and oxygen contamination.

Tungsten powders were purchased from a commercial source (Johnson Matthey). The powder has a particle size of 0.6 - 0.9 microns, a purity of 99.9% (manufacturer specification), and a surface area of 1.5g/m². SEM micrographs of the as-received tungsten powder are shown in Figure 7.

Dispersion of the W powder was examined in the following organic solvents: methanol, isopropanol, toluene, and hexane. The dispersions were examined in test tubes 100mm long, 15mm diameter. The tubes were filled with the selected powder/ solvent/ dispersant mixture, sealed and then hand shaken for five minutes before being placed vertically onto a rack for settling. The dispersion was measured by the size of the different zones in the settling tube. The three observed zones were the "supernatant" or clear liquid where all particles were settled, the "falling" zone where the particles were still floating but settling and the "sediment" zone where the particles have settled and packed into a cake. Primary emphasis was given to the packing of the sediments and the transparency of the falling zone.

(a)



(b)

Figure 7. SEM micrographs of as-received raw tungsten powders.

The non-polar solvents, toluene and hexane, exhibited very poor ability to suspend the W powder. Complete sedimentation of the powder was reached within a few minutes, see Figure 8a. The more polar solvents showed better ability to suspend the W powder with isopropanol having a darker color of the falling zone as compared to methanol. The darker color is an indication of the larger number of particles in suspension. A plot of the sedimentation results as a function of time is shown in Figure 8b where the smaller sediment height for polar solvents is indicative of better packing density (well dispersed powders pack better).

The conclusion drawn from the above experiments is that isopropanol is the most effective solvent for dispersion of the tungsten powder. However, to isolate the effect of the dispersant alone on the steric stabilization of the W particles, different dispersants were added to a non-polar solvent (toluene). In each of the test tube containing 3g of W powder and 20 cc of toluene, 10 droplets of dispersant were added (~4.0% dispersant). The dispersants tested were Polyvinylpyrrolidone with molecular weights of 15,000, 30,000 and 40,000 (commercially referred to as PVP 15, PVP 30 and PVP 40 respectively), Solsperse 20,000 and 24,000. The rate of change of the 'clear zone' and the 'sediment' height is reported here in Figure 9 as a function of the settling time. From Figure 9a, it is clear that when no dispersant was used, almost all the tungsten powder settled immediately thereby leaving a large clear zone; this is indicative of poor dispersion since the tungsten particles agglomerate into larger clusters which settle at high velocities. By contrast, all the dispersants, by preventing the agglomeration into larger clusters, were effective in stabilizing the suspension. Figure 9b shows the rate of change of the 'sediment' height at the bottom of the tube as a function of settling time. Well-dispersed powders pack better (undispersed powders leave empty spaces in their packing thereby decreasing the density of packing), a

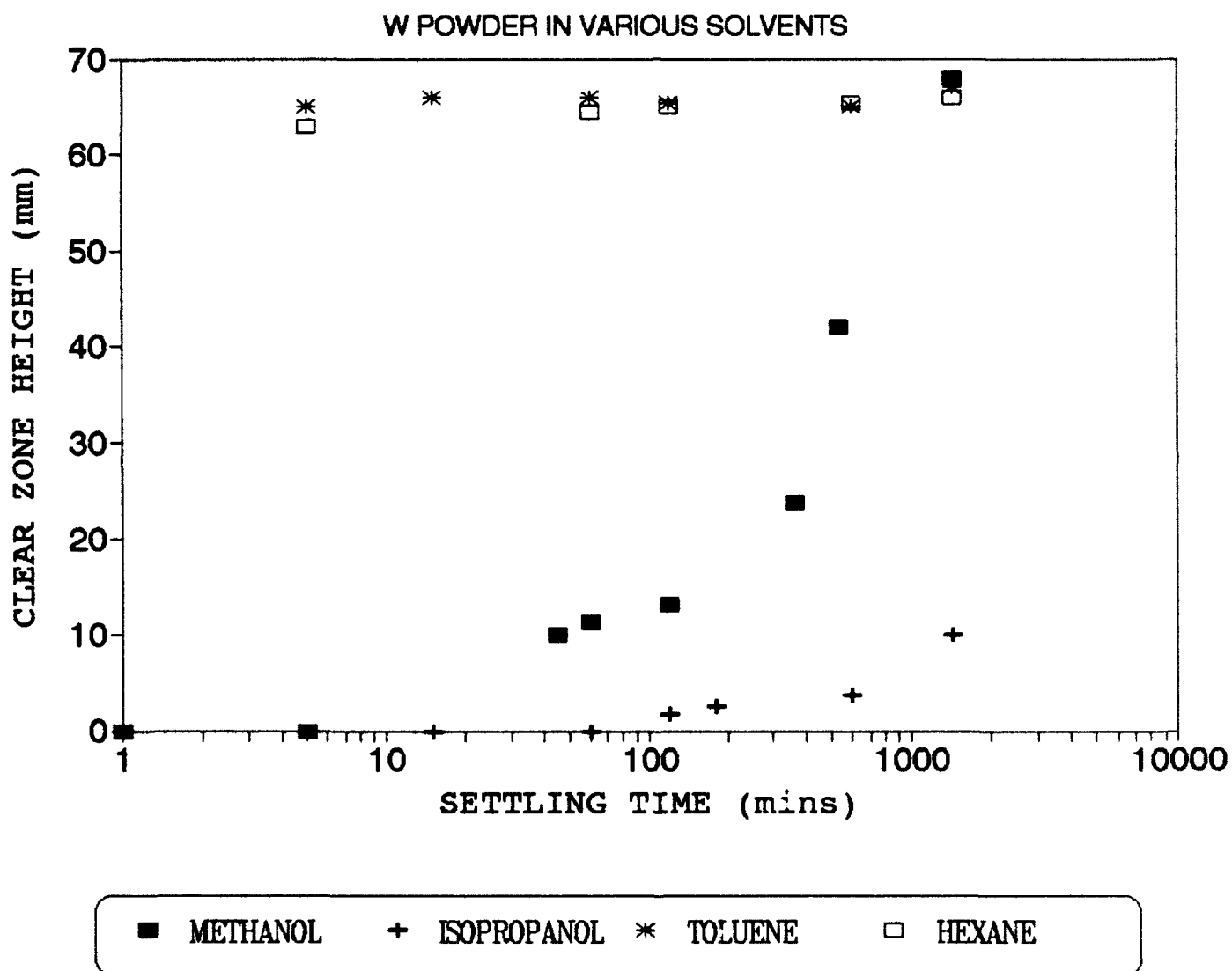


Figure 8a: Settling behavior of Tungsten powder suspended in different organic solvents.

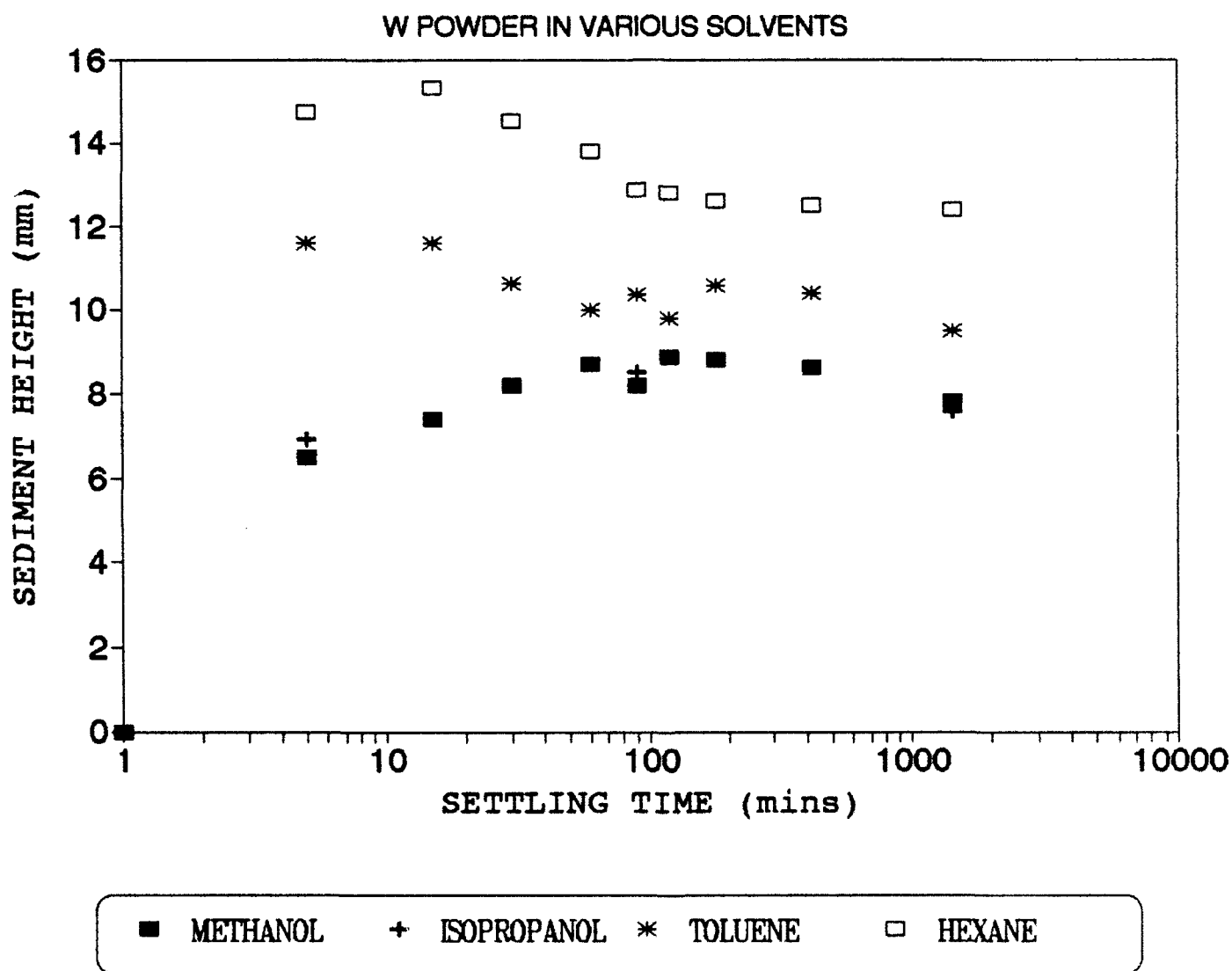


Figure 8b. Rate of change of sediment height (packing density) for W powders suspended in various organic solvents. Both methanol and isopropanol yield good packing.

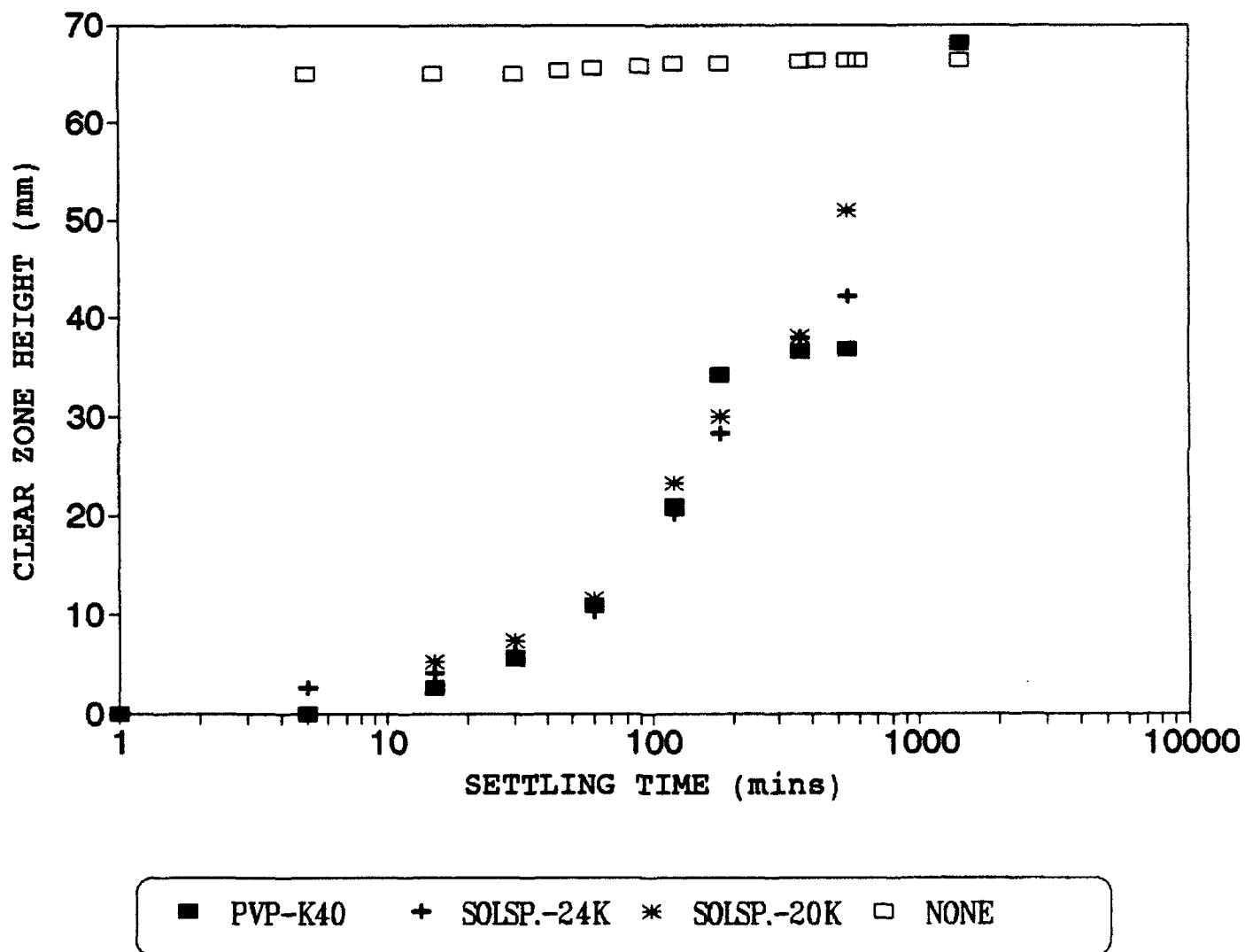


Figure 9a. Rate of change of 'clear zone' height with settling time for tungsten powders dispersed in toluene with and without dispersants.

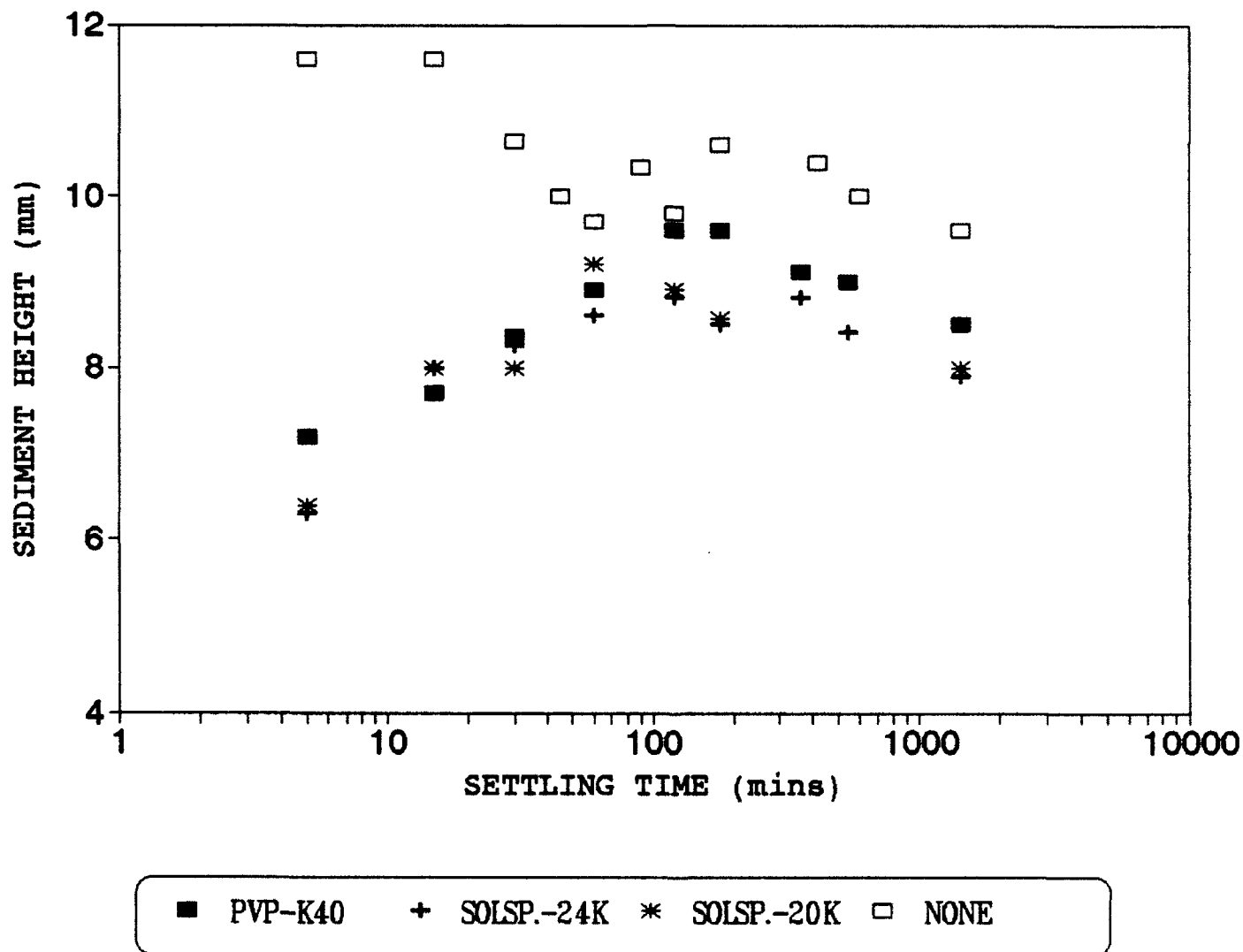


Figure 9b. Rate of change of 'sediment' height with settling time for tungsten powders dispersed in toluene with and without dispersants.

smaller sediment height is indicative of better dispersion. The data indicates that Solsperse 24000 and Solsperse 20,000 are very effective in dispersing the tungsten powders even in a non-polar media like toluene. These dispersants were determined to be the best for dispersing tungsten powders. It should be noted that Solsperse 24,000 is insoluble in isopropanol, hence, Solsperse 20,000 was chosen as the dispersant for further experimentation with isopropanol.

The dispersion of the powder was also checked as a function of dispersant content. It was found that a 2 wt% was sufficient. Among the polyvinylpyrrolidones tested, the higher molecular weight showed dispersion comparable to that of Solsperse 20,000.

While the dispersion of the major phase is the most critical in maintaining a homogeneous microstructure, the dispersion of the matrix phase(s) (Ni_3Al and Ni-12 at % Al - 40 at % Fe) are also very important in maintaining uniform distribution of the liquid phase during sintering. The particle size of the Ni_3Al powder was found to be in the range of 50 - 100 μm which was considered unsuitable for our purposes. Ball milling in a planetary mill was utilized to grind some of the coarse powders into finer fractions. The Ni - 12 at % Al - 40 at % Fe powder was considered acceptable even though it was rather coarse (5 - 10 microns) for our purposes. The powders were ball milled in steel jars to generate a high volume fraction of submicron sized which we consider to be the optimum particle size to generate a uniform distribution of the liquid phase during sintering.

Dispersion of the as-received intermetallic powder was examined using the dispersant 'Solsperse 20,000' in isopropanol. Although the dispersant helped considerably in the stabilization of the suspension (over that of isopropanol alone), it was not as successful as with the tungsten, primarily due to the larger particle size of the intermetallic powders. Large particles are very difficult to keep in suspension due to their large mass. Upon

grinding the intermetallic powders to finer fractions, the suspension achieved was excellent. SEM micrographs of as-received Ni-12Al-40Fe and Ni₃Al powders are shown in Figure 10.

The separation of finer fractions of powder from the bulk of the Ni - 12 at % Al - 40 % at Fe after ball milling was done by sedimentation techniques in isopropanol, after a well mixed and stable suspension was achieved. The settling velocity of the powder in the solvent was calculated based on Stokes law of free fall in a liquid medium:

$$U_f = \frac{gD_p^2 (\rho_p - \rho)}{18\mu}$$

μ is the medium viscosity (Pa.s),

g is the gravity (m/s²),

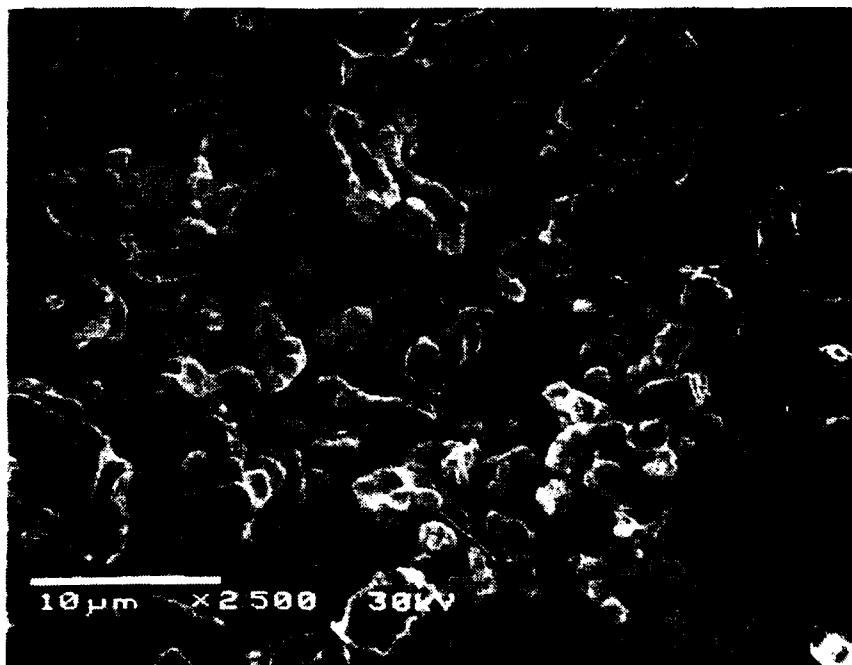
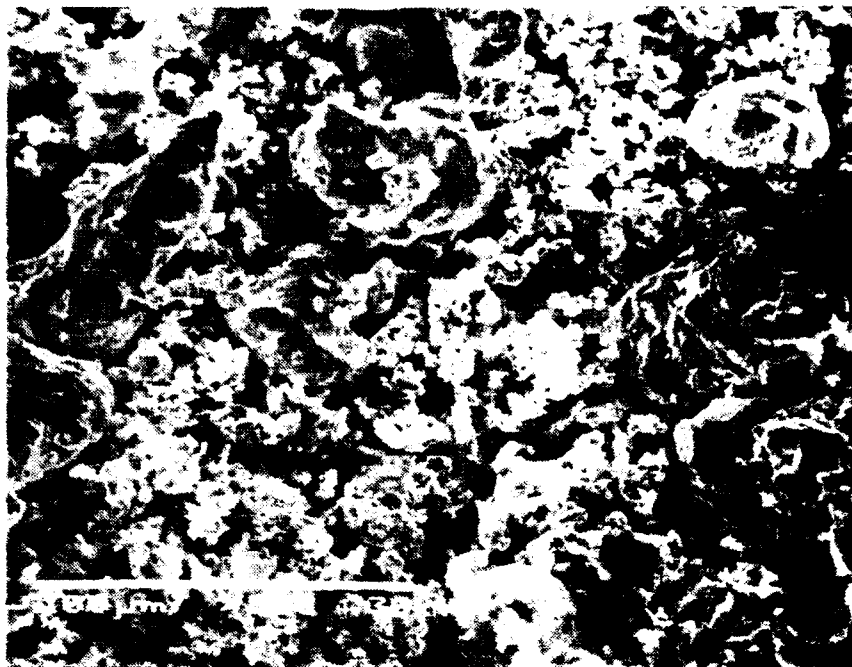
D_p is the particle diameter (m),

ρ_p is the density of the particle (kg/m³),

and ρ the density of the solvent (kg/m³).

Separation of fine particles of Ni-12Al-40Fe by sedimentation was done using a two foot tall separation column. Collection of the fines from the solvent was performed at 6000rpm in a centrifuge. Micrographs of the finer fractions indicated a narrow particle size distribution, and a particle size of approximately 3 μ m.

(a)



(b)

Figure 10. SEM micrographs of as-received intermetallic powders of (a) Ni₃Al-0.02B (b) Ni-12Al-40Fe(at.%).

B. Powder Processing

1. Mixing

The effect of the processing parameters, especially those of mixing and compaction, on the final density and porosity, were investigated for the purpose of obtaining good compositional uniformity. A series of statistically designed set of experiments were carried out according to a two-level factorial design. A total of five process variables were investigated: mixing speed of the roller mill, the mixing charge-ratio which is the ratio of mixing media to added powder, the time of mixing, the mixing medium (dry vs. methanol) and the type of mixing media (tungsten carbide vs. stainless steel). The main objective of the first part of this statistical design is to locate and explore the region of maximum response. The mixing parameters were evaluated based on the sintered densities of the individual specimens as they were measured by the water displacement method. Table I shows the experimental design matrix along with the values of the liquid-phase sintered densities.

For the purpose of evaluation of these various statistically designed experiments, the as-received powder of Ni-12at%Al-40at%Fe was utilized due to its smaller particle size ($5\text{-}10\mu\text{m}$) as compared to Ni_3Al ($10\text{-}50\mu\text{m}$). The powders were dry pressed in stainless steel dies at a pressure of 275 MPa (similar to cold-compaction pressures usually reported in the literature for WHA). The samples were pressed in dimensions of 0.25" in diameter, 0.12" - 0.13" in thickness, having a mass of $\sim 1\text{g}$. The samples were placed inside an aluminum oxide crucible and were surrounded by -20 mesh aluminum oxide particles. All the specimens were sintered under identical conditions. The samples were sintered inside a resistance heated graphite furnace. The sintering profile is shown in Figure 5.

**Table I. Statistical Experimental Design Applied to Optimize Mixing Process
Experimental Approach and Resultant Sintered Densities**

Sample #	Rot Speed 1=Fast 2=Slow	Charge Ratio 1=20:1 2=4:1	Time 1=1 hr 2=4 hrs	Solvent 1=Dry 2=MeOH	Milling Media 1=WC 2=Steel	Bulk Density
1	1	1	1	1	1	17.42
2	1	1	1	1	2	16.84
3	1	1	1	2	1	
4	1	1	1	2	2	17.34
5	1	1	2	1	1	17.78
6	1	1	2	1	2	17.06
7	1	1	2	2	1	17.57
8	1	1	2	2	2	18.40
9	1	2	1	1	1	17.16
10	1	2	1	1	2	17.16
11	1	2	1	2	1	17.83
12	1	2	1	2	2	17.80
13	1	2	2	1	1	17.48
14	1	2	2	1	2	17.25
15	1	2	2	2	1	17.50
16	1	2	2	2	2	16.89
17	2	1	1	1	1	17.70
18	2	1	1	1	2	17.60
19	2	1	1	2	1	17.86
20	2	1	1	2	2	17.71
21	2	1	2	1	1	17.38
22	2	1	2	1	2	16.72
23	2	1	2	2	1	17.33
24	2	1	2	2	2	17.82
25	2	2	1	1	1	17.22
26	2	2	1	1	2	16.51
27	2	2	1	2	1	17.97
28	2	2	1	2	2	17.11
29	2	2	2	1	1	17.21
30	2	2	2	1	2	16.74
31	2	2	2	2	1	17.08
32	2	2	2	2	2	16.96

For reduction of the oxide layer on the tungsten particles, the samples were held at $\sim 800^{\circ}\text{C}$ for 1 hour in dry hydrogen. The temperature was then raised $10^{\circ}\text{C}/\text{min}$ to the sintering temperature of 1550°C (chosen based on the melting temperature) and held there for 35 minutes. Midway through the soak at the sintering temperature, the gas atmosphere was changed to argon. Following completion of sintering, the samples were then cooled $5^{\circ}\text{C}/\text{min}$ to 1200°C and then furnace cooled to room temperature.

The sintered samples were cleaned and then were boiled in water for two hours. Their densities were measured using the Archimedes principle and are also shown in Table I. The results were analyzed using a statistical computer program. The analysis provided both descriptive and inferential statistics. The conditions which represented each of the independent variables were compared individually with the sintered density using a t-test of independent means. The t-test is a measurement of significance level of the results to reject the null hypothesis. T-test results of 5% or less are considered statistically significant. The results are shown in Table II for each of the independent variables. From the five independent variables listed above only the solvent (dry vs methanol) has a statistically significant effect on the densities since the 2-tail probability is $<5\%$. Consequently, the use of solvent, in this case methanol, as processing variable for mixing has a strong effect in densification of the tungsten alloys. The charge ratio of 20:1 may have some significance but this cannot be strongly supported from these results, as the null hypothesis cannot be rejected. No other variable has any significant impact on the densification of the tungsten alloys.

**Table II. Results of Statistical Analysis of
Mixing Process Optimization**

INDEPENDENT VARIABLE	NUMBER OF CASES	MEAN	STANDARD DEVIATION	2-TAIL PROBABILITY
ROT SPEED Group 1 = fast Group 2 = slow	15 16	17.4297 17.3074	0.409 0.444	43.1%
CHARGE RATIO Group 1 = 20:1 Group 2 = 4:1	15 15	17.5008 17.2407	0.425 0.397	9%
TIME Group 1 = 1 hour Group 2 = 4 hours	15 16	17.4145 17.3216	0.419 0.439	55.2%
SOLVENT Group 1 = dry Group 2 = MeOH	16 15	17.2002 17.544	0.363 0.424	2.3%
MILLING MEDIA Group 1 = WC Group 2 = SS	16 15	17.4773 17.2484	0.282 0.522	14.7%

i. Compaction of Powder Mixtures

A separate set of experiments were run to examine the effect of compaction pressure on both the green and sintered densities of the samples 95%W-5%(Ni-12Al-40Fe) (AR = as-received powder) and 95%W - 5%Ni₃Al (fine powder obtained by ball milling the coarse, as-received powder). About 7.5g of powder per sample were compacted in stainless steel dies at pressures ranging from 10,000 psi (68.9 MPa) to 60,00 psi (413.7 MPa). These samples were run in ultra-high purity argon gas with a heating rate of 13°C/min to 1600°C and a hold time at maximum temperatures of 42 minutes. The green and sintered densities of the samples are shown in Table III and plotted in Figure 11. The compaction pressure has a big effect on the green density. For the sample of 95%W + 5%Ni-12Al-40Fe (AR), the green density is 8.593 g/cc at 10 ksi and increases to 10.348 g/cc at 60 ksi which is about 10% increase in theoretical density. However, the higher green densities do not necessarily correspond to higher sintered densities. It was decided to use a compaction pressure of 40

ksi (275 MPa) for all future work in order to be consistent with the values reported in the literature.

Table III: Summary of Results of Effect of Compaction Pressure on Green and Sintered Densities of Tungsten Alloys.

Dry Pressing in Steel Die at Room Temperature ½" Diameter Die

PRESSURE (Ksi)	GREEN DENSITY (g/cc)	SINTERED DENSITY (g/cc)
W + 5%NiFeAl (As-received)		
10	8.520425	17.14027
10	8.666391	17.2016
20	9.168474	17.05892
20	9.145876	17.28548
30	9.537441	17.11977
30	9.567568	
40	9.943954	17.05309
40	9.976259	17.13846
60	10.38905	

PRESSURE (Ksi)	GREEN DENSITY (g/cc)	Sintered DENSITY (g/cc)
W + 5%Ni ₃ Al (FINES)		
10	7.99386	
10	7.907074	17.32774
20	8.326402	17.28309
20	8.470943	16.93843
30	8.854754	16.87638
30	8.795686	16.69349

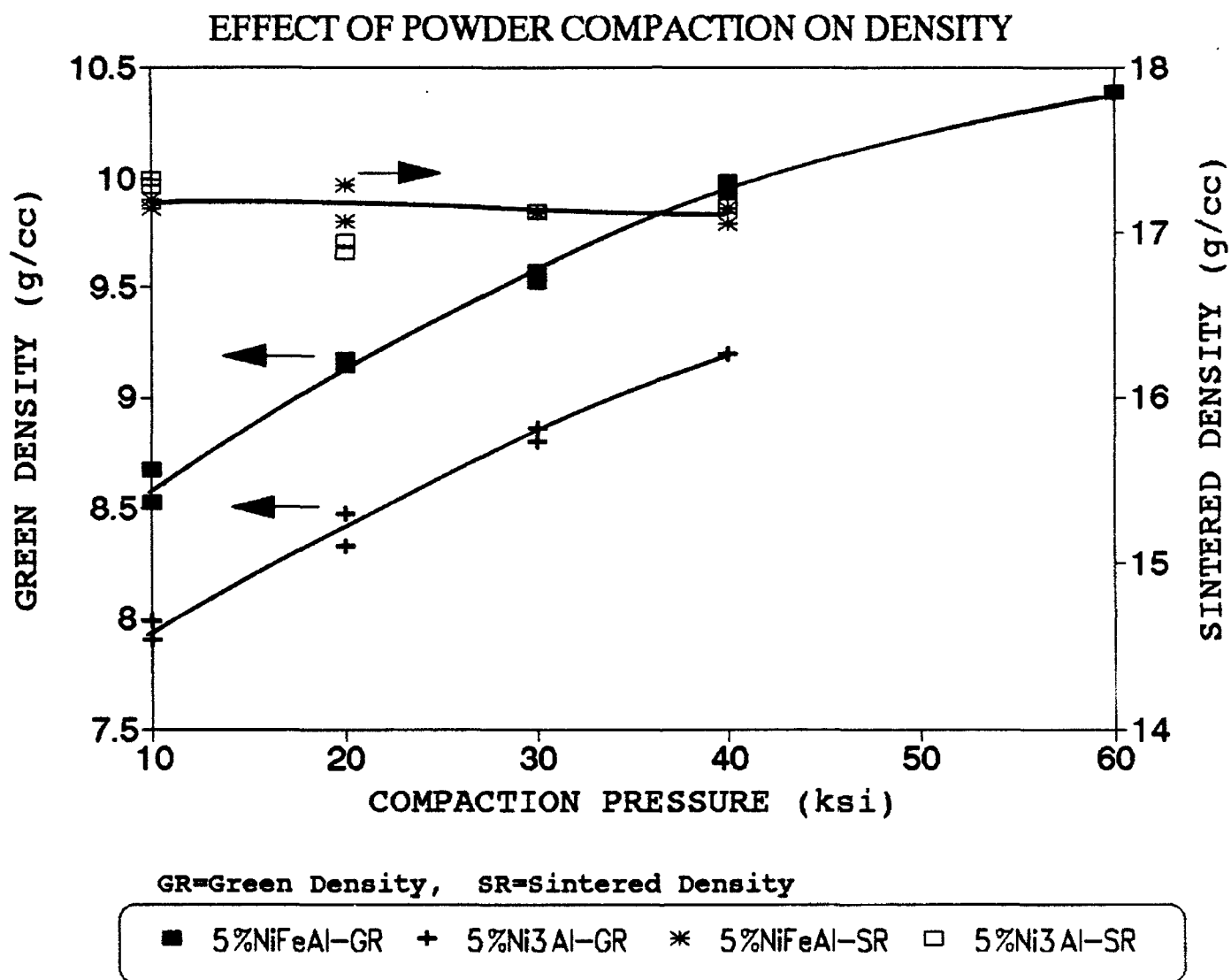


Figure 11: Plot of Compaction Pressure vs. Green and Sintered Density of Tungsten Alloys.

C. Consolidation

1. Pressureless Sintering

The major parameters that needed to be optimized for these alloys were atmosphere, sintering temperature and time. The atmosphere plays a vital role in purity, formation of by-products, and elimination of porosity in the sintered microstructure, and could involve various furnace environments over a single sintering cycle. The main goals in selecting atmosphere were:

- the removal of the oxide layer present on the surface of the tungsten powder by the use of dry hydrogen;
- removal of gaseous oxide decomposition species from the samples by the application of vacuum, and
- suppression of water vapor formation by the reaction of the oxide decomposition products with dry hydrogen. This was found to be eliminated by using wet hydrogen during liquid-phase sintering.

Sintering temperature and time are important in achieving dense samples with small grain size and a uniform microstructure.

i) **Atmosphere:** The three main sintering atmospheres which were investigated are:

Atmosphere A. (Dry H₂/Ar): Dry hydrogen (dew point -55°C) until the first half of the sintering temperature soak, followed by a switch to dry argon.

Atmosphere B. (Dry H₂/wet H₂/Ar): Dry hydrogen (dew point -55°C) until 1250°C, followed by a switch to wet hydrogen (dew point +30°C) until the first half of the sintering temperature soak, followed by a switch to dry argon.

Atmosphere C. (Dry H₂/vacuum/Ar): Dry hydrogen (dew point -55°C) until 1250°C, followed by a switch to vacuum until the end of the sintering temperature soak, followed by a switch to dry argon.

Samples tested under these conditions were dry pressed at 40 Ksi in ½" diameter die. Sintering temperature was 1550°C for 35 minutes. Densities of the samples were measured using the Archimedes principle. The results are shown in Table IV. Samples run in Atmosphere C (dry H₂/Vac/Ar) gave the highest densities. Some densities are well above the expected maximum density. The sample W + 5% Ni₃Al (fines) had a density of 18.53 (±0.21) g/cc which is well above the maximum theoretical density (103.5%). The higher densities observed could be explained due to the vacuum atmosphere in which the matrix phase as a whole or elements from the matrix are evaporated during the high temperature sintering. A number of samples sintered using Atmosphere C showed swelling. Samples run in Atmosphere B (dry H₂/wet H₂/Ar) gave the lowest densities for every sample category tested. Due to the low densities of Atmosphere B, and the swelling of Atmosphere C, it was concluded that Atmosphere A would be the most suitable for pressureless sintering the W-intermetallic alloys.

Several samples of 95W-5 (7Ni+3Fe) were also examined as shown in Table IV for comparison of density that reported in the literature. Near theoretical densities were achieved in these samples as well as in the samples utilizing the intermetallic matrix. The Ni-Fe mixture in the ratio of 7-3 or 8-2 are the main matrices used in the past to densify W-heavy alloys. The densities obtained from these samples are comparable to reported literature values.

ii) Temperature and Time

A set of eleven sintering experiments were carried out to examine the effect of sintering temperature and time on the density, grain size of the tungsten, and amount of phase separation. Atmosphere cycle A (dry H_2/Ar) was used for all of these experiments. After sintering the densities of the samples were measured by the water displacement method. The results are shown in Table V. Each data point represents three values, the average is taken to be the experimental value. The standard deviation is shown in parenthesis. The grain size was measured using SEM micrographs of polished specimens. For each sample, a picture of 500X magnification was taken. The number of grains within that picture was measured. The area represented in that picture was measured to be $41,400 \mu m^2$. This area was multiplied by 0.9 to account (approximately) for the area occupied by the tungsten grains, $37,260 \mu m^2$. This area was then divided by the number of grains counted. The grain area was then converted into diameter assuming a circular shape of the grains, $diameter = (4a/\pi)^{1/2}$.

Although the data is not complete, the results shown in Table V, indicate that both temperature and time have some effect on the densities and W particle size in these composites. The effect of time appears to be stronger at the lower temperatures $< 1500^\circ C$, but weaker above a threshold temperature, $1500^\circ C$. Time however, has a rather strong effect on the W particle size, for example at $1550^\circ C$, the average W particle size is $21 \mu m$ for 30 minutes soak time and $17.7 \mu m$ for five minutes soak time. SEM micrographs of samples 230 and 233 are shown in Figure 12a-b. SEM micrographs of samples 65 and 61 are shown in Figure 12c-d. The dark spots appearing in Figures 12 are aluminum rich phase

**Table IV: Cumulative Results of Pressureless Sintering
of the Tungsten Heavy Alloys at Three Different Atmospheres**

SAMPLE COMPOSITION	Theoretical Density (g/cc)	ATMOSPHERE		
		A dry H ₂ /Ar (g/cc)	B dry H ₂ /wet H ₂ /Ar (g/cc)	C dry H ₂ /Vac/Air (g/cc)
W + 5% Ni ₃ Al (AR) W + 5% Ni ₃ Al (fines)	17.89	18.01 (± 0.04)	16.31 (± 0.20) 16.88 (± 0.14)	18.00 (± 0.19) 18.53 (± 0.21)
W + 5% NiFeAl (AR) W + 5% NiFeAl (fines)	17.89	17.597 (± 0.17)	17.32 (± 0.18)	18.03 (± 0.18) 17.20 (± 0.13)
W + 5% (7Ni + 3Fe)	18.16		17.90 (± 0.18)	
Pure W	19.3	15.65 (± 0.27)	15.50 (± 0.20)	16.21 (± 0.51)

AR - As-received powder

Fines = Ball-milled powder - fines fraction used

**Table V: Results of Densities for Experiments of
Sintering Temperatures and Time for the Tungsten Alloy**

Sample #	Temp./Time (°C/mins)	Sample Composition	Sintered Density (g/cc)	Grain Intercept. (μm)
64,65,66 61,62,63 67,68,69	1600/30	W + 5% Ni ₃ Al(BM-fines) W + 5% NiFeAl (AR) W	18.01 (± 0.04) 17.597 (± 0.17) 15.65 (± 0.27)	22 20
188,189,190 194,195,196 191,192,193 197,198,199	1550/15	W + 5% Ni ₃ Al(AR) W + 5% Ni ₃ Al(BM-fines) W + 5% NiFeAl(AR) W + 5% NiFeAl(BM)	16.537 (± 0.108) 17.383 (± 0.08) 17.40 (± 0.06) 17.40 (± 0.24)	
226,227,228 232,233,234 229,230,231 235,236,237	1550/5	W + 5% Ni ₃ Al(AR) W + 5% Ni ₃ Al(BM-fines) W + 5% NiFeAl(AR) W + 5% NiFeAl(BM)	16.917 (± 0.14) 17.516 (± 0.04) 17.507 (± 0.04) 17.692 (± 0.06)	17.44 17.78 17.38 18.34
176,177,178 182,183,184 179,180,181 185,186,187	1500/45	W + 5% Ni ₃ Al(AR) W + 5% Ni ₃ Al(BM-fines) W + 5% NiFeAl(AR) W + 5% NiFeAl(BM)	16.651 (± 0.06) 17.59 (± 0.28) 17.47 (± 0.11) 17.62 (± 0.07)	
139,140,141 145,156,147 142,143,144 148,149,150	1500/30	W + 5% Ni ₃ Al(AR) W + 5% Ni ₃ Al(BM-fines) W + 5% NiFeAl(AR) W + 5% 7Ni+3Fe	16.60 (± 0.24) 17.57 (± 0.12) 17.54 (± 0.18) 17.92 (± 0.25)	23.9 23.3 27.2

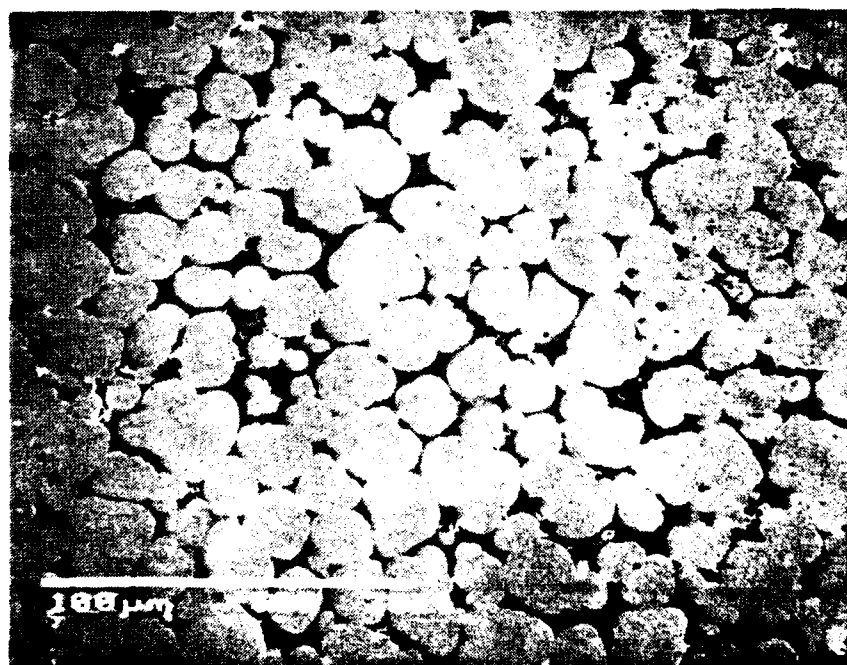
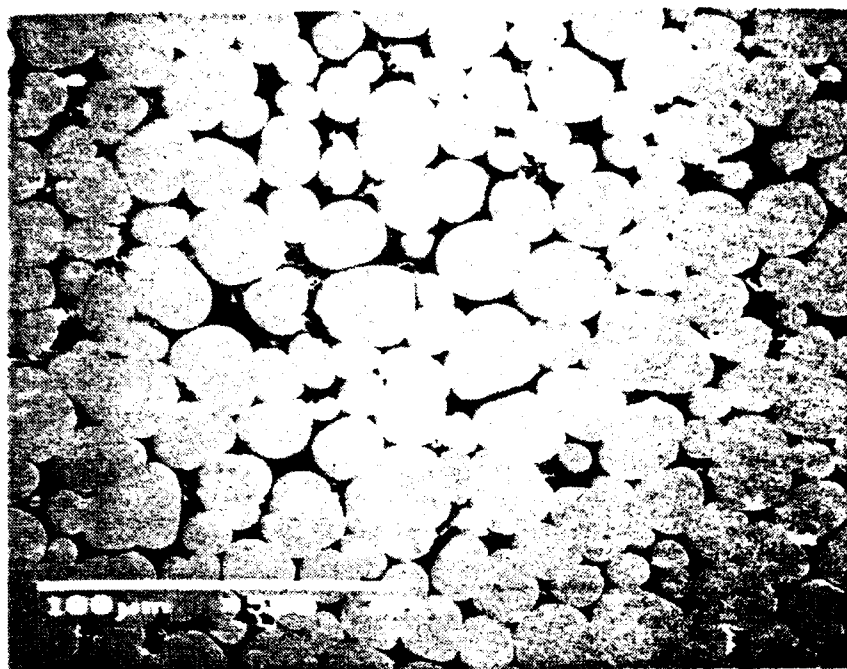
Table V (Cont.)

Sample #	Temp./Time (°C/mins)	Sample Composition	Sintered Density (g/cc)	Grain Intercept. (μm)
203,204,205 206,207,208 200,201,202 209,210,211	1500/15	W + 5% Ni ₃ Al(AR) W + 5% Ni ₃ Al(BM-fines) W + 5% NiFeAl(AR) W + 5% NiFeAl(BM)	16.62 (± 0.12) 17.53 (± 0.06) 17.21 (± 0.49) 17.60 (± 0.11)	
163,164, 165 170,171,172 166,167,168 175 172,173,174	1450/60	W + 5% Ni ₃ Al(AR) W + 5% Ni ₃ Al(BM-fines) W + 5% NiFeAl(AR) W + 5% NiFeAl(BM) W + 5% (7Ni+3Fe)	16.568 (± 0.24) 17.631 (± 0.20) 17.562 (± 0.23) 16.569 17.987 (± 0.25)	36.8 23.1 24.5 18.3 28.8
115,116,117 121,122,123 118,119,120 124,125,126	1450/30	W + 5% Ni ₃ Al(AR) W + 5% Ni ₃ Al(BM-fines) W + 5% NiFeAl(AR) W + 5% (7Ni+3Fe)	16.577 (± 0.16) 17.118 (± 0.09) 17.391 (± 0.11) 17.828 (± 0.15)	
212,213,214 218,219,220 215,216,217 221,222,223 224,225	1450/15	W + 5% Ni ₃ Al(AR) W + 5% Ni ₃ Al(BM-fines) W + 5% NiFeAl(AR) W + 5% NiFeAl(BM) W + 5% (7Ni+3Fe)	16.781 (± 0.21) 17.368 (± 0.58) 17.251 (± 0.15) 17.424 (± 0.13) 18.05 (± 0.07)	
151,152,153 157,158,159 154,155,156 160,161,162	1400/60	W + 5% Ni ₃ Al(AR) W + 5% Ni ₃ Al(BM-fines) W + 5% NiFeAl(AR) W + 5% NiFeAl(BM)	16.558 (± 0.21) 17.626 (± 0.06) 17.602 (± 0.20) 17.294 (± 0.04)	23.9 16.9
127,128,129 133,134,135 130,131,132 136,137,138	1400/30	W + 5% Ni ₃ Al(AR) W + 5% Ni ₃ Al(BM-fines) W + 5% NiFeAl(AR) W + 5% (7Ni+3Fe)	16.258 (± 0.11) 17.407 (± 0.11) 17.282 (± 0.06) 17.93 (± 0.14)	

AR = As-received powder

BM = Ball-milled ≥ 4 hoursBM-fines = Ball-milled ≥ 4 hours, fines fraction used

(a)

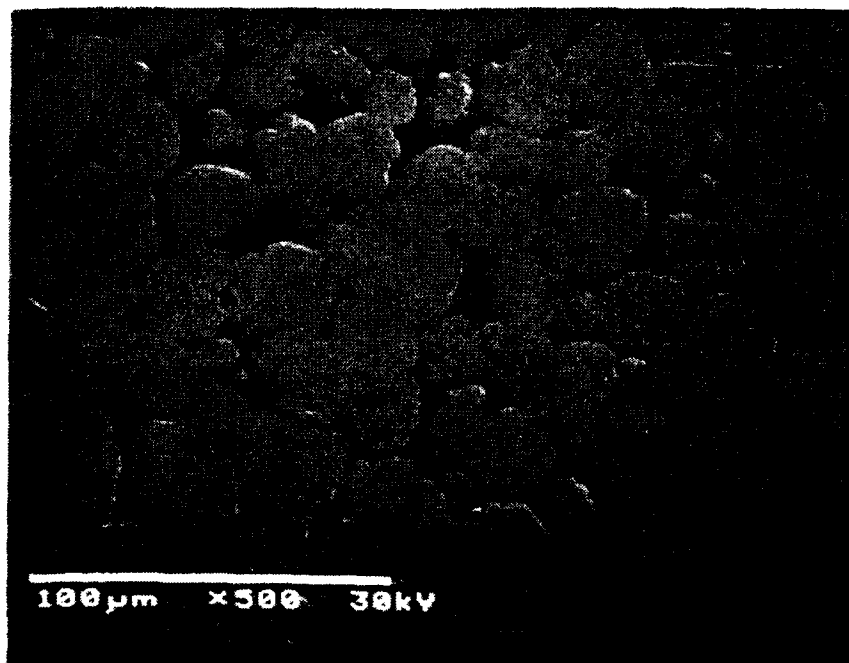
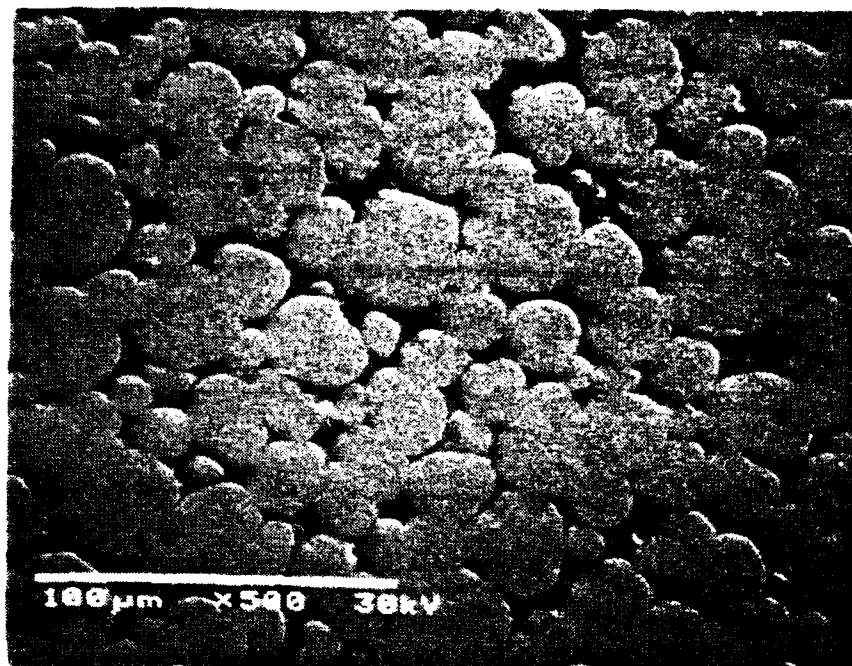


(b)

Figure 12a-b.

SEM micrograph of WHA specimens sintered at 1550°C/5mins with 5wt.% intermetallic powder starting with (a) as-received NiFeAl powder (b) ball-milled Ni₃Al powders.

(c)



(d)

Figure 12c-d. SEM micrograph of WHA specimens sintered at 1600°C/30mins with 5wt.% intermetallic powder starting with (a) as-received NiFeAl powder (b) ball-milled Ni₃Al powders.

which was precipitated out during sintering. Further analysis of the samples is subsequently discussed in another section.

2. Hot Pressing

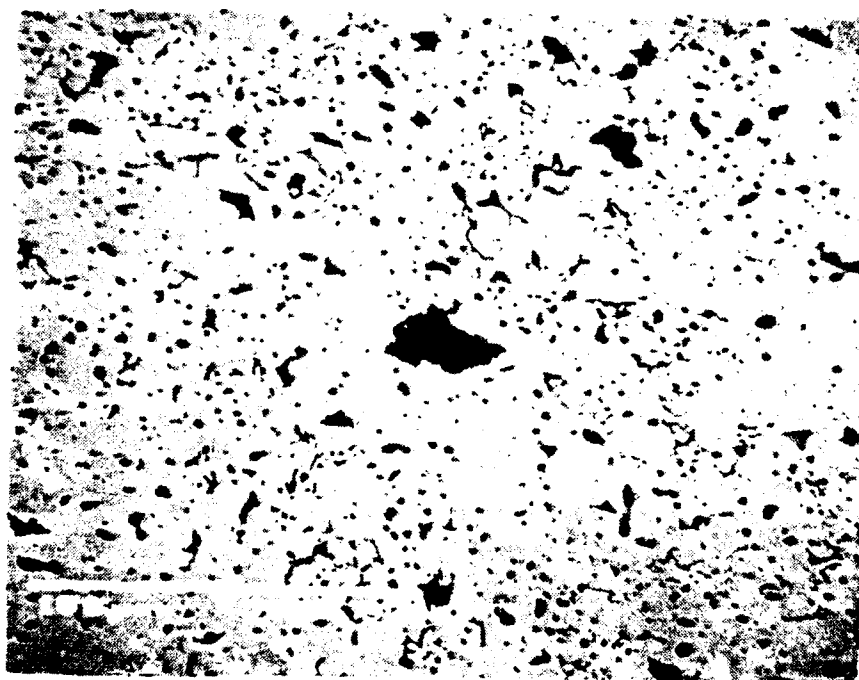
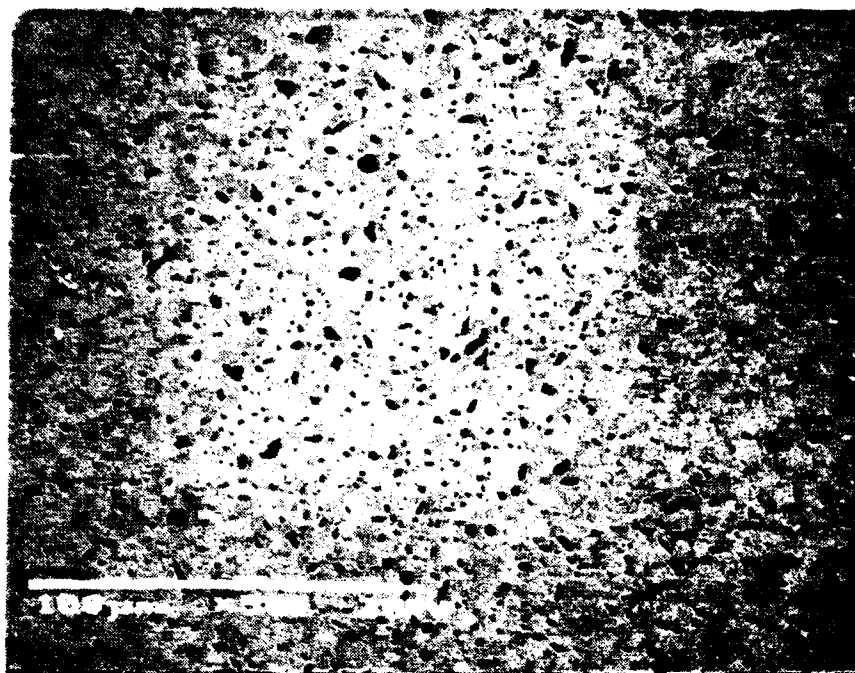
Consolidation of the WHA was also pursued by means of hot pressing. One major anticipated advantage of hot pressing was the lower temperature needed for consolidation. The application of pressure can force pack the tungsten alloy to full density. The powder mixtures were loaded into graphite dies. Hot pressing conditions were a maximum temperature of 1400°C and an applied pressure of 51.7 MPa (7.5 ksi), under a 95%Ar-5%H₂ atmosphere.

After hot pressing the samples were removed from the dies and cleaned from the grafoil spacers. The samples were unusually hard indicating that a reaction with the grafoil had taken place forming tungsten carbide. The density of the sample with W-5wt.% NiFeAl was 16.054 g/cc (± 0.08) which was significantly lower than for samples of similar composition processed by pressureless sintering. SEM analysis of the samples showed a very different microstructure compared to the pressureless sintered samples. The samples showed no clear separation between the W grains and an aluminum rich phase was observed to have separated out. SEM micrographs of the microstructure of the hot pressed specimen is shown in Figure 13.

D. Microstructural Analysis

The superlattice {100} and {110} reflections in the x-ray diffraction patterns for as-received Ni₃Al powders shown in Figures 14a indicate an ordered structure, although their intensity is low. In contrast to Ni₃Al, the x-ray diffraction pattern for Ni-12Al-40Fe(at.%) does not exhibit these {100} and {110} superlattice reflections (Figure 14b), presumably due to the reduced difference in atomic scattering factors when Fe substitutes for Al in the lattice (their absence does not indicate a disordered structure). X-ray diffraction patterns

(a)



(b)

Figure 13. SEM micrographs of hot pressed specimens with 5wt% intermetallic powder
a) ball-milled Ni_3Al powder, b) as-received NiFeAl .

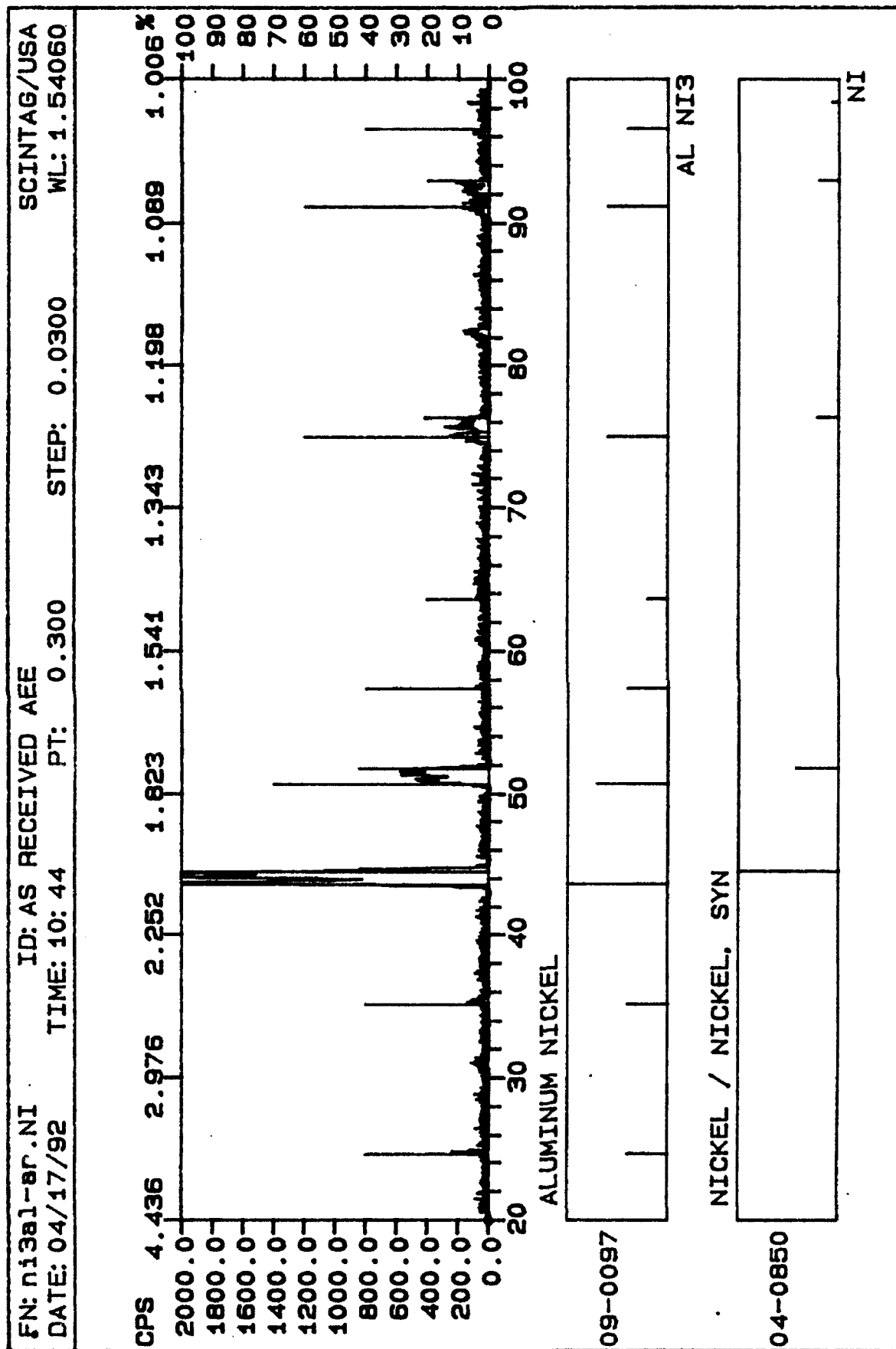


Figure 14a X-ray diffraction pattern of as-received Ni_3Al intermetallic powder.

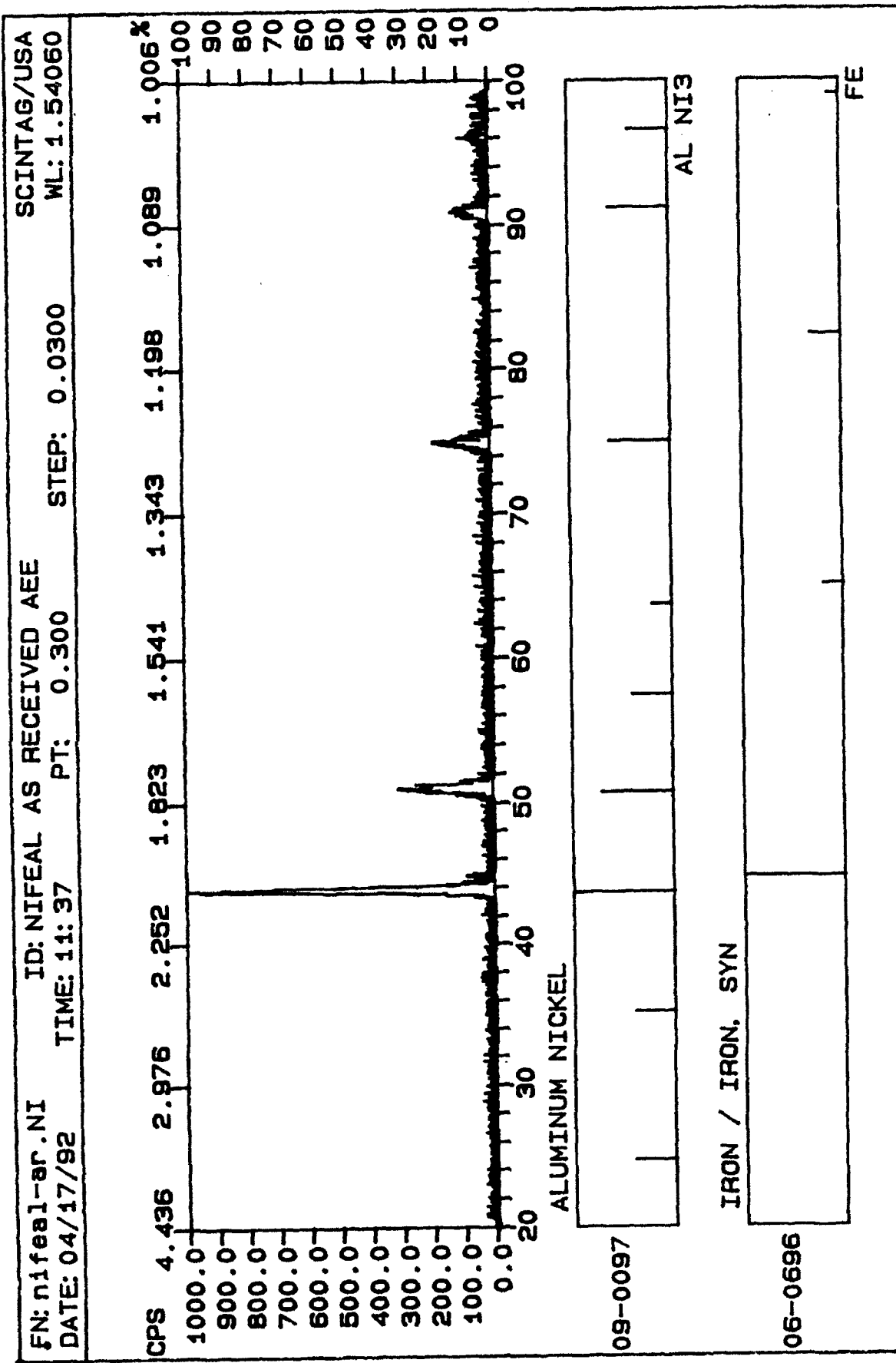


Figure 14b X-ray diffraction pattern of as-received Ni-12Al-40Fe intermetallic powder.

from the as-received intermetallic powders indicated that some free-Ni was present in the as-received Ni_3Al powders while the NiFeAl powder did not contain any free Fe (see Figures 14a-b). The microstructures and some x-ray diffraction patterns for the as-sintered WHA with various weight fractions and types of intermetallic matrices are shown below in Figures 15-20. For comparison purposes, the microstructures of conventional WHA (with Ni-Fe matrix), processed similar to the intermetallic-based WHA are shown in Figure 21. Only two intermetallic matrices were investigated: boron-microalloyed Ni_3Al and Ni-12at.%Al-40at.%Fe. Four different weight fractions of intermetallic matrices were investigated namely 3%, 5%, 7% and 10%. For the conventional WHA, a 8:2 Ni-to-Fe ratio was chosen (since it has recently been reported to exhibit better quasi-static properties than the 7:3 ratio) and only two weight fractions namely 7% and 10% were investigated.

Typical low magnification SEM micrographs corresponding to compositions 97W-3% Ni_3Al or 97W-3% NiFeAl are shown in Figure 15a-b. These samples were sintered under the following conditions: 1550°C/0.5 hrs in atmosphere A. The sintered density was $\approx 97\%$ for alloys with Ni_3Al matrix and $\approx 100\%$ for those with NiFeAl matrix; the average W particle size was in the range 25-30 μm . The micrographs in Figure 15, however, exhibit large scale W-W particle contiguity which would be indicative of poor mechanical properties. This is presumably due to the low matrix weight fraction. Hence, heavy alloys with higher matrix weight fractions were investigated next.

Figures 16a-b show the low magnification micrographs of 95W + 5%matrix (Ni_3Al and Ni-12Al-40Fe) heavy alloys sintered at 1600°C for 30 minutes in atmosphere A and polished to a 1 μm finish. For these sintering conditions, the sintered densities obtained were 98% for Ni_3Al matrix and $\sim 100\%$ for Ni-12Al-40Fe (henceforth referred to as NiFeAl) matrix. The mean W particle size was $\approx 20\mu\text{m}$ and the matrix was well dispersed around the W grains. No porosity is evident from these micrographs although an unidentified phase of

darker contrast at the W-matrix interface in the micrographs of higher magnification, see Figure 16c-d. A preliminary elemental compositional analysis of the W particles, matrix and the dark particles was conducted for the alloys containing 5% Ni₃Al and 5% NiFeAl and the results are reported in Tables VI and VII respectively. Correlating the results of Table VI with Figure 16c and Table VII with Figure 16d, it is clear that the W grains are essentially pure while the dark particles appear to be Al-enriched. The Al concentration measured in these particles sometimes exceeded 75% which may be erroneous due to the absorption effects and large activation volume during compositional analysis using EDS in a SEM. It should be noted that for the alloy 95W-5Ni₃Al, some Fe was measured during the semi-quantitative chemical analysis (EDS); this iron was probably incorporated in the Ni₃Al (which has an extensive solubility for Fe) during the milling of as-received Ni₃Al powders in steel jars. X-ray diffraction patterns from these heavy alloys indicated a two-phase microstructure consisting of W and Ni₃Al (or NiFeAl) phases; no diffraction peaks corresponding to the dark particles can be seen in Figures 16e-f presumably due to their low volume concentration. W heavy alloys with 7% matrix were processed as follows: 93W-7% Ni₃Al alloys were sintered at 1575°C for 30 minutes while 93W-7%NiFeAl specimens were sintered at 1550°C for 20 minutes. The as-sintered specimens exhibited a density \approx 98% of theoretical and the average W particle size measured between 20-30 μ m for Ni₃Al-based alloys and between 10-20 μ m (closer to 20 μ m) for NiFeAl-based alloys. The microstructures were examined in a SEM and were qualitatively similar to those described earlier for 5% matrix alloys (see Figures 17a-b). As described in Figure 16, small dark particles were observed at the W-matrix interface in both alloys. These dark particles were of 1-2 μ m size in Ni₃Al-based alloys and \approx 5 μ m size in NiFeAl-based heavy alloys. Again, these particles were observed to be Al-enriched when examined by EDS in a SEM.

Table VI. Elemental Analysis of Sample 95W + 5% Ni₃Al. Area of analysis is indicated by markings on the SEM Picture of Figure 16c.

ELEMENT	ELEMENTAL COMPOSTION (wt%)								
	G	M1	M2	M3	P1	P2	GR1	GR2	GR3
W	89.67	22.82	14.26	18.30	19.63	-	100.00	100.00	95.93
Ni	10.33	71.84	74.18	76.96	28.15	38.03	-	-	4.07
Al	-		7.40	-	52.22	58.32	-	-	-
Fe		5.34	4.16	4.73	-	3.65	-	-	-

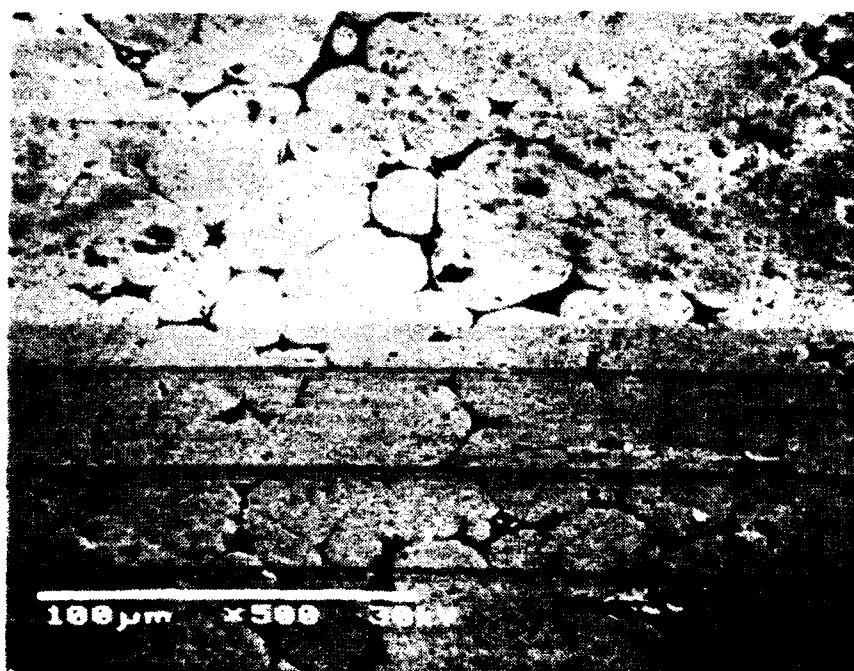
G = general area
M = matrix area
P = precipitated particles
GR - grain area

Table VII. Chemical analysis for 95W-5NiFeAl corresponding to Figure 16d.

ELEMENT	ELEMENTAL COMPOSTION (wt%)								
	G	M1	M2	M3	P1	P2	P3	GR1	GR2
W	87.02	52.00	9.51	33.06	-	-	-	100.00	100.00
Ni	7.73	28.86	51.68	39.58	16.09	19.73	-		
Al	-		-	-	71.23	64.57	100.00		
Fe	5.25	5.34	38.81	27.36	12.68	15.70	-		

G = general area
M = matrix area
P = precipitated particles
GR - grain area

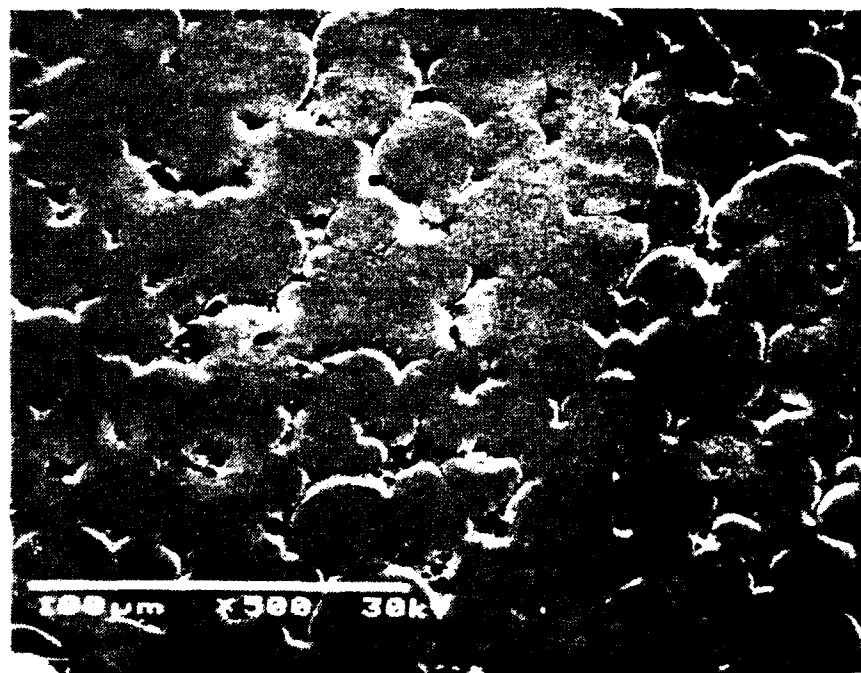
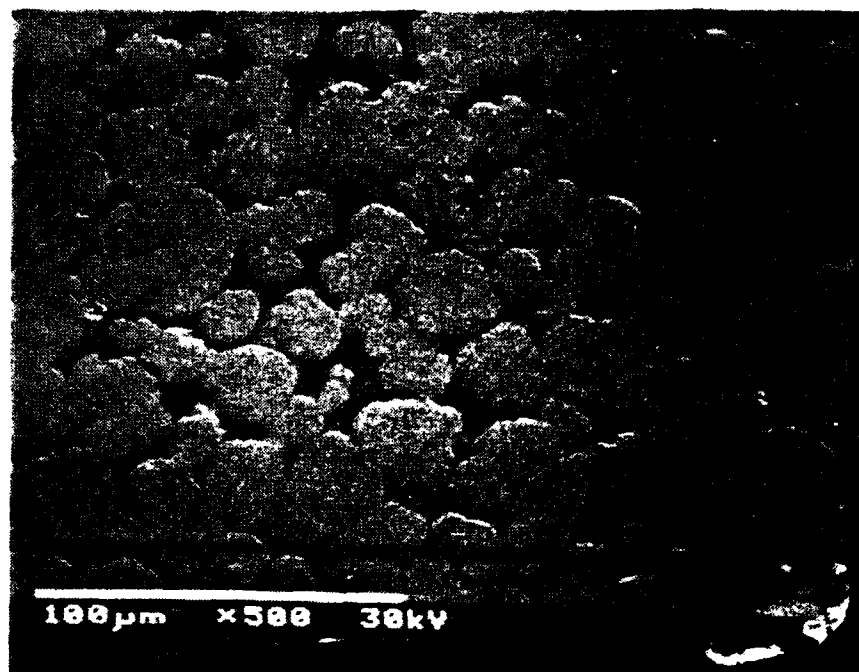
(a)



(b)

Figure 15. SEM micrographs of liquid-phase sintered (a) W+3%Ni₃Al & (b) W+3%NiFeAl.

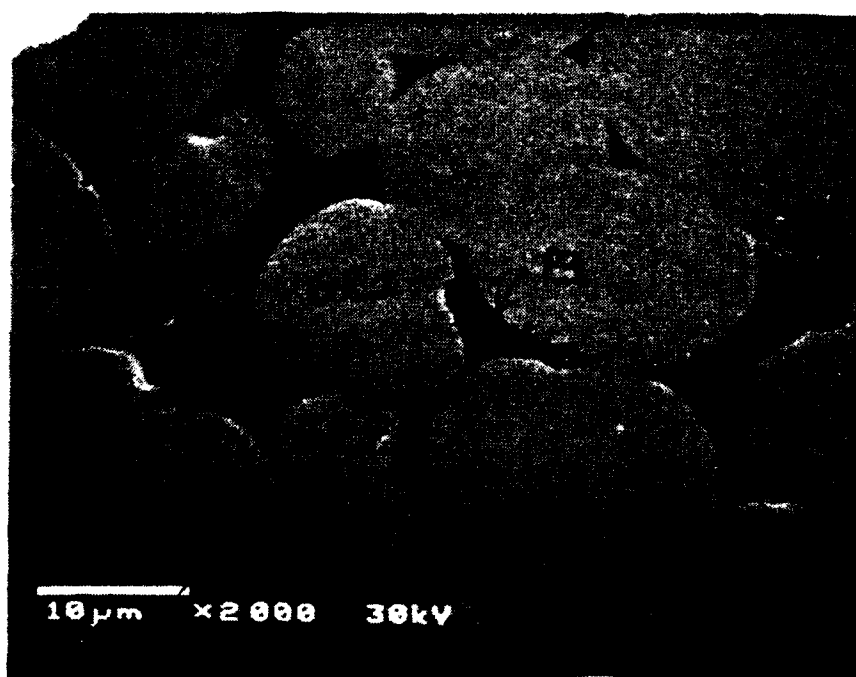
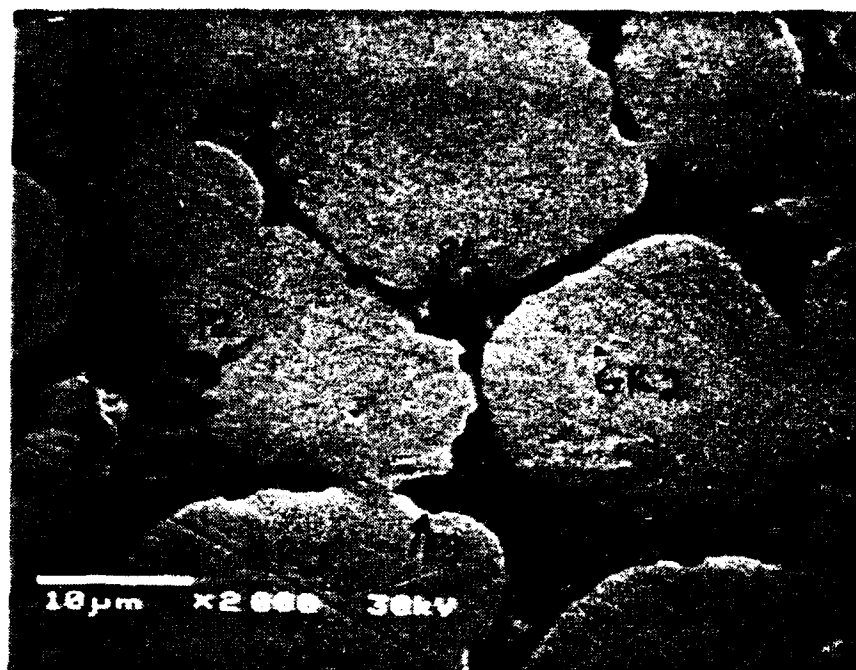
(a)



(b)

Figure 16a-b. Low magnification SEM micrographs for liquid-phase sintered (a) W+5%Ni₃Al, & (b) W+5%NiFeAl.

(c)



(d)

Figure 16c-d. High magnification SEM micrographs for liquid-phase sintered (c) W+5%Ni₃Al & (d) W+5%NiFeAl.

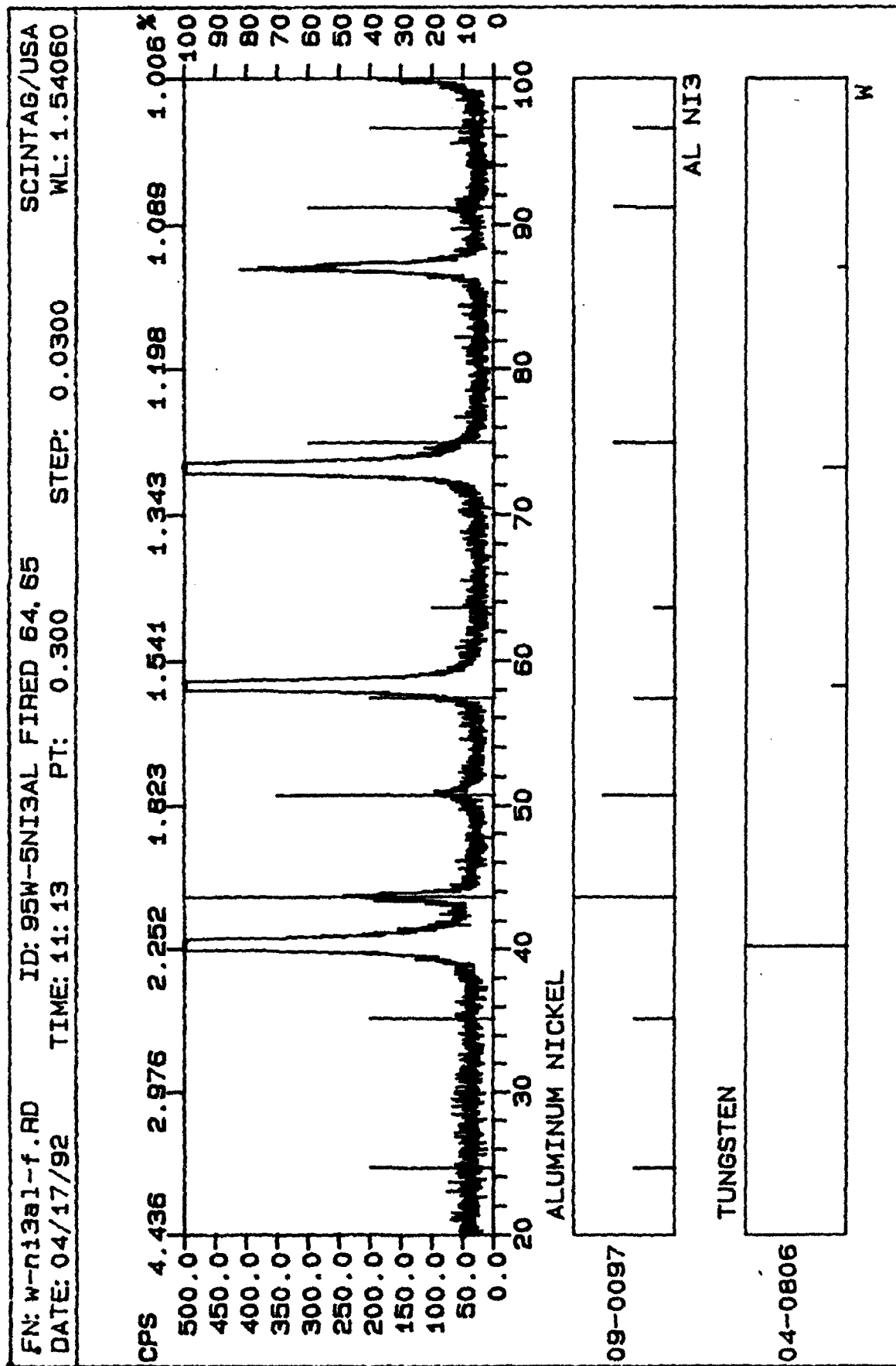


Figure 16e. X-ray diffraction pattern for sintered heavy alloy W + 5%Ni₃Al.

Dmp

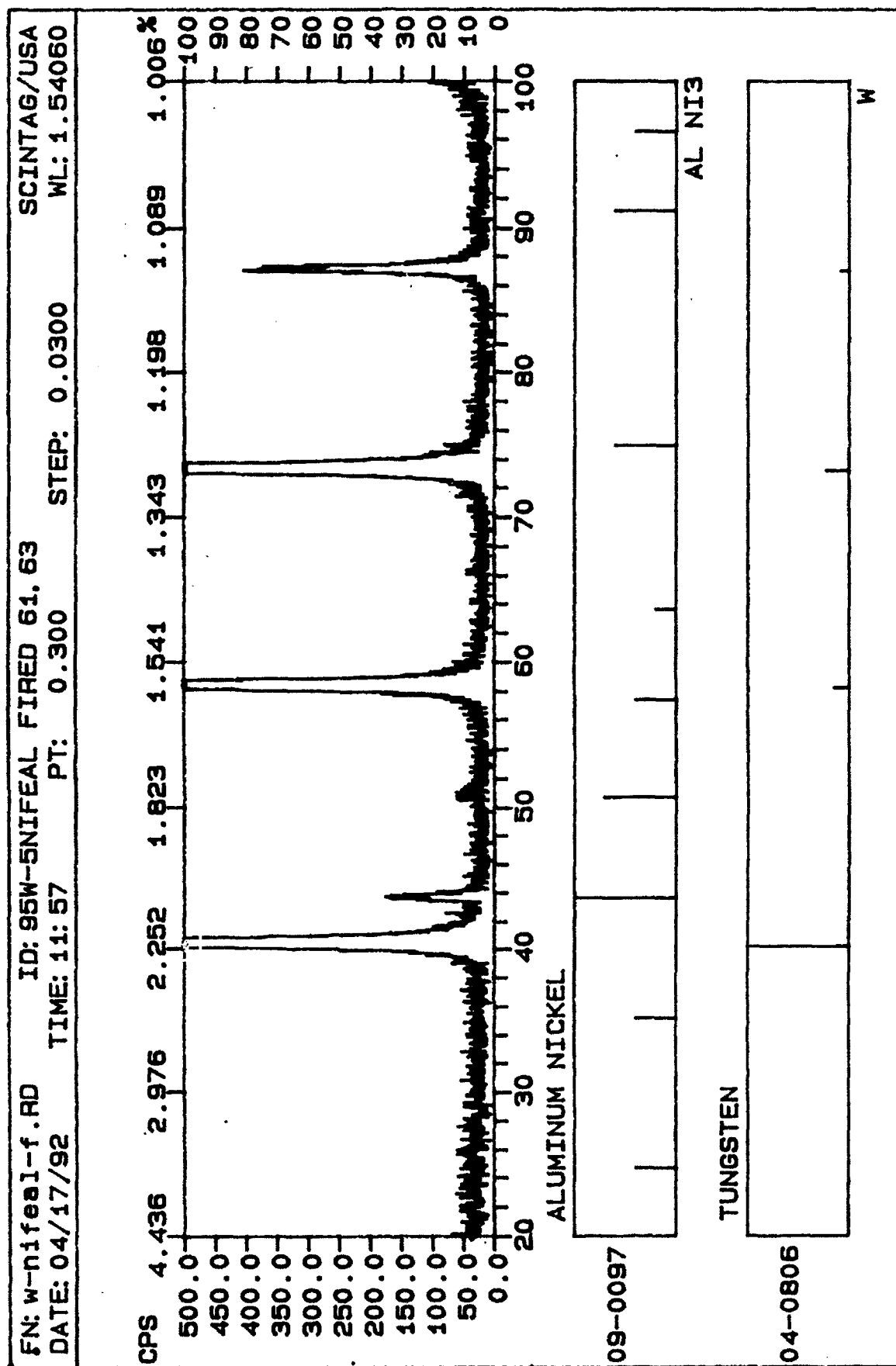
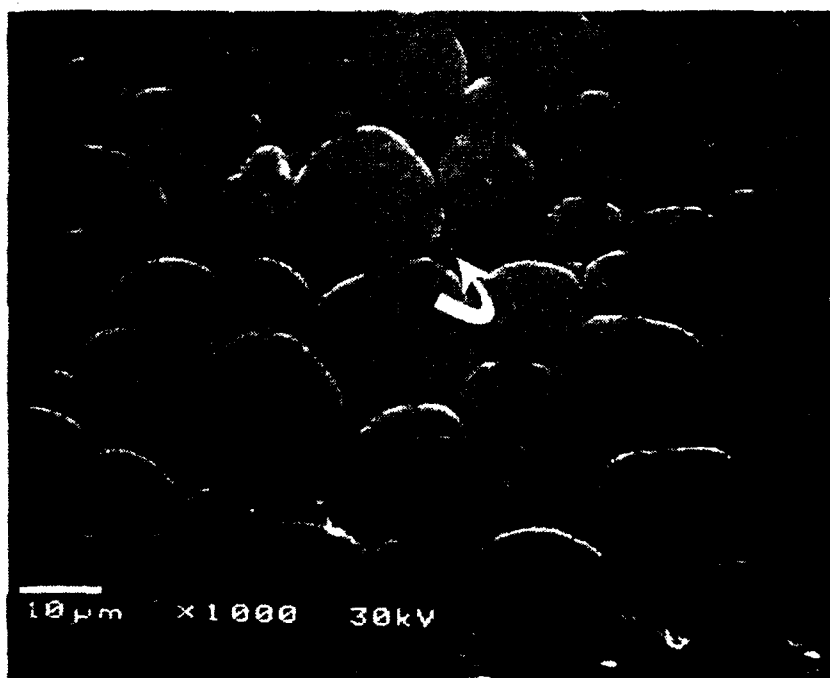
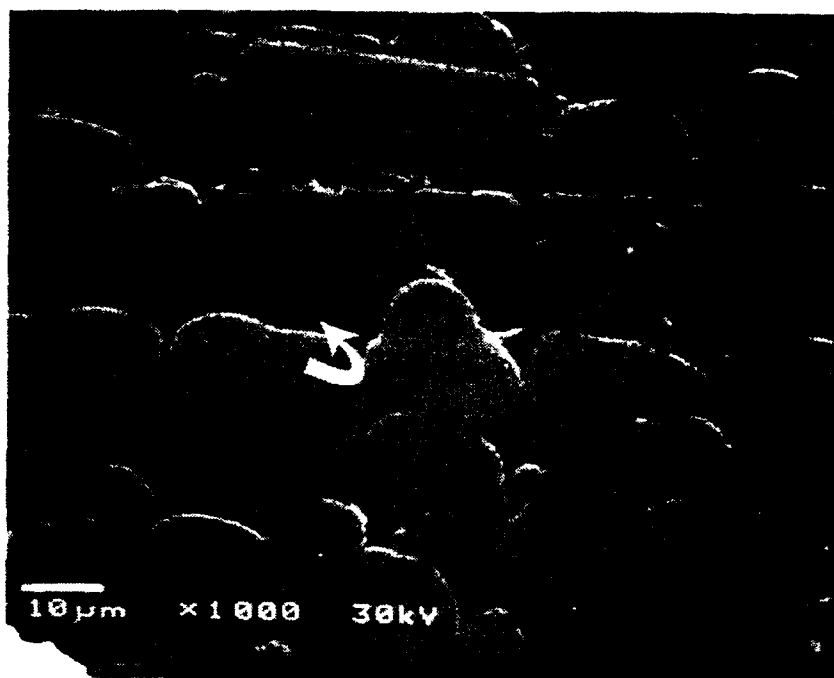


Figure 16f. X-ray diffraction pattern for sintered heavy alloy W + 5%NiFeAl.

(a)



(b)

Figure 17. High magnification SEM micrographs for liquid-phase sintered (a) W+7wt.%Ni₃Al, & (b) W+7wt.%NiFeAl.

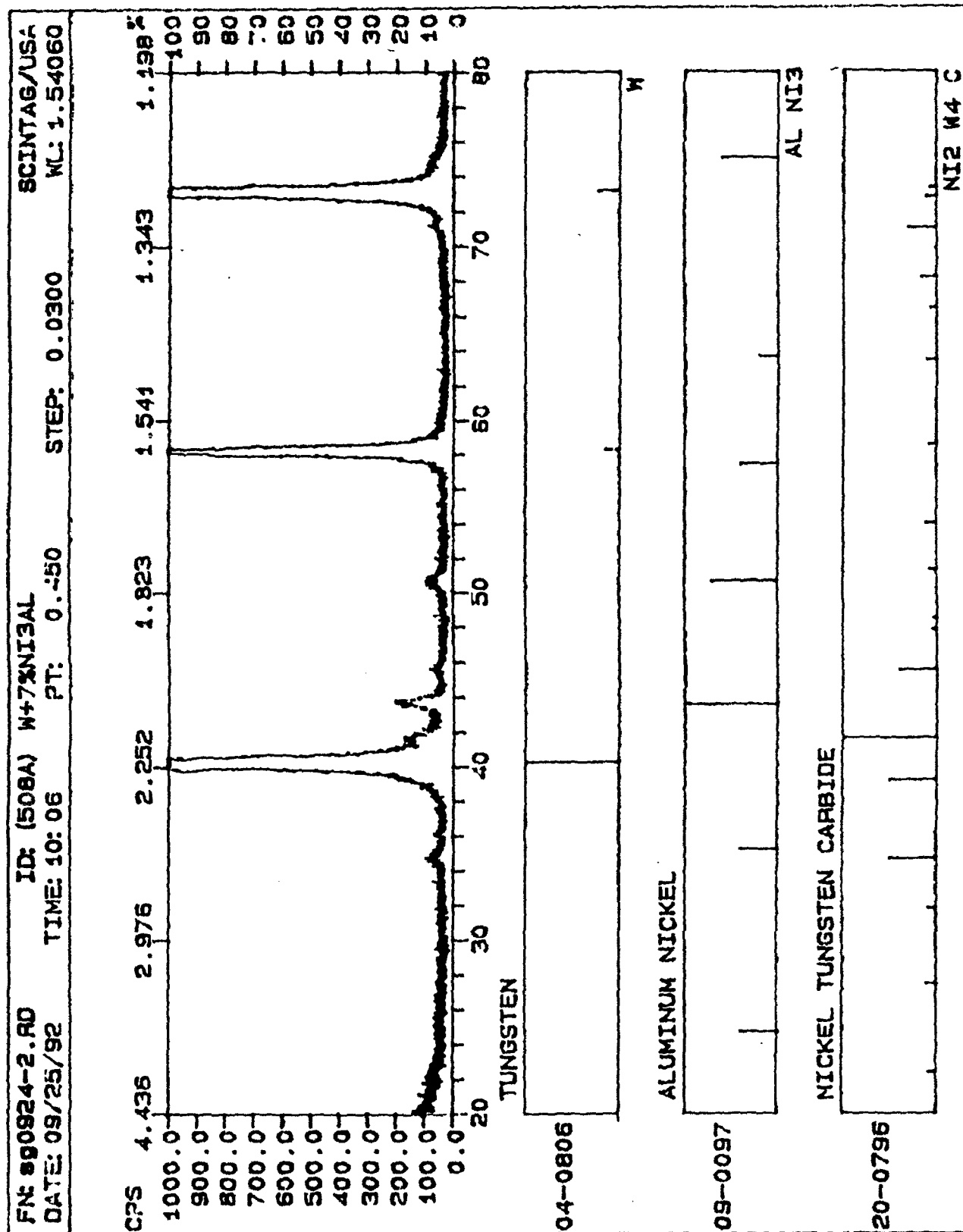


Figure 18. X-ray diffraction pattern for the sintered heavy alloy W+7%Ni₃Al.

While the carbide phase cannot account for the Al-enrichment normally associated with these particles, no Al-W or Al-Ni intermetallics could be satisfactorily fitted to account for these peaks. Further, since an EDS system can not X-ray diffraction pattern from a W + 7%Ni₃Al specimen (see Figure 18), however, indicated the presence of W and Ni₃Al as primary phases; three extra weak peaks at $\approx 35^\circ$, $\approx 42^\circ$ and $\approx 46^\circ$ match with the diffraction pattern for the phase Ni₂W₄C. detect carbon, hence EDS compositional measurements could not be used to argue against the presence of such carbide phases. Thus, it is tentatively concluded that both Ni₂W₄C and some presently unidentified phase is present. Microprobe measurements (described later) are necessary for more precise compositional estimates of these different phases in the microstructure.

The microstructures of heavy alloys with 10wt.% matrix are shown in Figure 19. Two sets of sintering conditions were investigated for each alloy. The alloy 90W-10%Ni₃Al was sintered at 1550°C/15 mins and 1575°C/30mins while the alloy 90W-10%NiFeAl was sintered at 1475°C/15mins and 1485°C/20mins. The SEM micrographs corresponding to the first set of sintering conditions are shown in Figures 19a-d. Figure 19a is a low magnification micrograph showing $\approx 15\text{-}30\mu\text{m}$ W particle sizes although in addition to W and the matrix, there appears to be a third phase (which exhibits sharp facets). By contrast, the microstructure of the 90W-10NiFeAl alloy is similar to other WHA consisting of $\approx 10\mu\text{m}$ sized W particles in an intermetallic matrix, see Figure 19b. Figures 19c and 19d are high magnification micrographs corresponding to the W + 10%Ni₃Al and W + 10%NiFeAl alloys. Compositional measurements in a SEM (using EDS) corresponding to different features indicated on these micrographs are listed in Tables VIII and IX respectively. Based on the compositional measurements in Table VIII, it is clear that the faceted phase in Figure 19c is a W-Ni phase. Sintering at slightly higher temperatures (1575°C/30mins) resulted in a

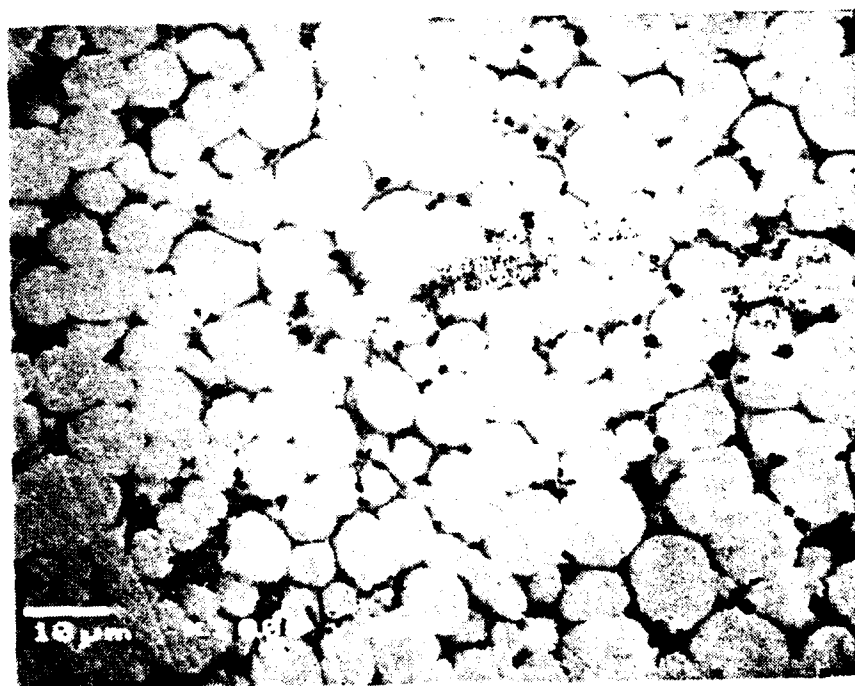
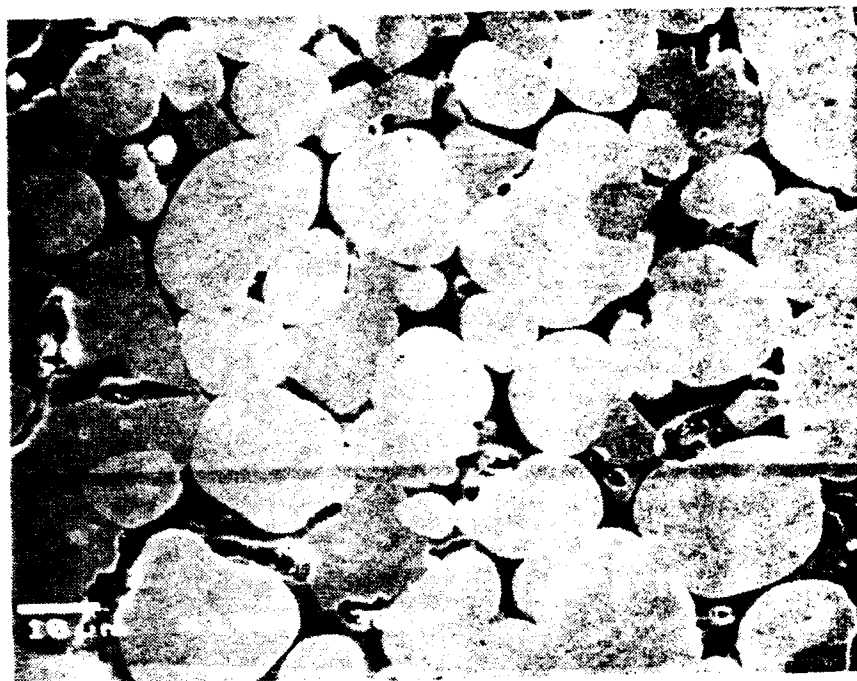
Table VIII. EDS elemental analysis of alloy composition W+10%Ni₃Al corresponding to Figure 19C.

ELEMENT (wt%)	GENERAL AREA	MATRIX	MATRIX PARTICLES	GRAINS (G)	SGI1	SG2
Al K α	3.91	trace	38.50	0		
Ni K α	32.11	89.67	61.50	0	33.82	36.22
W M α	63.98	10.33	0	100.00	66.18	63.78

Table IX. EDS elemental analysis of alloy composition 95W+10%NiFeAl corresponding to Figure 19d.

ELEMENT (wt%)	GENERAL AREA	MATRIX	MATRIX PARTICLE	GRAIN
Al K α	3.34	trace	56.85	0
Fe K α	9.16	34.19	15.37	0
Ni K α	14.53	54.02	27.78	0
W M α	72.97	11.79	0	100.00

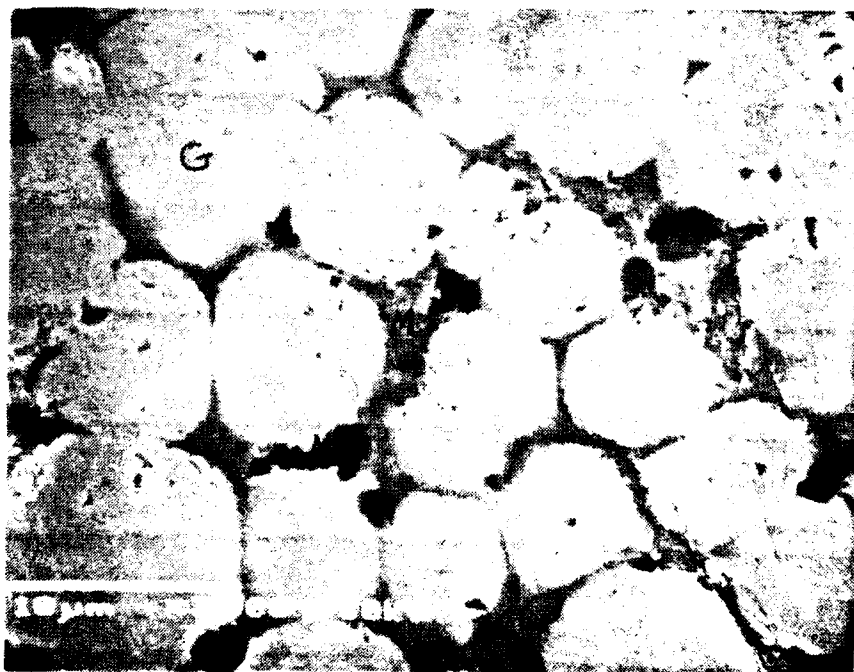
(a)



(b)

Figure 19a-b. Low magnification SEM micrographs for liquid-phase sintered (15 minutes at 1475 or 1550°C) (a) W+10%Ni₃Al & (b) W+10%NiFeAl.

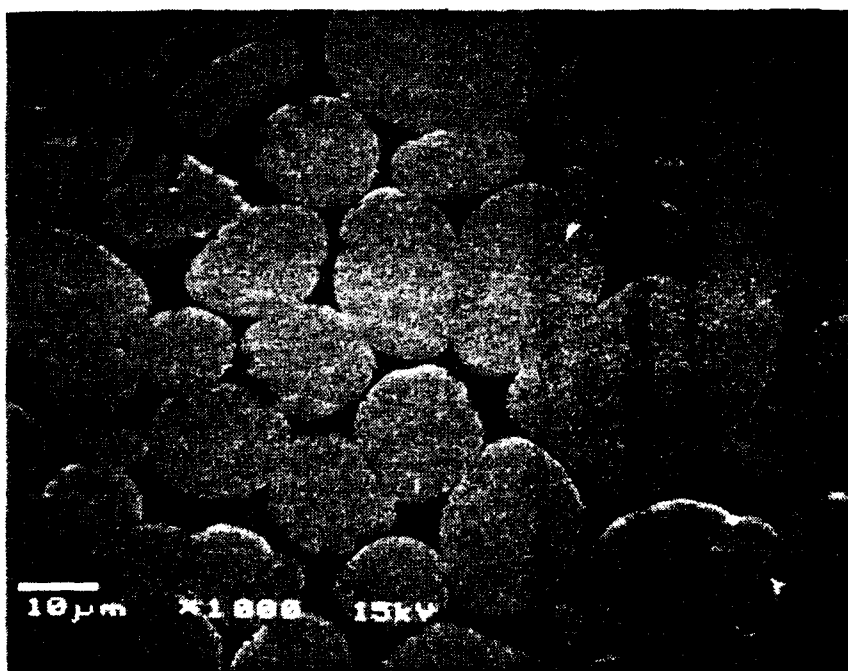
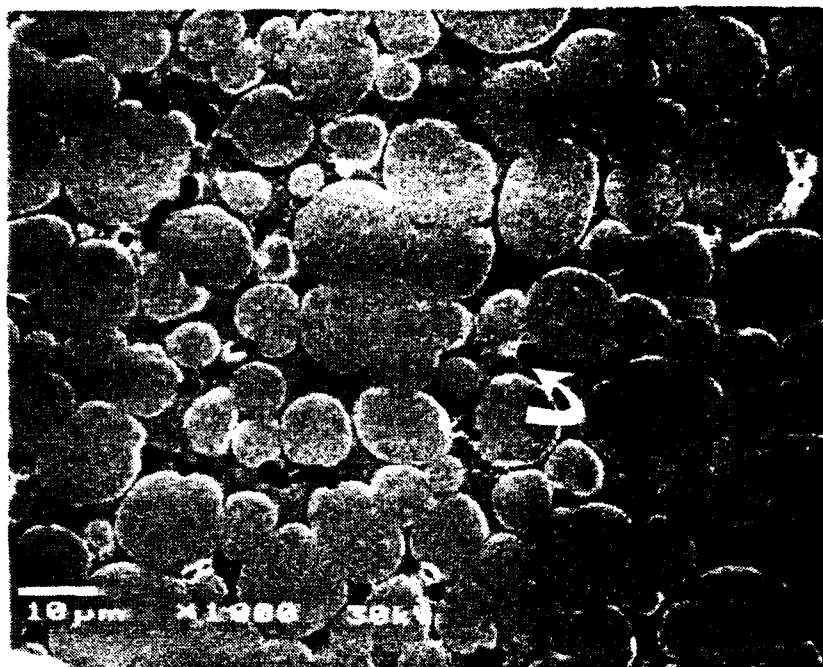
(c)



(d)

Figure 19c-d. High magnification SEM micrographs for liquid-phase sintered (c) W+10%Ni₃Al, & (d) W+10%NiFeAl.

(e)



(f)

Figure 19e-f: High magnification SEM micrographs for (e) W+10%Ni₃Al and (f) W+10%NiFeAl sintered at 1475-1575°C/20-30mins.

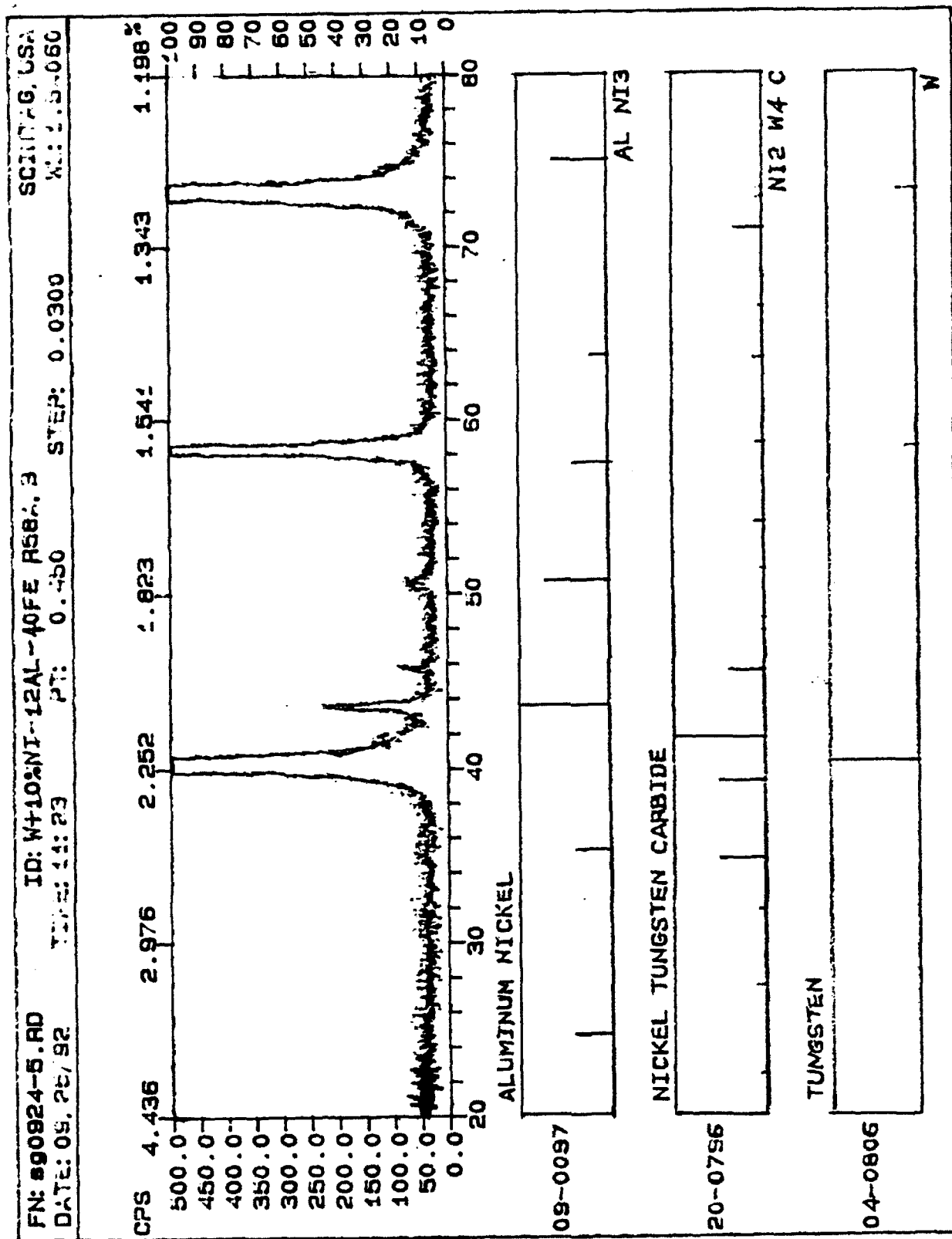


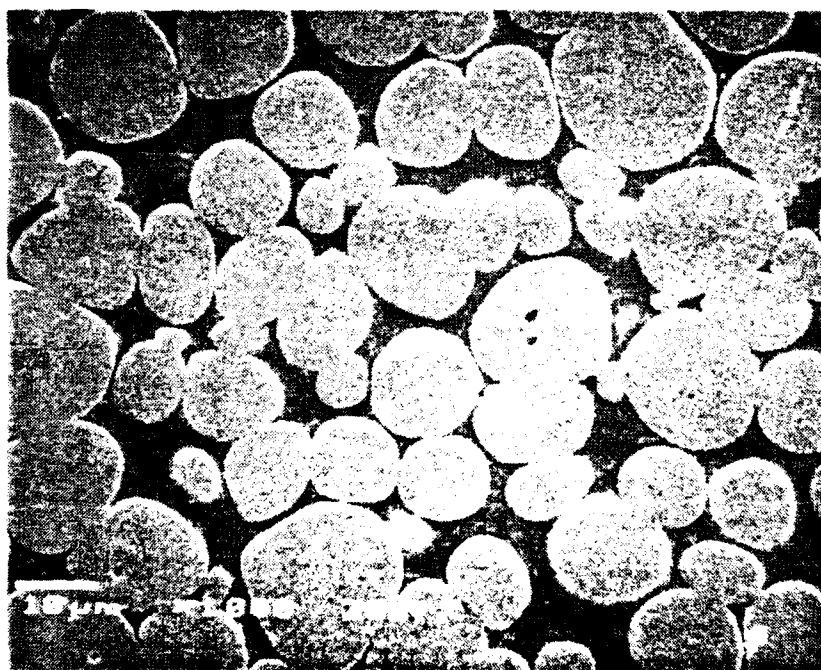
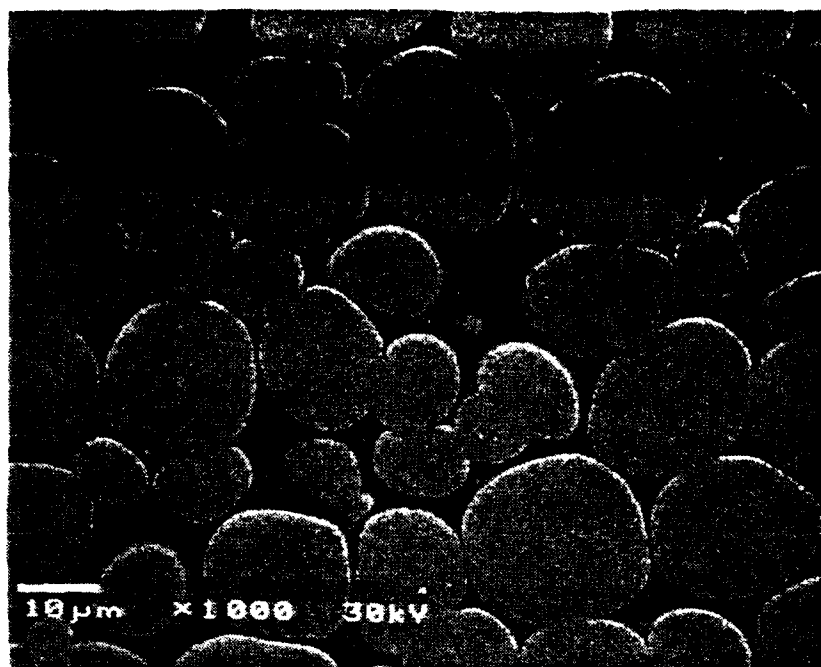
Figure 20. X-ray diffraction pattern corresponding to specimen in Figure 19f (W + 10%NiFeAl) showing the presence of W, NiFeAl (pattern being similar to Ni_3Al) and $\text{Ni}_2\text{W}_4\text{C}$ phases.

microstructure essentially free from these faceted phases, see Figure 19e. The intermetallic matrix for this alloy was identified to be Ni_3Al using x-ray diffraction, see Figure 20. For the alloy $\bar{\text{W}} + 10\%\text{NiFeAl}$ sintered at 1485°C for 20 mins (Figure 19f), the microstructure is essentially similar to that described earlier in Figure 19d, where $\approx 5\mu\text{m}$ diameter particles (presumably $\text{Ni}_2\text{W}_4\text{C}$) were observed at the W-matrix interfaces. Note however that compositional measurements using EDS again suggest these dark particles to be Al-enriched although no Al-Ni or Al-W intermetallics could be satisfactorily matched to the weak peaks unaccounted in the x-ray diffraction pattern in Figure 20.

Finally, specimens of $\text{W} + 7\%\text{Ni-Fe}$ and $\text{W} + 10\%\text{Ni-Fe}$ (a 8:2 Ni-to-Fe ratio) specimens were sintered at 1450°C for 20 minutes, the SEM micrographs corresponding to their microstructure are shown in Figure 21. The W particle sizes are in the range $10\text{-}20\mu\text{m}$ for both alloy compositions although the particle sizes are smaller (closer to $10\mu\text{m}$) for the alloy with higher matrix weight fraction. Note that no dark particles are observed in the matrix which would suggest that these dark particles are probably related to the presence of Al in the alloy. Further, the sintered densities were higher with a Ni-Fe matrix in comparison to those with an intermetallic matrix which would be indicative of the possible role of Al contributing towards lower densities (quite likely the precipitation of Al-rich particles would lower the theoretical density which would then imply that the sintered densities were really much better than those reported above).

The question thus remains, "Is there $\text{Ni}_2\text{W}_4\text{C}$ in the microstructure?". Since the detection of C would be impossible using a conventional EDS system, measurements were carried out using an electron microprobe analyzer at the University of Arizona, Dept. of Geosciences. The analysis indeed detected the presence of C in some of these particles which indicates that $\text{Ni}_2\text{W}_4\text{C}$ is a likely phase in the microstructure. It should be noted, however, that some particles were also detected to be highly Al-enriched which would

(d)



(b)

Figure 21. SEM micrographs for conventional WHA (8:2 Ni-Fe ratio) with (a) 7% and (b) 10% matrix.

indicate that probably a small volume fraction of a second Al-based phase may also be present. Detailed TEM analysis is necessary to unambiguously establish the microstructure of these liquid phase sintered intermetallic-based heavy alloys.

E. Quasi-Static Testing

Preliminary evaluation of mechanical properties of this novel class of intermetallic-based tungsten heavy alloys was performed using 4-pt bend testing with an outer span of 18mm and an inner span of 9mm. Bend testing was also utilized to examine the influence of heat treatments, if any, on the mechanical properties. A summary of bend test results is shown in Table X. From the Table X, it is clear that a heat treatment consisting of annealing at 1100°C for 1 hour in Argon followed by quenching did not significantly affect the properties of the heavy alloys. By contrast, the compositions of the heavy alloys themselves exerted more influence on the quasistatic mechanical properties. Generally, the heavy alloys based on Ni-12Al-40Fe matrix were stronger than those based on Ni₃Al matrices. However, it is not clear whether the higher strength measured in bend testing can be related to increased strength or increased ductility since both these parameters can affect the final fracture strength. Furthermore, plastic deflections in the bend specimens can artificially inflate the bend test values. This is illustrated by the results of specimens R57T where bend strengths over 4GPa were observed for specimens that did not fail by plastic deformation. Similar results were observed for conventional WHA where the specimens underwent extensive plastic deformation without failure and the calculated bend strength values were as high as several GPa.

In addition to the bend tests, tensile tests were carried out to examine the influence of heavy alloy composition on mechanical properties such as yield strength, tensile strength and ductility. The alloys containing the L1₂ matrix (Ni₃Al or Ni-12Al-40Fe (at.%)) exhibit

Table X: Bend Tensile Results of Pressureless Sintered Tungsten Heavy Alloys

SAMPLE ID	COMPOSITION	TREATMENT	FLEXURAL STRENGTH (MPa)
307	W + 5% Ni ₃ Al	none	701 (± 49)
475	W + 7% Ni ₃ Al	none	1,113
475	W + 7% Ni ₃ Al	HT&Q	1,196
314	W + 5% NiFeAl	none	901 (± 22)
314	W + 5% NiFeAl	HT&Q	910
R56T	W + 10% NiFeAl	none	1,270 (± 123)
R58	W + 10% NiFeAl	none	1,482 (± 67)
R57T	W + 7% NiFeAl	none	1,476 4,705 ** 4,410 **
488	W + 7% NiFeAl	none	1,462 (± 135)

* HT&Q = Heat treated in Argon at 1100°C for one hour, quenched to room temperature in a bath of water (ΔT - 1070°C).

** = Samples showed large amounts of deflection and failure did not occur.

Table XI: Summary of Tensile Test Results of W-Heavy Alloys

Sample Composition	Density (g/cc) (% theoretical)	UTS (MPa)	Yield Strength (MPa)	Elongation (%)	Hardness (Rc)
W + 5% Ni ₃ Al	17.394 (96.7) 17.308 (97.2)	544.6 551.7	- -	0 0	36.3
W + 7% Ni ₃ Al	16.955 (97.5)	724.2	649.4	1.3	35.4
W + 10% Ni ₃ Al	16.452 (98.7) 16.434 (98.5)	739.6 718.3	685.3 656.4	1.2 1.1	36.9
W + 5% NiFeAl	17.455 (97.6) 17.593 (98.3)	406.0 517.0	- -	0 0	34.5
W + 7% NiFeAl	17.007 (97.8) 17.135 (98.5)	762.2 757.6	590.5 594.6	5.3 3.9	33.5
W + 10% NiFeAl	16.345 (98.0) 16.319 (97.9)	736.8 673.8	580.6 550.9	2.2 2.4	33.1
W + 7% (8Ni + 2Fe)	17.544 (98.7) 17.666 (99.4)	908.3 839.5	566.9 609.4	15.5 8.3	33.6
W + 10% (8Ni + 2Fe)	17.095 (99.4) 16.986 (98.8)	932.5 931.8	619.5 612.9	16.6 18.6	33.5

an increase in UTS as the matrix fraction increased from 5 wt% to 7wt%. An increase in matrix fraction from 7wt% to 10wt%, however, shows little improvement in UTS or ductility for Ni₃Al-based heavy alloys. Also, for similar weight fractions of matrix, the heavy alloys with Ni-12Al-40Fe matrix exhibited lower yield strength but similar (or possibly slightly higher) UTS than those with Ni₃Al matrix. This is evident in UTS, YS and elongation data in Table XI. The conventional heavy alloys containing 7% and 10% matrix of (8Ni + 2Fe) were tested primarily for comparison purposes. These samples showed much higher UTS and elongation but slightly lower yield strengths. It is worthwhile noting that the alloys containing NiFeAl matrix exhibited higher tensile elongation than those containing Ni₃Al matrix. Overall the alloy composition W + 7% NiFeAl showed the best mechanical behavior among the L1₂-based heavy alloys.

The 4-pt bend strength values listed in Table X indicate considerably higher strengths than those observed in tensile tests. This is attributable to the deflection in the specimen that occurs during bend testing. For example, for W + 7wt%NiFeAl (alloy R57T), the bend strengths computed for specimens that exhibited considerable deflection (to the point that they did not fail) were in excess of 4 GPa, yet their tensile strengths were considerably lower. Three-point bend test results have been used in the past as a measure of higher ductility in tungsten heavy alloy specimens synthesized from coated powders by comparing the bend strengths with previously reported tensile strengths. Referring back again to alloy W + 7% NiFeAl, it is clear that even though the bend specimen did not fail (which indicates considerable ductility), the tensile ductility was only $\approx 5\%$. Hence, the conclusion of our experimental work is that considerable caution should be exercised when comparing the properties of tungsten heavy alloys measured by tensile and bend test techniques.

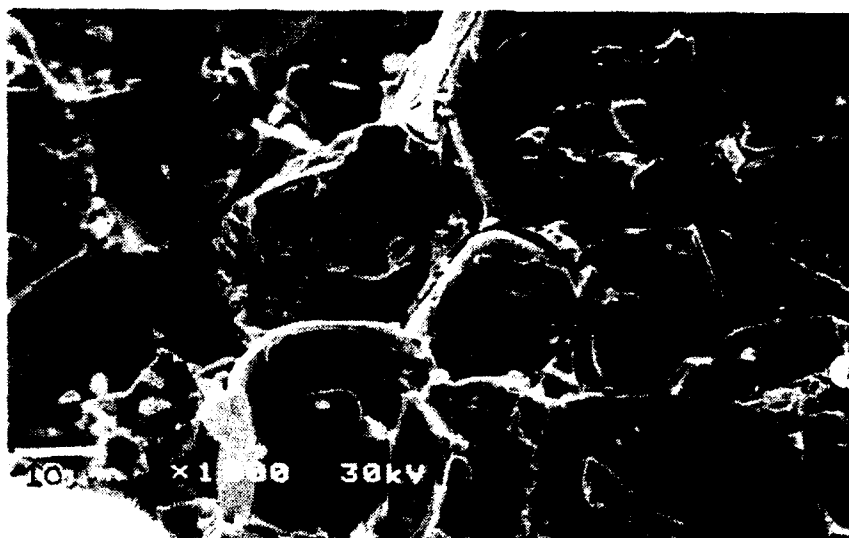
In addition to tensile tests, the hardness of these alloys was measured using a Rockwell C hardness tester. The alloys showed no significant variation due to the matrix

type or matrix content for the compositions tested. The results of hardness tests are shown in Table XI. Also, after tensile testing, polished longitudinal sections near the fracture surfaces and the fracture surfaces of these samples were examined in the SEM to look for evidence of plastic tearing in the intermetallic matrix. Fractographs and SEM micrographs of polished longitudinal sections of these samples are shown in Figures 22-25.

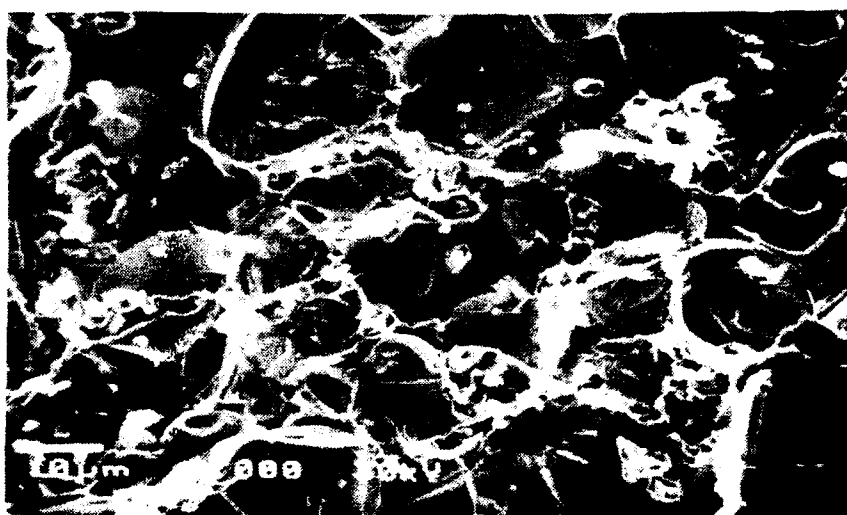
Comparing the fracture surfaces of heavy alloys based on Ni_3Al matrix (Figure 22a-c), it is clear that for alloys containing only 5% matrix, failure occurs by separation between and by cleavage cracks in the W grains. By contrast, the alloys with 7 and 10wt% matrix exhibit evidence of plastic tearing in the matrix which is indicative of the intrinsic ductility of the intermetallic matrix. A large number of $1\text{-}2\mu\text{m}$ diameter particles (presumably Ni-W-carbides) are also observed on the fracture surfaces which are believed to be the dark particles observed during microstructural analysis of these heavy alloys (see Figures 16). In comparison with the Ni_3Al -based heavy alloys, those based on the intermetallic Ni-12Al-40Fe exhibit evidence of considerably more ductility (Figure 23) as seen by the size of the dimples encircling the W grains (these are comparable to the dimples in the heavy alloys sintered with Ni-Fe matrix as shown in Figure 24). Also, the frequency of the unknown phase ($\approx 5\mu\text{m}$ dia. particles in this case, presumably $\text{Ni}_2\text{W}_4\text{C}$) is lesser in these alloys in comparison with the Ni_3Al -based alloys; these particles are absent in the W alloys sintered with Ni-Fe matrix. This is indicative of the fact that the frequency of these particles may be related to the Aluminum content in the matrix; the higher the Al content, the higher the expected frequency of these unidentified particles.

In addition to examination of fracture surfaces, polished longitudinal sections near the fracture surfaces were also examined and the SEM micrographs are shown in Figure 25a-c. From these figures, it is clear that crack nucleation in the WHA with Ni-Fe matrix occurs by separation at the W grain-(Ni-Fe) matrix interface. The incidence of interfacial

(a)



(b)



(c)

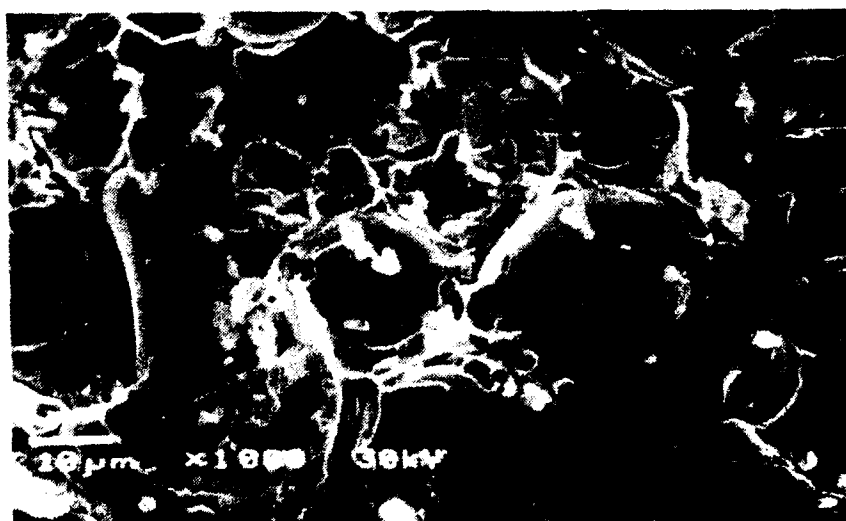
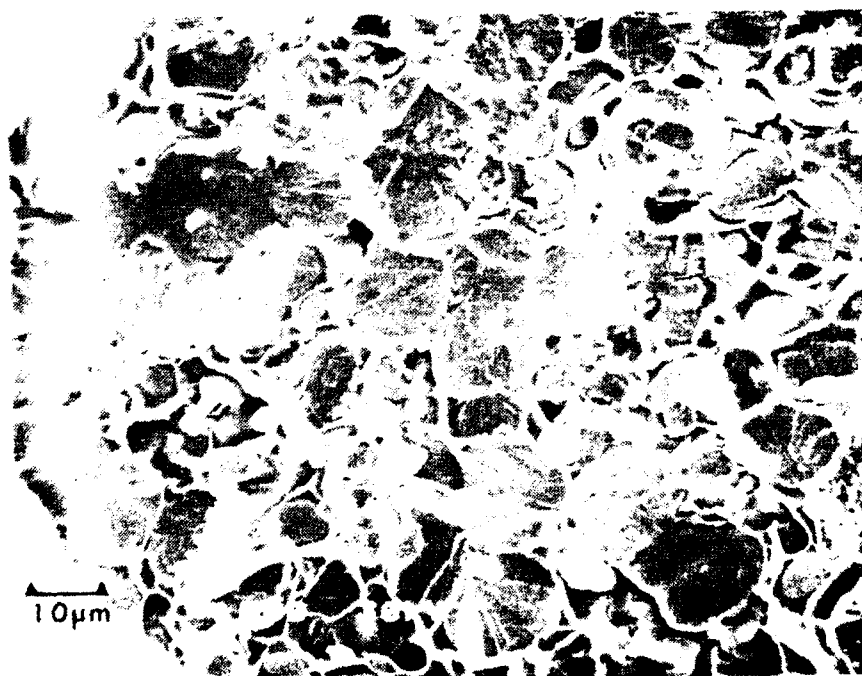
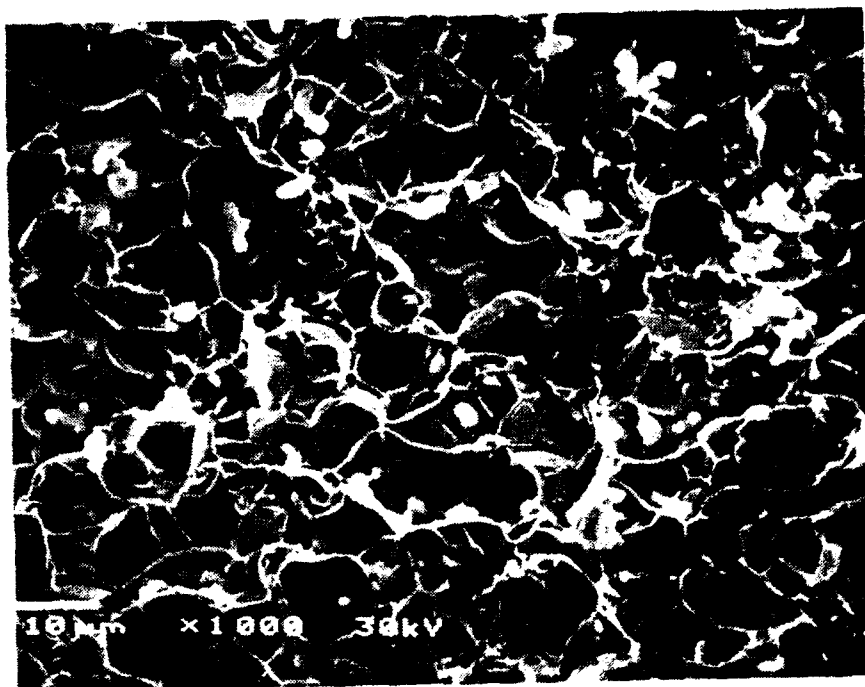


Figure 22. Fractographs of tensile-tested W+Ni₃Al heavy alloys with (a) 5% matrix (b) 7% matrix and (c) 10% matrix.

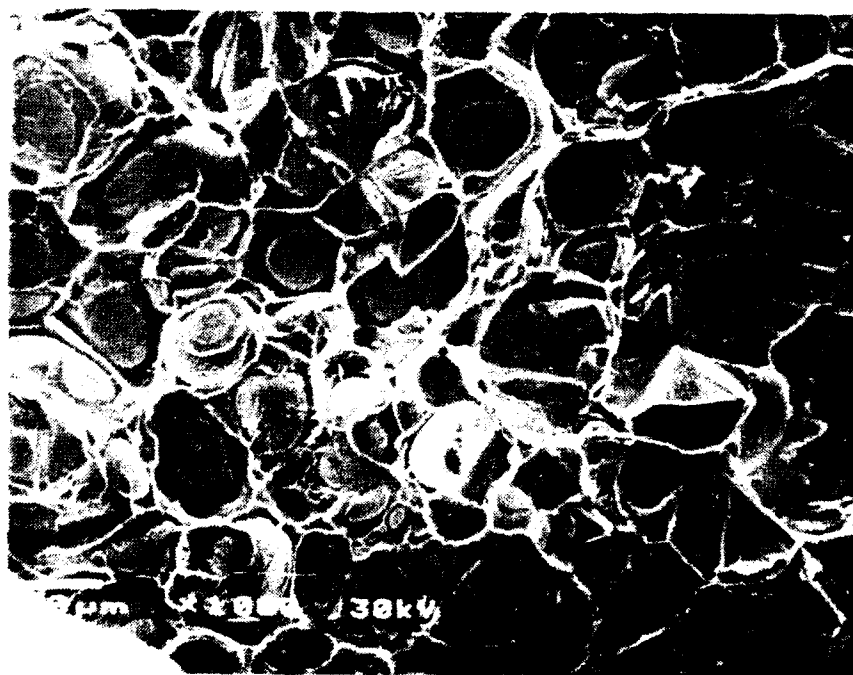
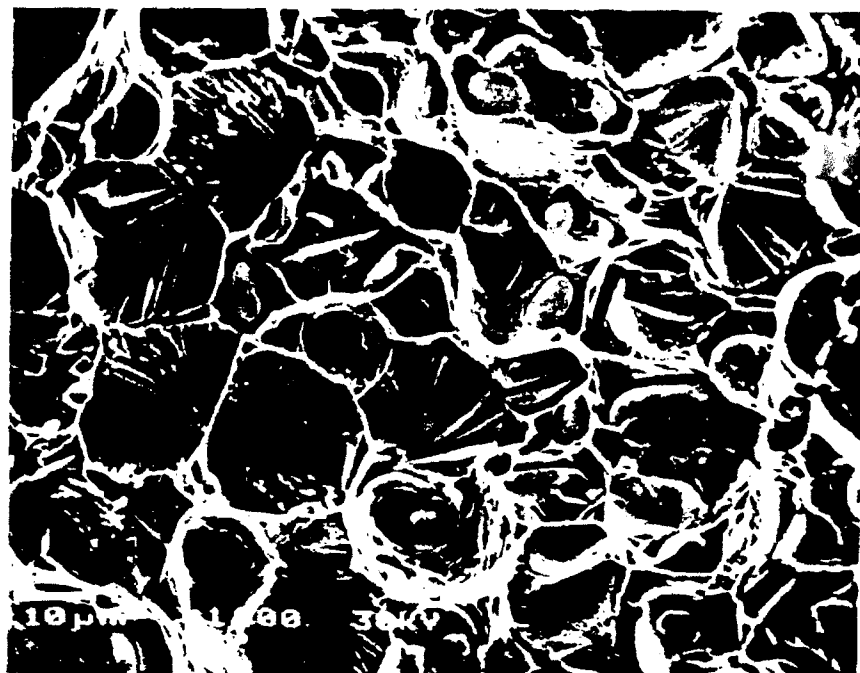
(a)



(b)

Figure 23. Fractographs of tensile-tested W+NiFeAl heavy alloys with (a) 7% matrix and (b) 10% matrix.

(a)



(b)

Figure 24. Fractographs of conventional WHA (W+NiFe) with (a) 7% matrix and (b) 10% matrix.

(a)



(b)



(c)

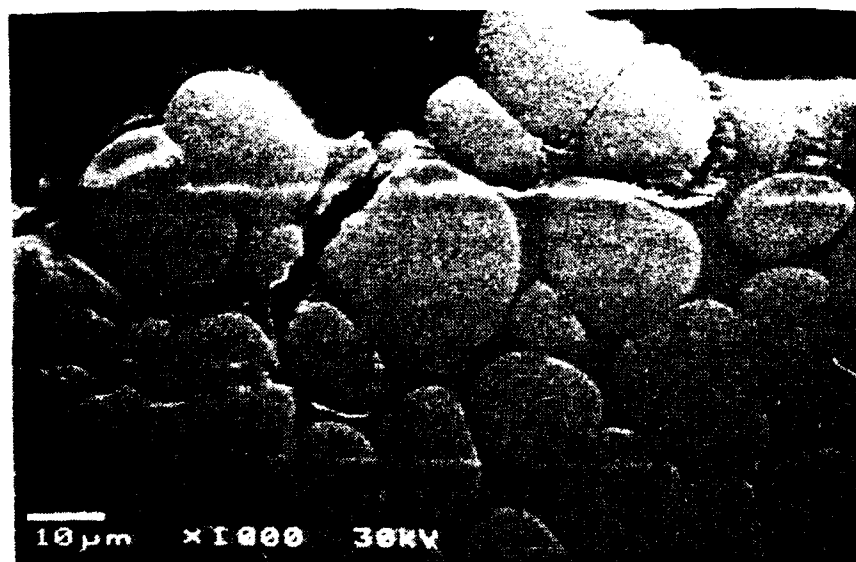


Figure 25. SEM micrographs of polished longitudinal sections (near fracture surface) of (a) W+7%Ni₃Al, (b) W+7%Ni₁₂Al-40Fe & (c) W+7%NiFe.

separation, however, decreases with increasing Al content such that for the WHA with Ni_3Al matrix, no separation is observed between the W grains and the intermetallic matrix. Rather, the fracture path clearly occurs through W grains which is consistent with a 'cleavage fracture' failure mode observed in the fracture surfaces.

Although Ni_3Al has been shown to exhibit extensive tensile ductility, the ductility is dependent upon a critical control of stoichiometry; only Ni-rich Ni_3Al doped with boron in the range of 0.1-0.3at.% is known to exhibit good ductility. Clearly, since processing by the liquid phase sintering approach yields a Ni_3Al matrix with a significant quantity of dissolved tungsten in the intermetallic (as observed by EDS), the precise control of stoichiometry is disturbed, which may explain the degradation in ductility of the heavy alloy. In addition, the second phase particles may have had a detrimental effect in the ductility of the heavy alloy composite. Novel processing schemes have to be designed to minimize the dissolution of tungsten into Ni_3Al and possibly eliminate these second phase particles to improve the ductility. Alternately, the ductility (and other properties such as strength) may also be dependent upon the composition. For example, heavy alloys sintered with Ni-12Al-40Fe which is actually a two-phase intermetallic consisting of $\text{L1}_2 (\text{Ni,Fe})_3(\text{Al,Fe})$ dispersoids in a Ni-Fe matrix, exhibit higher ductility than those sintered with $\text{L1}_2 \text{Ni}_3\text{Al}$. It is quite likely that compositional optimization in the Ni-Fe-Al system or other L1_2 -based ternary intermetallic systems may yield even higher ductility for the composite at room temperature. And finally, for alloys sintered with NiFeAl matrix, those with 10% matrix phase exhibit lower ductility than those with 7% matrix. This result is contrary to expectation and may be related to defects during sintering as is evident in the microstructure for W + 10%NiFeAl

alloy in Figure 19f. Clearly, an improvement in the sintered densities may lead to further improvements in the ductility of the composite.

F. Dynamic Testing

Since these WHA are being developed as alternatives to DU as kinetic energy penetrators, it is imperative to examine the high strain rate properties (flow stress, ductility, shear localization) of these alloys. The alloys were investigated only in an as-sintered state. Typically, the as-sintered cylinders were 0.21" dia. x ≈ 0.4 " long, which were then centerless

Table XII: List of Specimens Shipped to Los Alamos National Labs for Hopkinson Bar Testing

Sample ID	Composition (wt. %)	Diameter (in)	Height (in)	Mass (gms)
7M1	W + 7% NiFeAl	0.1840	0.3275	2.5092
7M2	W + 7% NiFeAl	0.1840	0.2585	1.9750
7M3	W + 7% NiFeAl	0.1840	0.2590	1.9837
7M4	W + 7% NiFeAl	0.1840	0.2585	1.9807
10M1	W + 10% NiFeAl	0.1840	0.2580	1.8868
10M2	W + 10% NiFeAl	0.1840	0.2570	1.8825
MM1	NiFeAl Matrix	0.1840	0.2575	0.8729
MM2	NiFeAl Matrix	0.1840	0.2565	0.8706
MM3	NiFeAl Matrix	0.1840	0.2320	0.7920
7N1	W + 7% Ni ₃ Al	0.1840	0.2580	1.9178
7N2	W + 7% Ni ₃ Al	0.1840	0.2500	1.8932
7N3	W + 7% Ni ₃ Al	0.1840	0.2450	1.8508
7N4	W + 7% Ni ₃ Al	0.1840	0.2480	1.8330
10N1	W + 10% Ni ₃ Al	0.1840	0.2580	1.8685

ground to a diameter of 0.1840". Specimen height varied slightly with most specimens at 0.2575" height. Table XII is a list of specimen identification no., composition and dimensions of specimens tested in this program. These specimens were tested at the Dynamic Test facility at Los Alamos National Laboratory, courtesy of Dr. G.T. Gray. The specimens were tested with an $L/D \approx 1.4$. Ideally, the L/D ratio should be equal to $\tan(45 + \phi/2)$ where ϕ is the angle of deformation of the metal. Only in the case that $\phi = 0$ will a specimen of $L/D = 1$ set up conditions favorable for shear. For non-zero ϕ (which can be obtained from Mohr circle construction), a $L/D \leq 1$ is quite likely to prevent shear in the specimen. By contrast, for large L/D ratios, specimen buckling is of concern. Further, the value of ϕ at high strain rates is unknown. Hence, as a compromise between testing convenience and conventional wisdom for compression specimen geometry, a ratio of ≈ 1.5 was settled upon in consultation with Dr. Gray of Los Alamos National Laboratory. The results of high strain rate tests (strain rate of $5 \times 10^3/\text{sec}$) are shown in Figures 26 and 27.

The results shown in Figure 26 indicate that for the test conditions (projectile sintered at a gas pressure of 20psi, 3" striker bar), the intermetallic Ni-12Al-40Fe work-hardens almost linearly up to $\approx 1400\text{MPa}$ at $\approx 22\%$ strain without exhibiting any signs of shear localization (i.e. no plateau in the flow stress curve). Also superimposed on the graph is the flow stress curve of $\text{Ni}_3\text{Al}-0.095\%\text{B}$, a result taken from previous work by Sizek and Gray [25]. It should be noted that the Ni_3Al intermetallic utilized in our experiments contained 0.2at.%B instead of 0.095at.%B; although B content may exert some influence on the nature of the flow stress curve, the difference is probably less significant compared to the differences we anticipated from using an intermetallic (instead of Ni + Fe) as a binder

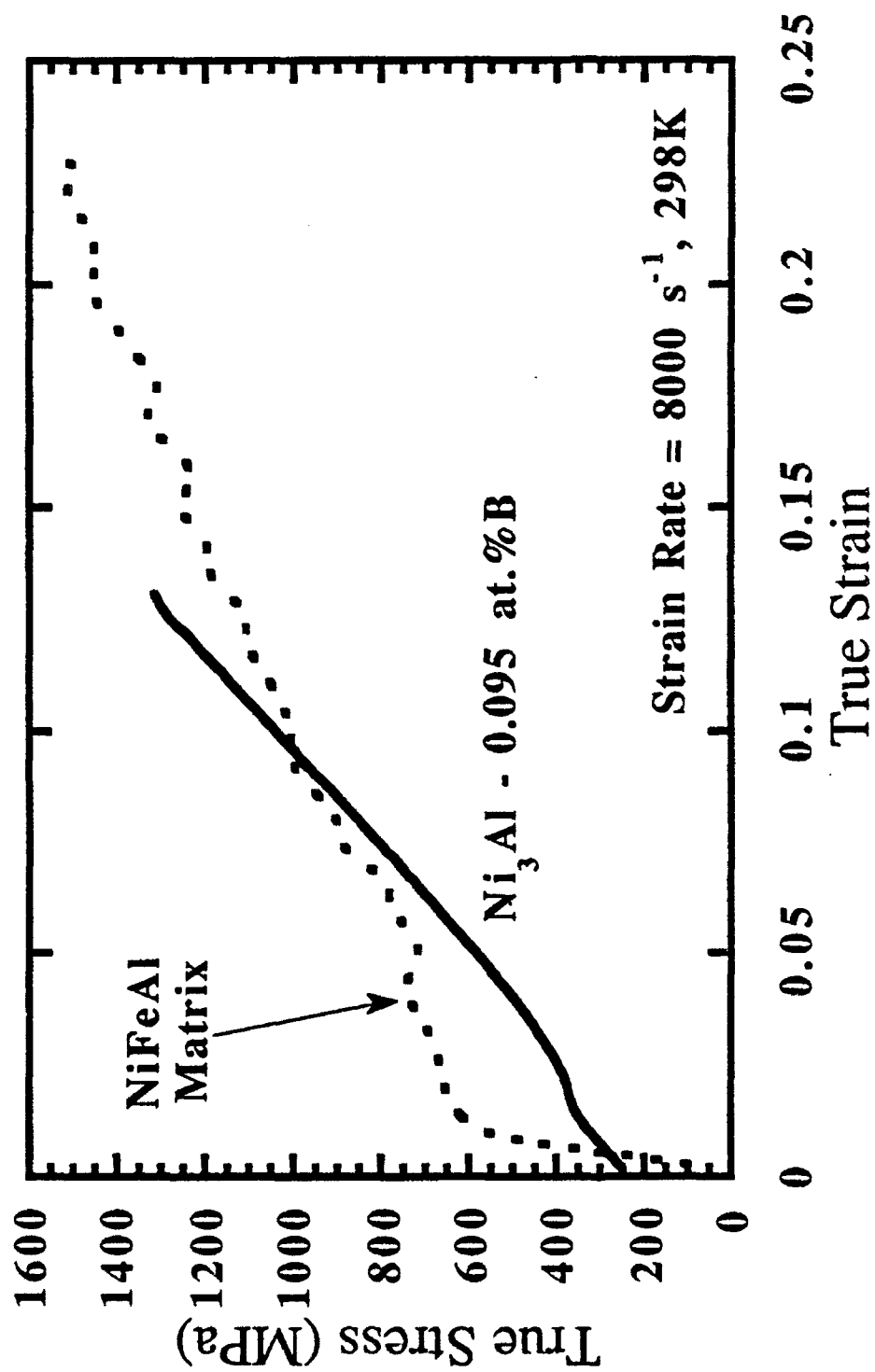


Figure 26. High strain rate ($5 \times 10^3/\text{sec}$) stress-strain relationships in intermetallic matrices utilized for WHA. Data for Ni_3Al from ref. 25.

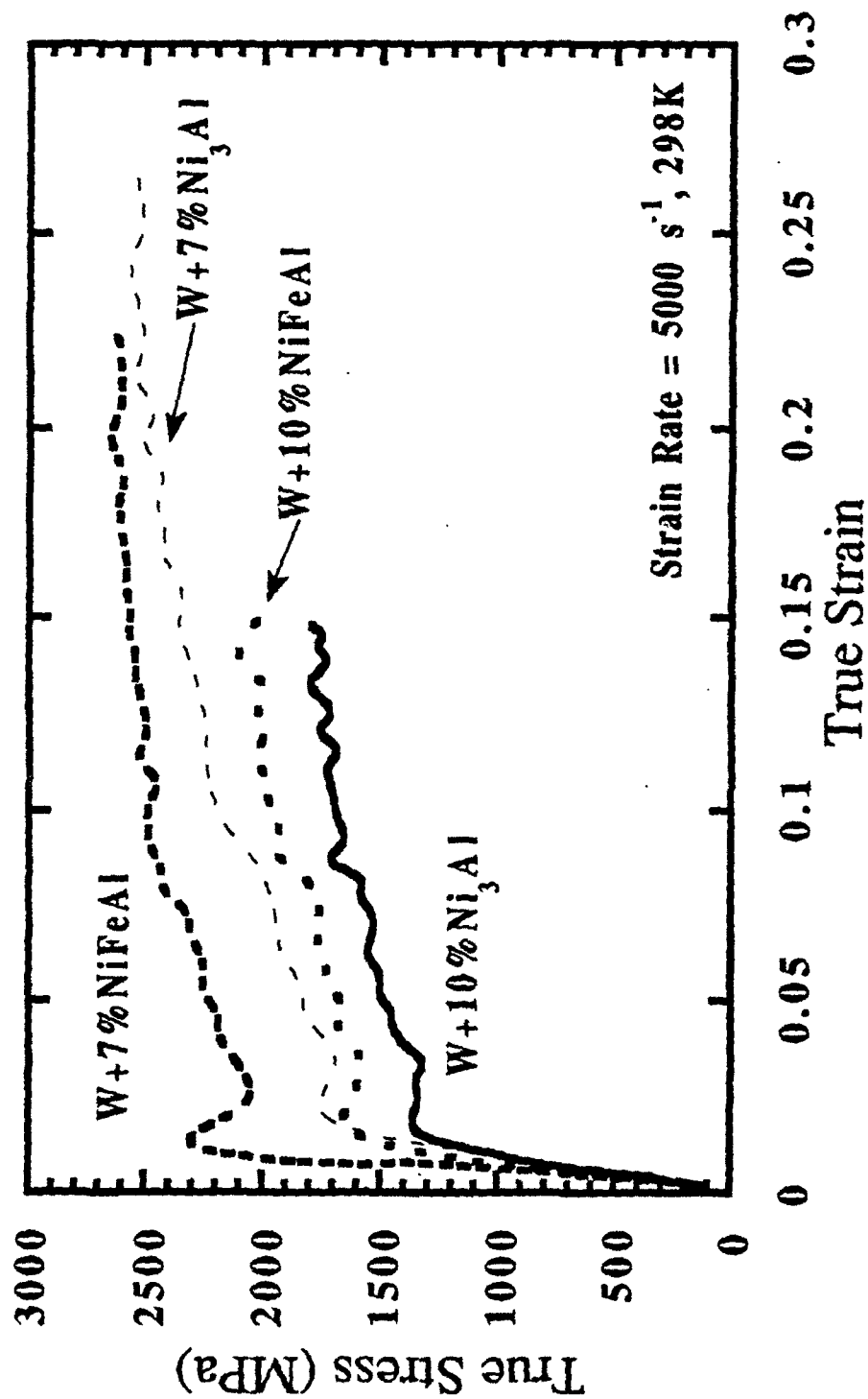


Figure 27. High strain rate ($5 \times 10^3/\text{sec}$) stress-strain relationships in intermetallic-based W heavy alloy composites with 7% and 10% Ni₃Al and NiFeAl matrices.

in WHA. Comparing the flow stress behavior for both these alloys indicates that, the dynamic 'yield strength' of the intermetallic Ni-12Al-40Fe is higher than that of Ni₃Al while the dynamic work-hardening rate of Ni₃Al is higher than that of Ni-12Al-40Fe. Thus, the flow stress for both these intermetallics is similar at $\approx 10\%$ strain despite their differences in initial flow stress levels.

Figure 27 shows four representative dynamic stress-strain curves (digitized from dispersion-corrected curves) for W-based composite with 7wt.% and 10wt.%, Ni₃Al and NiFeAl matrices. The results of high strain rate testing of WHA based on these intermetallic matrices indicates that:

1. increasing weight fractions of W lead to greatly increased strength
2. heavy alloys with NiFeAl matrix are stronger than those with Ni₃Al matrix indicating that the matrix contributes to the effective dynamic strength of the composite
3. the dynamic work-hardening rate of the WHA composite is higher for alloys based on Ni₃Al matrix compared to those based on NiFeAl matrix, indicating again that the dynamic properties of the composite are related to the dynamic properties of the matrix
4. the peak flow stress levels attained for hard hit (5" striker bar, 35psi gas pressure) W+7%Ni₃Al and W+7%NiFeAl specimens approach/exceed the strength of the pressure transmitting bars
5. For the 'hard hit' specimens, based on the plateau in flow stress curve, it would appear that shear localization should have been initiated in both the W+7%Ni₃Al and W+7%NiFeAl composites

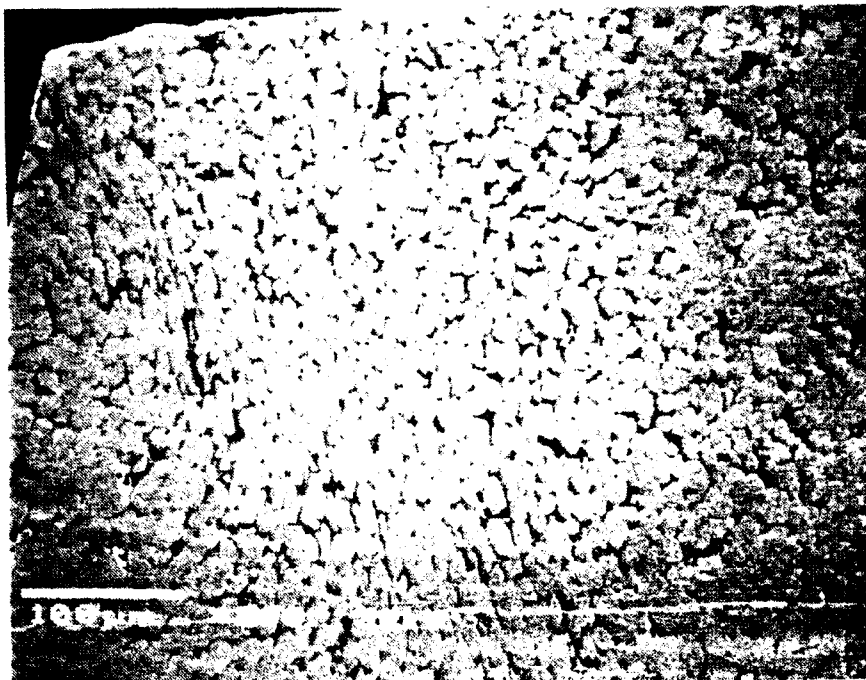
6. The 'hard-hit' WHA composite W + 7%NiFeAl failed into six pieces during the test

The 'hard-hit' Ni₃Al and NiFeAl-based WHA were examined in a SEM and the results are shown in Figure 28. From Figure 28a which is a longitudinal section of the deformed specimen, shear bands at $\approx 45^\circ$ to the stress axis can clearly be seen; the W grains have been deformed (elongated) along the shear bands while those away from the bands are relatively undistorted. Figure 28b is a SEM micrograph showing one (the largest) of the failed pieces of the W + 7%NiFeAl composite where the failure path is clearly at $\approx 45^\circ$ to the stress axis indicating failure by shear localization. Note that failure occurred in this specimen after $\approx 22\%$ strain while the W + 7%Ni₃Al composite endured $\approx 26\%$ strain without failure. Hence, it is clear that shear localization and failure along shear bands occurs more readily in WHA based on NiFeAl intermetallic matrix in comparison to those based on Ni₃Al matrix. These results demonstrate the validity of the proposed (Phase I) concept of developing alloys prone to a self-sharpening behavior by using intermetallic matrices that exhibit a trend of decreasing ductility with increasing temperature.

G. Electroless Coating of W powders by Ni

The processing techniques for tungsten heavy alloys can greatly affect the microstructure and the mechanical properties of these alloys. During preliminary experiments related to process development, it was observed that the starting intermetallic powder size in the mixture had a big impact on the final sample density. A finer matrix particle size resulted in significantly higher sintered densities. Besides the final sintered densities, the size of tungsten particles and contiguity can be varied by varying the particle

(a)



(b)

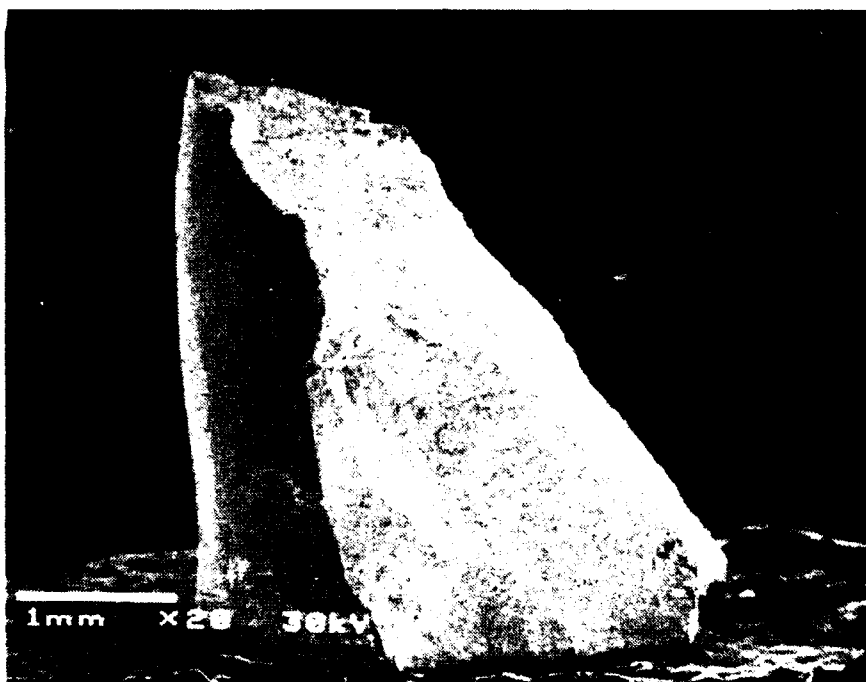


Figure 28. Shear localization in WHA with (a) Ni_3Al and (b) NiFeAl matrices.

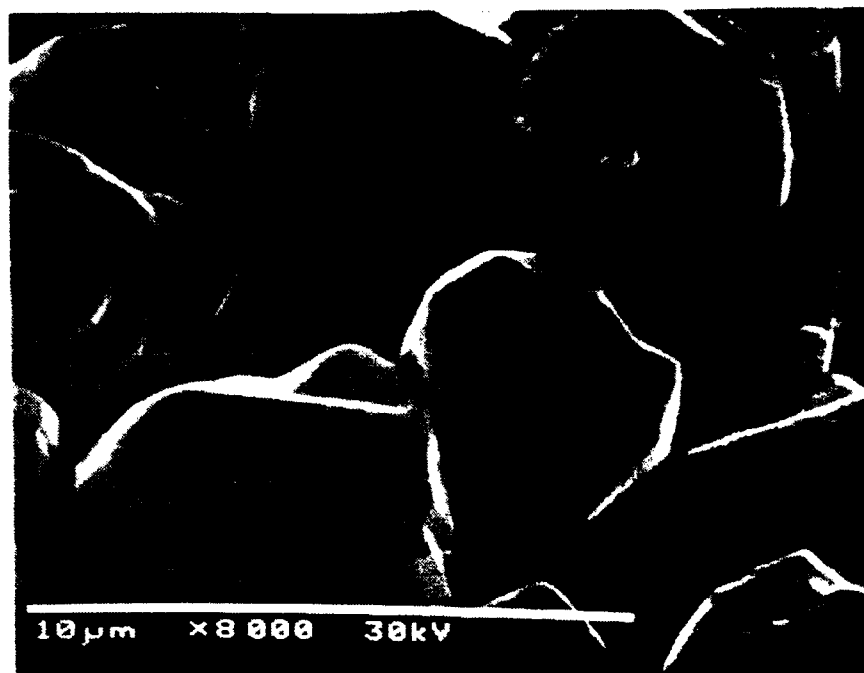
size of the starting powders. Electroless plating is one way of distributing the matrix phase in the form of uniform coating thickness over the individual tungsten particles. Electroless plating is the chemical deposition of a metal from an aqueous solution of a salt of the metal. Electroless nickel (EN) plating is the most important catalytic plating process and it has widespread commercial and industrial use. Electroless nickel deposits possess an unique combination of both corrosion and wear resistance. The ability to coat parts of any size and shape, with a uniform thickness coating makes electroless plating a powerful industrial technique.

There are two main groups of EN deposits. The first is the nickel-phosphorous group in which sodium hypophosphite is the reducing agent. The resulting coating have a typical phosphorous content of 7-11wt%. Nickel-boron constitute the second group and are obtained from solutions of an organic aminoborane which is used as the reducing agent. Typical boron contents are 0.2-4wt%. MER Corp. has selected to use the nickel-boron system because of the purity. Tungsten powders were coated using a commercial process, Niklad™ 752 with a boron content of 1% max. in the deposited coating. The components of the deposition solution are: (i) Niklad 752A 15vol% (nickel sulfamate), (ii) Niklad 752R, 5vol%, (dimethylamine borane), and (iii) distilled water, 80vol%. The deposition procedure consists of making a solution of the plating bath of the three components. The pH of the solution is adjusted to pH=5.5-6.8 using ammonium hydroxide (NH_4OH). The bath is heated and maintained to a temperature range of 60-77°C, and stirred using a magnetic stirrer. Tungsten powder is added for a bath loading of about 70in³/gallon. This primarily depends on the surface area of the powder. The expected deposition rate of the nickel onto

the tungsten is 0.2-0.3 mils/hr. The deposition conditions are maintained until the desired coating thickness have been reached. The powder is then filtered, rinsed with distilled water several times and then dried. Analysis and characterization of the powder is done by weight gain of the powder after deposition, SEM examination and chemical analysis of the Ni and B contents.

Figure 29a and 29b respectively are SEM micrographs of $12\mu\text{m}$ and $0.5\mu\text{m}$ size W powders coated with Ni. The Ni content was chemically analyzed to be $\approx 3\text{wt.}\%$ and $\approx 2\text{wt.}\%$ respectively in these powders. The boron content was also analyzed and found to be very small, well within the limits of expected boron contents. Note that for Ni_3Al type intermetallics, boron is actually considered a beneficial impurity. By a process of repeated plating, we have demonstrated that the Ni content can easily be raised to very high levels, $\approx 15\text{wt.}\%$ which would constitute a much higher matrix weight fraction than levels normally utilized in WHA. A small sample of this coated powder has been sent to the program technical monitor for independent evaluation. Such an easy technique for coating W powders irrespective of W particle size or shape (current chemical vapor deposition processes on W powders as practiced by Ultramet Corp. suffer from the limitation of fluidizing particles of spherical shape) can be easily utilized to reduce W-W contiguity. It remains to be seen (under a Phase II program) whether powder electroplating processes can be developed along similar lines to impart controlled coatings of any elements/compositions.

(a)



(b)

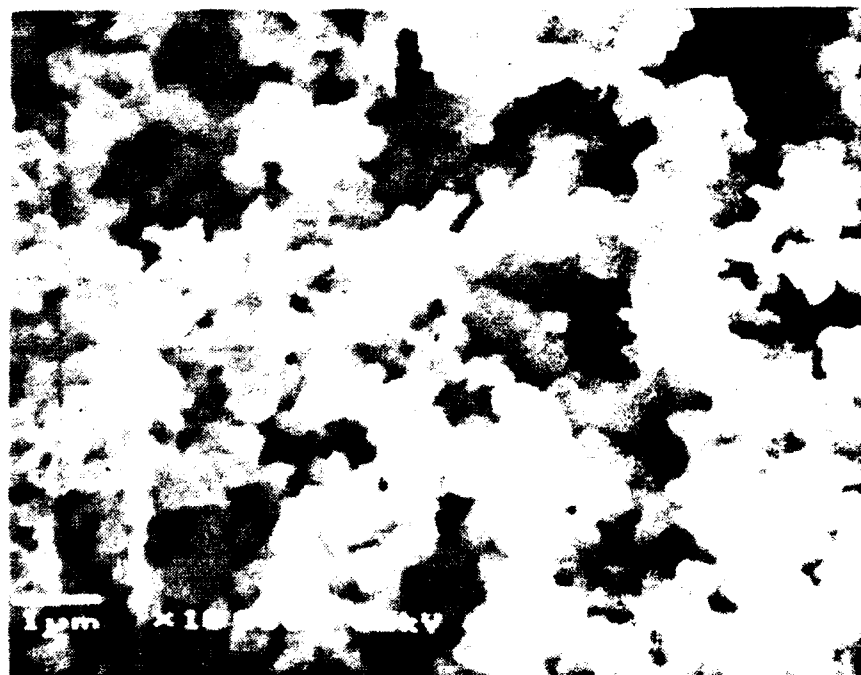


Figure 29. SEM micrographs of Ni-coated W powders coated by electroless deposition of Ni onto (a) 12 μ m size (b) 0.5 μ m size W particles.

H. Novel Processing Approaches For WHA

The liquid-phase sintering approach adopted for producing intermetallic-based WHA yielded W particle sizes in the range 20-30 μ m and the W particles were often in contact with other W particles. Since the improvements in mechanical properties of W alloys call for minimizing W-W particle contacts, and because coarse W particles can blunt cracks along adiabatic shear bands, some effort was directed towards producing high density microstructures with W particle sizes as small as possible and to minimize W-W particle contacts. Since the conventional WHA microstructures are produced by dissolution of W into the liquid Ni-Fe matrix and precipitation of W onto existing W particles (which leads to a few W particles growing at the expense of others), one approach to refining the W particle size is to minimize the sintering time and temperature while increasing the cooling rate. This can be achieved by sintering the W+intermetallic powder mixture pellets in an induction furnace where high cool-down rates from sintering temperatures are obtainable. Alternately, another approach would be to use W powder coated with Ni (or say Ni & Fe if NiFeAl is a desired intermetallic matrix), followed by in-situ generation of the intermetallic matrix amidst the W particles by a Self-Propagating High Temperature Synthesis (SHS) type reaction. The transient heating step (SHS reaction) when combined with some suitable consolidation step is capable of producing intermetallic matrix-based WHA with a refined scale of microstructure. The details relating to some preliminary attempts in this regard are discussed below.

For WHA composites based on Ni₃Al matrix, experiments were carried out with fine ($\approx 0.5\mu$ m av. size) and coarse ($\approx 12\mu$ m av. size) W powders electroless-coated with Ni as

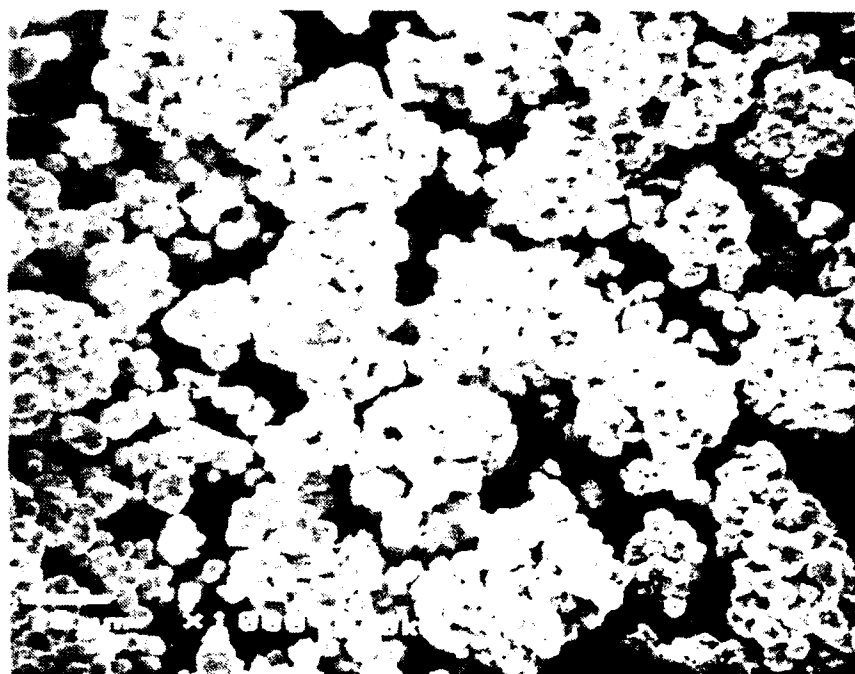
described in the previous section. By contrast, for WHA composites based on the NiFeAl matrix, it was desirable to generate W powders coated with both Ni and Fe; W powders of nominal $12\mu\text{m}$ size coated with both Ni and Fe (composition W-3wt.%Ni-0.5wt.%Fe) were procured from Ultramet Corp. (courtesy of Mr. Brian Williams) and utilized in our experiments to in-situ generate the intermetallic matrix in these WHA. However, since we received only a limited supply of such coated W powder (only 50 gms), some experiments had to be conducted using Ni-coated W powders with Fe and Al as added elemental powders. Figure 30a-b are SEM micrographs of the coated W powder as received from Ultramet Corp. Note that although the specified nominal W particle size is around $12\mu\text{m}$, the individual coated W powders appear to be $\approx 5\mu\text{m}$ in size rather than $12\mu\text{m}$.

Since the nominal Ni-to-Fe ratio on the as-received coated W powders (ratio = 6) was far removed from that required for the intermetallic Ni-12Al-40Fe (ratio ≈ 1.5), a different NiFeAl intermetallic composition was chosen to be processed through the SHS process. The new matrix composition was chosen to be Ni-10.65%Fe-10.4%Al-0.05%B (wt.%) which corresponds to Ni-20at.%Al-10at.%Fe (IC-46 according to Oak Ridge National Lab designation). This intermetallic is single phase $L1_2$ structured with the Fe replacing both the Ni and the Al equally on both lattice sites. Like other intermetallics discussed above, this intermetallic also exhibits a temperature-assisted embrittlement. The overall powder composition was adjusted to yield the composition 90%W-10% Ni-Fe-Al matrix. Following a variety of experimental attempts, only two approaches appeared to yield promising results and these techniques are discussed briefly below.

Approach #1: A 5gm W+Ni,Fe,Al pellet was ignited by a mixture of MoSi₂ and Ti₅Si₃ which generates a high transient temperature suitable for quick sintering of the WHA; since the adiabatic temperature of Ti₅Si₃ was higher than its melting point, MoSi₂ was added to lower the adiabatic temperature below its melting point. The silicide mixture itself was ignited by a Ni-31wt.%Al reactant pellet which has an adiabatic temperature of 1923K. The furnace temperature was ramped gradually up to 600°C where the high transient temperature generated is believed to have caused in-situ generation of the intermetallic matrix by a SHS reaction between the Ni, Fe and Al powders. Subsequently, the temperature was further ramped to 1100°C where it was held for 20 minutes before being cooled at 5°C/min. During the 20 minute soak at 1100°C, the pressure was ramped to a load of 2000lbs (2.5ksi) in 10 minutes and the load held steady for another 10 minutes before being released. The resulting microstructure is shown in Figure 31 where the average W particle size appears to be in the range 20-30μm and the W-W particle contacts appear to have been minimized. This processing technique will be investigated further under a Phase II program.

Approach #2: Despite minimizing the W-W contacts, the W particles themselves were significantly large compared to the starting W particle sizes. Experiments investigating the reduction of W particle sizes in the sintered microstructure were carried out in an induction furnace by placing the W+Ni+Fe+Al reactant pellet (0.25 dia. x 0.5" high) on a ceramic foam covered with a thin-walled graphite cup. The thin-walled graphite cup provides high heating and cooling rates. An example of a typical sintered microstructure (sintered for 5 minutes) generated through induction sintering is shown in Figure 32 where the average W

(a)



(b)

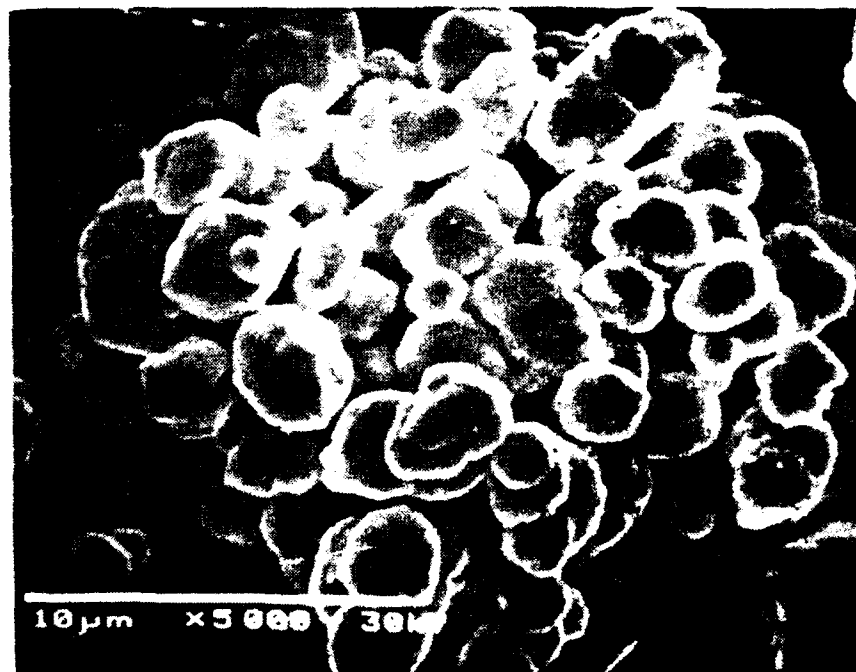


Figure 30. SEM micrographs of Ni-Fe coated W powders ($\approx 12\mu\text{m}$ nominal size) obtained from Ultramet Corp.



Figure 31. SEM micrograph illustrating the minimization of W-W particle contacts by a combination of applied pressure and transient heating (in-situ generation of the intermetallic matrix by a SHS reaction).



Figure 32. SEM micrograph illustrating the refinement of W particle size by induction sintering techniques.

particle size ranges between 5-10 μ m, almost similar to the starting W particle sizes. These preliminary experiments indicate significant promise in refining the scale of microstructure through rapid-sintering approaches. It is possible that by a suitable combination of electroless coating of ultrafine ($\approx 0.5\mu$ m size) W powders and rapid sintering approaches of the type described above, it may be possible to generate the intermetallic matrix in-situ in WHA while preventing significant growth of W particle sizes from the starting particle size of $\approx 0.5\mu$ m.

I. W-Mn ALLOYS

The effect of Mn as the matrix phase substituting the NiFe matrix for the WHA was examined for a 5wt.% matrix content. Preparation and processing of the samples followed standard procedures used for the other WHA. The Mn raw powder used was a 99.9% purity and a particle size of 1-5 μ m. Sintering temperature and time were 1550°C for 30 minutes. The samples reached a density of 17.987 g/cc (± 0.248) which corresponds to a density of 95% of theoretical. SEM analysis of the sample microstructure showed severe matrix phase segregation and large amounts of porosity. A micrograph of the sample is shown in Figure 33. Due to the inferior results obtained from the use of the Mn matrix and also the financial/time constraints of a Phase I program (especially since the primary objective was to investigate WHA based on L1₂ intermetallic matrices), this approach was not pursued further.

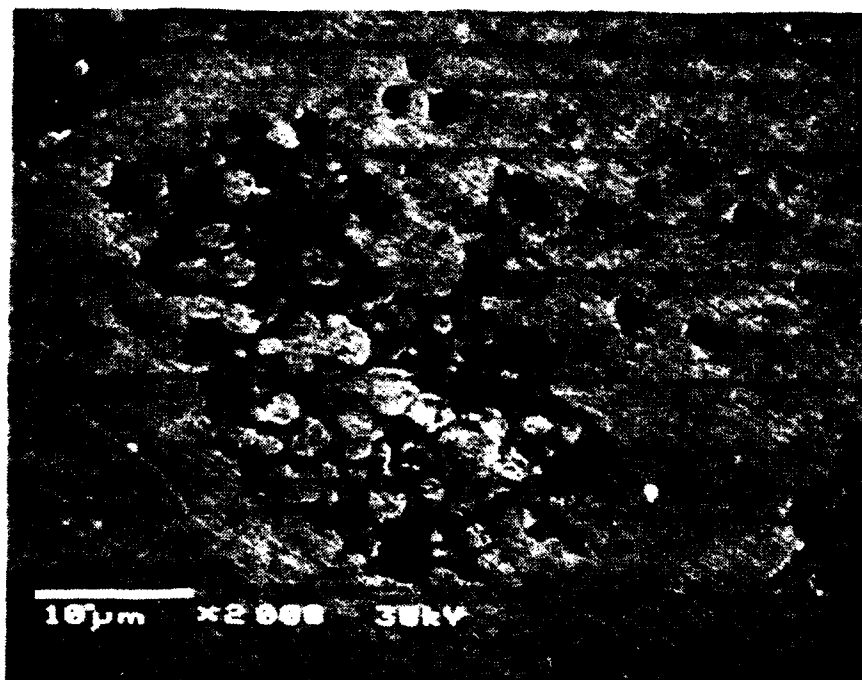
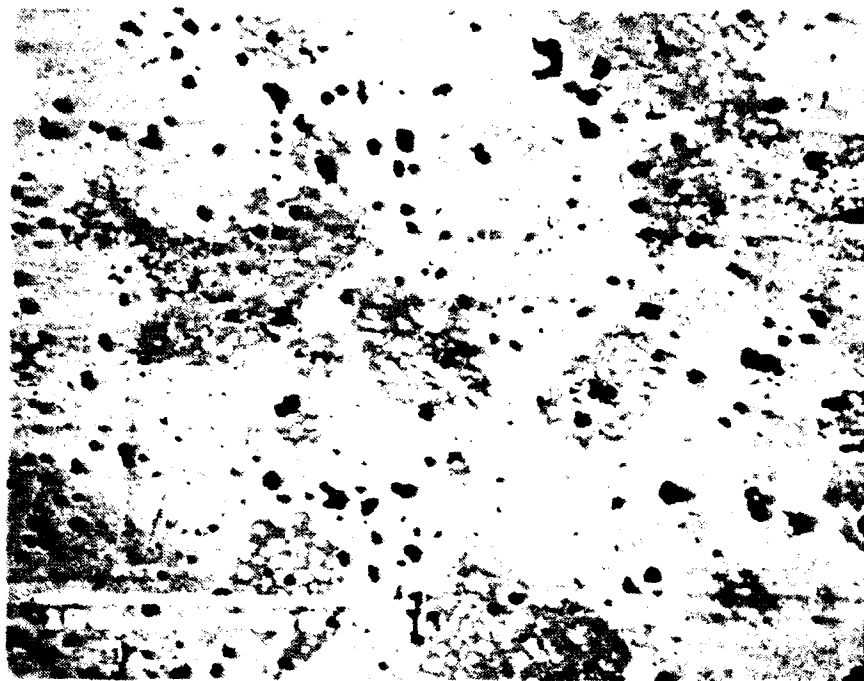


Figure 33. Liquid-phase sintered W+5wt.%Mn alloy showing extensive matrix segregation and porosity.

VI. DISCUSSION

Bose, Couque and Lankford [26] have recently reported the high strain rate flow behavior of as-sintered WHA based on Ni-Fe and Ni-Co matrices. The peak flow stresses for intermetallic-based WHA (≈ 2500 and 2600 MPa respectively for $W+7\%Ni_3Al$ and $W+7\%NiFeAl$) are ≈ 700 MPa higher than the peak flow stresses obtainable in as-sintered conventional WHA. Further, the flow stresses are either similar or ≈ 100 MPa higher than those reported for 25% swaged $W+9\%(Ni-Co)$ heavy alloy. Although the shear instability initiated in these heavy alloys at $\approx 15-20\%$ true strain, these conventional heavy alloys typically endured $> \approx 40\%$ strain prior to failure. By contrast, while shear instability initiated at similar strain levels ($\approx 15-20\%$ strain) in the $W+7\%NiFeAl$ composite, failure occurred at only $\approx 22\%$ strain. Since these $L1_2$ intermetallics are known to exhibit a high temperature embrittlement, the smaller failure strain is probably related to the ensuing high temperature embrittlement along adiabatic shear bands. It is interesting to note that the $W+7\%NiFeAl$ alloy also exhibits $\approx 5\%$ tensile elongation which may be adequate for thermo-mechanical processing and projectile launching considerations. The present investigation indicates that for WHA composites based on NiFeAl matrices, the unique combination of reasonable quasi-static and excellent dynamic properties for NiFeAl based WHA indicates that such alloys indeed should be investigated further as viable replacement candidates for DU as kinetic energy penetrators.

Clearly the quasi-static properties of WHA based on intermetallic matrices (especially NiFeAl matrix) can be improved considerably by optimization of the NiFeAl composition and processing conditions. For example, Andrade-Yanez et al.[27] have

recently examined the quasi-static properties of WHA with small additions of Al and Ti which result in the precipitation of $L1_2$ precipitates within the fcc matrix, similar to the microstructure of NiFeAl-based WHA. The quasi-static tensile ductility of those WHA composites [27] were $\approx 12\%$ indicating that by a suitable choice of NiFeAl composition, the quasi-static tensile properties can be improved significantly. It should be noted, however, that Andrade-Yanez et al.[27] did not examine the dynamic mechanical properties of their heavy alloys and it is possible that the choice of the NiFeAl matrix has to be optimized with respect to both quasi-static tensile ductility, dynamic strength and shear localization properties.

Bose et al.[26] have indicated the importance of matrix stoichiometry in promoting shear localization; a 7:3 rather than 8:2 ratio of Ni:Fe was found to be more susceptible to shear localization and cracking along shear bands despite their similar stress-strain behavior. Further, an inhomogeneous microstructure and swaging were shown to be favorable to shear localization. Swaging was shown recently [28] to exercise significant effect on shear localization properties with as-sintered heavy alloys exhibiting 'stable shear bands' (shear band where localization does not extend to the point that failure can be initiated in these bands) while 25% swaged alloys exhibit 'unstable shear bands' where localization occurs to the extent that cracking occurs along these bands. It was postulated that the residual dislocation density acts as a trigger to shear localization and cracking. However, it is also possible that a residual dislocation density can affect the other factors that affect critical strain for shear localization such as thermal conductivity, heat capacity and work-hardening; a reduced work-hardening rate and decreased thermal conductivity will produce conditions

conductive to shear localization. Thus, similar to the conventional WHA discussed above, for WHA based on $L1_2$ intermetallic matrices, thermomechanical processing may be utilized to increase the residual dislocation density (reduce the rate of work-hardening) further thereby leading to initiation of shear localization at lower strains.

For the intermetallic-based WHA examined here, the critical strain for shear localization is smaller for composites with lower work-hardening rates, consistent with the relationship of Staker [16]. From the flow stress behavior of matrices and W composites, it appears that the rate of work-hardening in the W composite is related to that for the matrix material itself; matrices with higher work-hardening rates (e.g. Ni_3Al compared to $NiFeAl$) impart higher work-hardening rate to the composite. The lower dynamic work-hardening rate of $Ni-12Al-40Fe$ compared to Ni_3Al (B doped) is similar to its quasi-static characteristic. This difference in work-hardening, in turn, may be related to the microstructure and operating deformation mechanisms. While the microstructure of Ni_3Al is single phase, the alloy $Ni-12Al-40Fe$ is two-phase, consisting of a dispersion of $L1_2$ -structured $(Ni,Fe)_3(Al,Fe)$ in a fcc (Ni,Fe,Al) matrix. It is possible that the higher resistance to flow offered by Ni_3Al may be related to the high APB energy on the primary deformation plane which would prevent these dislocations from operating individually or due to the splitting of superpartials into Shockley partials; cross-slip would then require re-combination of these Shockley partials and would lead to Kear-Wilsdorf locks thereby further increasing the flow stress required to carry on deformation. By contrast, deformation in the two-phase alloy may be concentrated in the fcc matrix and proceed either by shearing of the intermetallic precipitates or passage of APB-coupled dislocations within the weakly ordered

precipitates; the addition of Fe to Ni_3Al lowers the APB energy, hence the spacing between superpartials in Ni-12Al-40Fe is greater than in Ni_3Al , hence, deformation may proceed by cross-slip of single dislocations. Further, increasing deformation leading to shearing of intermetallic particles will reduce the area of ordered particles on the shear plane thereby leading to increased disorder with increasing deformation (experimentally, this was demonstrated [20] by the PI as increasing superpartial spacing with increasing distance from the head of the pile up); decreasing 'degree of order' will lead to progressively lower rates of work-hardening which would facilitate the localization of shear.

Interestingly, Magness [29] has demonstrated that despite the differences in quasi-static mechanical properties resulting from differences in swaging or matrix compositions, the dynamic penetration behavior of these composites based on conventional Ni-Fe type heavy alloy matrices are essentially identical. This indicates that novel approaches such as matrix substitution are necessary to improve the ballistic penetration behavior of WHA composites to levels comparable to those for DU penetrators. Baker and Dunn [30], for example, have examined DU as a matrix for WHA and demonstrated ballistic performance similar to those of U-0.75Ti penetrators. Since DU is environmentally unacceptable, alternate matrices such as Hf exhibit potential for performance enhancements of WHA. Unfortunately, although adiabatic shear may be initiated at lower strains in materials such as Hf, the general behavior of increasing ductility with increasing temperature implies that failure strains may still be significantly large enough to result in mushrooming (the imposed hydrostatic stresses at the head of the penetrator will further prevent early failure). By contrast, while thermo-mechanical processing of W+NiFeAl type WHA may lower the

critical strains to shear localization, the failure strains after shear localization will still be small, hence the material discard may be aided and the mushroom head minimized.

In summary, the present investigation suggests that ternary alloying elements such as Al (and possibly others such as Si and Ti) can affect the shear localization properties in WHA matrix either due to the general nature of plastic deformation by planar slip), a compositional effect (similar to that of Ni-Fe ratios discussed by Bose et al.[26]) or a microstructural effect (where an ultrafine dispersion of $L1_2$ phase in fcc matrix leads to shear localization). The negative dependence of matrix ductility on temperature holds significant promise to affect early failure in material soon after shear localization.

REFERENCES

1. P.N. Jones, Proc. of the Second International Tungsten Symp., SF, California, June (1982) 81.
2. L.S. Magness, "Deformation Behavior and Its Relationship to the Penetration Performance of High-Density KE Penetrator Materials", (Preprint).
3. B.H. Rabin and R.M. German, Met. Trans. 19A, (1988) 523.
4. A. Bose, D. Sims and R.M. German, Met. Trans. 19A, (1988) 487.
5. L.W. Meyer, H.D. Kunze and E. Staskewitsch, Proc. Seventh International Ballistic Symp., The Hague-Netherlands, (1983) 289.
6. J. Lankford, C.E. Anderson Jr., S.R. Bodner, J. mat. Sci. Lett., (1988) 1355.
7. K. Frank and J. Zook, Int. J. of Impact Engg., 5, (1986) 277.
8. E. Bloore and L. Herr, "Penetrator Materials Development", published in Agenda of Presentations given at the 1978 US-FRG Meeting Asso. with DEA-G-1060 Ballistic Research and Development, v 2, log no. RJE (SP)-5-S-78.
9. L. Magness, Proc. 28th NATO DRG Seminar on Novel Materials for Impact Loading, Bremen, FRG.
10. L.W. Hantel and J.W. Taylor, PHERMEX Evaluation of Air Force Tungsten and U-0.75Ti Penetrators, Los Alamos National Lab. Rep. LA-5658.
11. T. Nicholas, "Dynamic Testing of Structural Materials Using a Split Hopkinson Bar Apparatus", Tech. Rep. AFWAL-TR-80-4053, (1980).

12. D. Sandstrom, P. Dunn and W. Hogan, "Comparison of Tungsten and Uranium Kinetic Energy Penetrators Fired Into Semi-infinite Steel Targets", Proc. Tungsten Ordnance Tech. Seminar, Washington DC, (1986).
13. E. Foster et al., "Penetration of Ballistic Test Specimens From Ta-coated W Powders", Batelle, Columbus, Contract Rep. to BRL.
14. F.J. Fulton, C.F. Cline and E.O. Snell, "Penetration of Mild Steel Targets by High Density Long-Rod Penetrators, Lawrence Livermore Lab. Rep., UCRL-52991.
15. D.A. Shockey, L. Seaman and D.R. Curran, "Metallurgical Effects at High Strain rates", eds. R.W. Rhode et al., Plenum Press, New York, (1973) 473.
16. M.R. Staker, Acta Met., 29, (1981) 683.
17. J.A. Horton, C.T. Liu and M.L. Santella, Met. Trans. 18A, (1987) 1265.
18. N.S. Stoloff, Int. Met. Rev., 34, (1989).
19. K. Aoki and O. Izumi, J. Japan Inst. Met., 43, (1979) 1190.
20. S. Guha, Doctoral Dissertation, Dartmouth College.
21. W. Hogan, personal communication.
22. W.J. Bruchey, E.J. Howarth and P.W. Kingman, BRL Interim Memo. Rep. no. 941, (1990).
23. C.M. Kippbut, A. Bose, S. Farooq and R.M. German, Met. Trans, 19A, (1988) 1905.
24. G.E. Dieter, "Mechanical Metallurgy", McGraw Hill Publishers, 237.
25. H.W. Sizek and G.T. Gray III, Acta Metall., (1992) in press.
26. A. Bose, H. Couque and J. Lankford Jr., Paper Presented at 1992 World Congress MPIF, San Fransisco.

27. V. Andrade-Yanez, J.J. Urcola Galarza, K. Ostolaza Zamora and J. Gil Sevillano, Paper presented at the International Conf. on Tungsten and Tungsten Heavy Alloys, Nov 15-18, 1992, Washington DC.
28. H.R. Couque, A. Bose and J. Lankford Jr., Paper presented at the International Conf. on Tungsten and Tungsten Heavy Alloys, Nov 15-18, 1992, Washington DC.
29. L.S. Magness, Paper presented at the International Conf. on Tungsten and Tungsten Heavy Alloys, Nov 15-18, 1992, Washington DC.
30. B.D. Baker and P.S. Dunn, Paper presented at the International Conf. on Tungsten and Tungsten Heavy Alloys, Nov 15-18, 1992, Washington DC.

Distribution List

1 Office of the Secretary of Defense for Research and Engineering, The Pentagon, Washington, D.C. 20301

Director, U.S. Army Research Laboratory, 2800 Powder Mill Road, Adelphi, MD 20783-1197

1 ATTN: AMSRL-OP-CI-AD, Technical Publishing Branch

1 Dr. Alan Goldman

1 AMSRL-OP-CI-AD, Records Management Administrator

Commander, Defense Technical Information Center, Cameron Station, Building 5, 5010 Duke Street, Alexandria, VA 22304-6145

2 DTIC-FDAC

1 MIAC/CINDAS, Purdue University, 2595 Yeager Road, West Lafayette, IN 47905

Commander, Army Research Office, P.O. Box 12211, Research Triangle Park, NC

27709-2211

1 ATTN: Information Processing Office

1 Dr. Andrew Crowson

Dr. Edward Chen

Commander U.S. Army Materiel Command (AMC), 5001 Eisenhower Avenue, Alexandria, VA 22333

1 ATTN: AMCSCI

Commander, U.S. Army Materiel Systems Analysis Activity, Aberdeen Proving Ground, MD 21005

1 ATTN: AMXSY-MP, Director

Commander, U.S. Army Missile Command, Redstone Arsenal, AL 35809

1 ATTN: AMSMI-RD-CS-R/Doc

Commander, U.S. Army Armament Research Development and Engineering Center, Dover, NJ 07801

1 ATTN: Technical Library

1 Mr. D. Kapoor

1 Dr. S. Cytron

Commander, U.S. Army Tank-Automotive Command, Warren, MI 48397-5000

2 ATTN: AMSTA-TSL Technical Library

Commander, U.S. Army Foreign Science and Technology Center, 220 7th Street, N.E., Charlottesville, VA 22901

3 ATTN: AIFRTC, Applied Technologies Branch, Gerald Schlesinger

Naval Research Laboratory, Washington, D.C. 20375

1 ATTN: Code 2627

1 Dr. Virgil Provenzano

Chief of Naval Research, Arlington, VA 22217

1 ATTN: Code 471

Naval Surface Weapons Center, Dahlgren Laboratory, Dahlgren, VA 22448

1 ATTN: Code G-32, Ammunition Branch, Mr. Brian Sabourin

Commander, Rock Island Arsenal, Rock Island, IL 61299-6000

1 ATTN: SMCRI-SEM-T

Battelle Columbus Laboratories, Battelle Memorial Institute, 505 King Avenue, Columbus, OH 43201

1 ATTN: Mr. Henry Cialone

1 Dr. Alan Clauer

Battelle Pacific Northwest Laboratories, P.O. Box 999, Richland, WA 99352

1 ATTN: Mr. William Gurwell

1 Dr. Gordon Dudder

1 Mr. Curt Lavender

GTE Sylvania, Inc. Chemical and Metallurgical Division, Hawes Street, Towanda, PA 18848

1 ATTN: Dr. James Mullendore

1 Mr. James Spencer

1 Ms. Susan Doepker

Director, U.S. Army Research Laboratory, Aberdeen Proving Ground, MD 21005

1 ATTN: AMSRL-WT

1 AMSRL-WT-T, Dr. Lee Magness

1 Ms. W.A. Leonard

Teledyne Firth Sterling, 1 Teledyne Place, LaVergne, TN 37086

1 ATTN: Dr. Steven Caldwell

Los Alamos National Laboratory, ATAC, MS F681, P.O. Box 1663, Los Alamos, NM 87545

1 ATTN: Mr. Bill Hogan

1 Mr. Paul Dunn

1 Mr. Bill Baker

Philips Elmet, 1560 Lisbon Road, Lewiston, ME 04240

1 ATTN: Mr. James Anderson

Ultramet, Inc., 12173 Montague Street, Pacoima, CA 91331

1 ATTN: Mr. Brian Williams

1 Dr. Robert Tuffias

Ceracon, Inc., 1101 N. Market Boulevard, Suite 9, Sacramento, CA 95834

1 ATTN: Dr. Ramas Raman

1 Mr. Sundeep Rele

Southwest Research Institute, 6220 Culebra Road, P.O. Drawer 28510, San Antonio, TX 78228-0510

1 ATTN: Dr. James Lankford

Metalworking Technology, Inc., 1450 Scalp Avenue, Johnstown, PA 15904

1 ATTN: Mr. C. Buck Skena

1 Mr. Timothy McCabe

Research Triangle Institute, P.O. Box 12194, Research Triangle Park, NC 27709-2154

1 ATTN: Dr. John B. Posthill

3C Systems, 620 Arglye Road, Wynnewood, PA 19096

1 ATTN: Mr. Murray Kornhauser

Advance Technology Coatings, 300 Blue Smoke Ct. West, Fort Worth, TX 76105

Alliant Techsystems, 7225 Northland Drive, Brooklyn Park, MN 55428

1 ATTN: Dr. Stan Nelson

1 Mr. Mark Jones

1 Mr. Thomas Steigauf

CAMDEC, 3002 Dow Avenue, Suite 110, Tustin, CA 92680

Chamberlain Manufacturing Co., 550 Esther St., P.O. Box 2545, Waterloo, IA 50704

1 ATTN: Mr. Tom Lynch

Defense Technology International, Inc., The Stark House, 22 Concord Street,

Nashua, NH

1 ATTN: Mr. Douglas Ayer

Materials and Electrochemical Research Corporation, 7960 S. Kolb Road, Tucson, AZ 85706

1 ATTN: Dr. James Withers

1 Dr. Sumit Guha

Materials Modification, Inc., 2929-P1 Eskridge Center, Fairfax,
VA 22031
1 ATTN: Dr. T.S. Sudarshan

Micro Materials Technology, 120-D Research Drive, Milford, CT
06460
1 ATTN: Dr. Richard Cheney

Nuclear Metals, 2229 Main Street, Concord, MA 01742
1 ATTN: Dr. Willian Nachtrab

Olin Ordnance, 10101 9th Street N., St. Petersburg, FL
1 ATTN: Hugh McElroy

The Pennsylvania State University, Department of Engineering
Science and Mechanics, 227 Hammond Building, University Park, PA
16802-1401
1 ATTN: Dr. Randall M. German, Professor, Brush Chair in
Materials

Worcester Polytechnic Institute, 100 Institute Road, Worcester,
MA, 01609
1 ATTN: Dr. Ronald Biederman
1 Dr. Richard Sisson

Failure Analysis Associates, Inc., 149 Commonwealth Drive, PO Box
3015, Menlo Park, CA 94025
1 ATTN: S.P. Andrew
1 R.D. Caliguri
1 T.K. Parnell
1 L.E. Eiselstein

Amorphous Technologies International, Laguna Hills, CA
1 ATTN: Mr. Dick Harlow

Parmatech Corporation, 2221 Pine View Way, Petaluma, CA 94952
1 ATTN: Dr. Animesh Bose

Stiglich Associates, PO Box 206, Sierra Madre, CA 91025
1 ATTN: Dr. Jack Stiglich

Director, U.S. Army Research Laboratory, Watertown, MA 02172-0001
2 ATTN: AMSRL-OP-CI-D, Technical Library
1 AMSRL-OP-CI-D, Visual Information Unit
1 AMSRL-OP-PR-WT
20 AMSRL-MA-MB, Mr. Robert Dowding, COR